Non-Destructive Testing of Capless Porcelain Line Post Insulators to Detect Internal Defects

Leslie Borrill

Thesis submitted for the Masters Degree in Engineering Sciences at the University of Stellenbosch

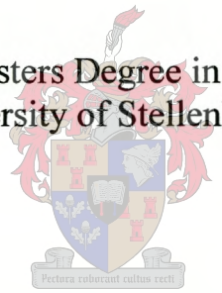

Supervisors:

Dr. J.P. Holtzhausen, University of Stellenbosch (Supervisor)
Dr. W.L. Vosloo, ESKOM Enterprises, TSI (Co-supervisor)

December 2003

Declaration

I, the undersigned, hereby declare that the work contained in this thesis is my own original work and has not previously, in its entirety, been submitted at any university for a degree.

Synopsis

This project relates to the unexplained failure of 33kV porcelain line post insulators in ESKOM's Southern Region. An initial investigation suggested that the failures could probably be due to a combination of internal manufacturing flaws and the effects of lightning. The failures all occurred in insulators based on a new design that uses a metal spindle for mechanical attachment to a power line structure embedded in the insulator base.

This thesis investigates the non-destructive detection of internal flaws in porcelain line post insulators. The research was structured as follows:

- The examination of the manufacturing process and materials used to determine the cause, location and nature of internal flaws.
- An electrical field simulation study to verify whether a void in the sulphur cement will experience discharge activity when exposed to system nominal voltage or lightning potential.
- The identification of non-destructive techniques (NDT) that are potentially viable for determining the presence of insulator internal flaws.
- The design of NDT experiments for X-ray, partial discharge (PD) detection and ultrasonic testing. These experiments were evaluated for their effectiveness in determining the presence of internal flaws and their usefulness as a quality control measure in the insulator manufacturing process.

The main findings are:

- The major cause of insulator internal flaws is the fast setting sulphur cement used for cementing the metal spindle (mechanical attachment) to the porcelain body of the insulator.
- The field simulation study shows that a discharge in a 3mm diameter spherical void on the insulator's axis of symmetry will occur if the insulator is exposed to lightning potential.
- High energy X-raying is an effective technique for exposing the location, nature, size and number of flaws in the insulator, but is impractical due to the high X-raying cost and over-utilisation of the only high energy X-ray facility in the RSA.

- The PD experiment was effective in revealing the presence of internal flaws, but the location, nature, size and number of flaws cannot be determined. The experiment is time consuming and is therefore not suitable for quality control in the insulator manufacturing process.
- A preliminary investigation into the suitability of ultrasonic testing techniques encountered major technical difficulties. Further investigation into the use of ultrasonic 3D imaging techniques is recommended.

Samevatting

Hierdie projek hou verband met die onverklaarbare faling van 33kV porselein staaf-tipe isolators in ESKOM se Suidelike Streek. 'n Aanvanklike ondersoek het daarop gedui dat die falings veroorsaak is deur 'n kombinasie van interne vervaardigings-foute en die effek van weerlig. Die falings het almal plaasgeving op isolators waarvan die vashegtingsbout direk in die porselein versink is.

Die doel van hierdie navorsingsprojek is om nie-vernietigende toetsmetodes (NVT) te ondersoek, teneinde interne foute in die tipe isolators op te spoor. Die tesis is soos volg gestruktureer:

- Die ondersoek van die vervaardigingsproses en die materiale wat gebruik word, ten einde die oorsaak, posisie en aard van hierdie foute vas te stel.
- 'n Simulasie van die elektriese veld om vas te stel of 'n holte in die swael-sement ontladings sal ondervind onder die invloed van nominale spanning en weerlig.
- Die indentifisering van nie-vernietignde toetsmetodes wat gebruik kan word om die teenwoordigheid van interne foute te bepaal.
- Die ontwerp van NVT eksperimente vir X-straal, gedeeltelike ontlading ("PD") deteksie en ultrasoniese toetsing. Hierdie eksperimente is geëvalueer om hul effektiwiteit om die teenwoordigheid van interne foute vas te stel, asook hul nuttigheid as 'n kwaliteitsbeheermaatreël in die isolatorvervaardigingsproses.

Die hoofbevindinge is:

- Die hoofoorsaak van die interne foute is die vinnig-stollende swael-sement wat gebruik word om die metaalinsetsel aan die porselein te heg.
- Die veldsimulasies het getoon dat 'n ontlading in 'n 3mm sferiese holte op die isolator se simmetrie-as sal plaasvind as die isolator aan weerligpotensiaal onderwerp word.
- Hoë-energie-X-strale is 'n effektiewe tegniek om die posisie, aard, grootte en aantal foute in die isolator vas te stel. Dit is egter onprakties as gevolg van die

hoë koste en oorbenutting van die enigste hoë-energie-X-straal-fasiliteit in die RSA.

- Die ontladingsdeteksie eksperiment was effektief om die teenwoordigheid van interne foute aan te dui, maar die posisie, aard, grootte en getal foute kan nie bepaal word nie. Die eksperiment is tydrowend en is daarom nie geskik vir kwaliteitsbeheer van die isolatorvervaardigingsproses nie.
- 'n Voorlopige ondersoek na die geskiktheid van ultrasoniese toetsmetodes het groot tegniese stuikelblokke opgelewer. Verdere ondersoek van die gebruik van ultrasoniese 3D-beeldtegnieke word aanbeveel.

Acknowledgements

I record my appreciation, in no specific order, to:

- My supervisor, Dr. Koos Holtzhausen, for his guidance.
- ESKOM for sponsoring the project.
- Mr Leon Kranhold of Somchem-Denel, for his assistance and guidance beyond contractual obligations.
- Dr Wallace Vosloo, for his guidance.
- Prof. B. Mortimer and the staff of the CIR at the Cape Technikon for their help and assistance with ultrasonic testing.
- Mr Jan Venter for providing me with technical information and insulator samples.
- Mr Petrus Pieterse for his assistance in the high voltage laboratory.
- My family.
- My Lord and saviour Jesus Christ for keeping his helping hand on me.

Table of Contents

Declaration		ii
Synopsis		iii
Samevatting		v
Acknowledgements		vii
Table of Contents		viii
List of Figures		xii
List of Tables		xvii
Glossary of Terms		xviii
1	INTRODUCTION	1
1.1	A Brief History of Porcelain as a High Voltage Insulator	1
1.2	General Background to this Investigation	2
1.3	Aims of the Thesis	4
1.4	Structure of this Thesis	5
References		7
2	THE MATERIALS AND PROCESS OF MANUFACTURE OF PORCELAIN POST INSULATORS	8
2.1	The Constituents of Ceramic Materials	8
2.2	The Manufacturing Process of Porcelain Insulators	9
2.3	Inspection and Screening Tests on Completed Components	12
2.4	Assembly of the Insulator	12
2.5	Routine Tests on the Completed Insulator	13
2.6	Discussion of the Manufacturing Process	15
2.6.1	Location and Types of Internal Flaws	15
2.6.2	The Causes of Internal Flaws	17
2.6.3	Dielectric Materials Used	17
Conclusion		18
References		20
3	ELECTRIC FIELD SIMULATION STUDY	21
3.1	Software package	22
3.2	Preliminary Study	23
3.3	Flow diagram	23
3.4	Insulator Electric Field Simulation	24
3.4.1	Insulator profile	24
3.4.2	Software Simulation	24
3.5	Simulation Results	26
3.6	Analysis of Results	28
Conclusions		28
References		29

4 NON-DESTRUCTIVE TESTING TECHNIQUES 30

4.1 Industrial Radiography 30
4.1.1 Units of measurement 31
4.1.2 Quality of Radiation and Contrast of the Radiation Image 31
4.1.3 Choice of X-ray source 32
4.1.4 Intensifying Screens 33
4.1.5 Choice of X-ray film and Processing 34
4.1.6 Radiograph Viewing 34
4.1.7 Defect Discernibility 34
4.1.7.1 Geometric Unsharpness, U_g 35
4.1.7.2 Inherent (Film) Unsharpness, U_f 35
4.1.7.3 Total Unsharpness, U_T 36
4.1.7.4 Choice of Source-to-film Distance (s.f.d.) 36
4.1.7.5 The Inverse Square Law 37
4.1.7.6 Prevention of Image Distortion 37
4.2 Partial Discharge Detection 38
4.2.1 Choice of PD Measurement Parameter 38
4.2.2 Discharge Inception and Extinction in Dielectric Voids. 40
4.2.3 Discharge Magnitude 41
4.2.4 Selection of Test Circuit Configuration 41
4.2.5 Recognition of Discharges 42
4.2.5.1 Determination of discharge magnitudes 43
4.2.5.2 Discharge Patterns 43
4.2.5.3 X-Y Diagram 44
4.3 Ultrasonic Testing 45
4.3.1 Reflection and Transmission 46
4.3.2 Refraction (Snell's Law) 47
4.3.3 Boundaries 48
4.3.4 Pulse-Echo Method of Flaw Detection 48
Conclusion 50
Industrial Radiography 50
Partial Discharge Detection 50
Ultrasonic Testing 51
References 51

5 DESIGN AND SET-UP OF NDT EXPERIMENTS 53

5.1 X-ray Detection 54
5.1.1 Experimental Set-up 54
5.2 Partial Discharge Detection 56
5.2.1 Test Specimen Preparation 57
5.2.2 Components of Detection Circuit 58
5.2.3 Test Procedure 60
5.3 Ultrasonic Testing 63
5.3.1 Pulse-Echo Method 63
5.3.2 Change of Flight Method 66

Conclusion 67
X-ray Detection 67
Partial Discharge Detection 67
Ultrasonic Testing 68
References 68

6 ANALYSIS OF EXPERIMENTAL RESULTS 69

6.1 X-ray Results 69
6.1.1 Presentation of X-ray Images 69
6.1.2 X-ray Image Analysis 70
6.1.3 Validity of X-ray as a NDT Technique 72
6.2 Partial discharge results 77
6.2.1 Medium Wave Radio Receiver 87
6.3 Ultrasonic experimental results 88
6.3.1 Pulse-Echo Method 88
6.3.2 Change of Flight Method 89
Conclusions 89
X-ray Detection 90
PD Detection 90
Ultrasonic Testing 91
References 91

7 CONCLUSIONS AND RECOMMENDATIONS 92

7.1 Conclusions 92
7.1.1 Manufacture 92
7.1.2 Electric Field Simulation 93
7.1.3 Non-Destructive Testing 94
7.1.3.1 X-ray 94
7.1.3.2 Partial Discharge Detection 95
7.1.3.3 Ultrasonic Testing 97
7.1.3.4 Impulse Testing 98
7.2 Recommendations 98
7.2.1 Manufacture 98
7.2.2 Electric Field Simulation 99
7.2.3 X-ray 99
7.2.4 Partial Discharge Detection 99
7.2.5 Ultrasonic Testing 100
7.2.6 The Effect of PD on the Insulator Materials 100
7.2.7 Impulse Test 100
References 100

APPENDIX A.1: STEP-WAVE OUTPUT VOLTAGE FOR EACH ATTENUATOR SETTING 102

APPENDIX A.2: E.R.A. DISCHARGE DETECTOR MODEL 3 INPUT 103

UNIT SELECTION TABLE

APPENDIX A.3: OPERATING INSTRUCTIONS FOR THE E.R.A. DISCHARGE DETECTOR MODEL 3 104

APPENDIX B.1: ACOUSTIC CHARACTERISTICS OF SOME NON-PIEZOELECTRIC MATERIALS 105

APPENDIX C.1: EXPERIMENTAL RESULTS FROM PD DETECTION MONITORING OF INSULATOR SAMPLE 2. 106

APPENDIX C.2: EXPERIMENTAL RESULTS FROM PD DETECTION MONITORING OF INSULATOR SAMPLE 3. 107

APPENDIX C.3: EXPERIMENTAL RESULTS FROM PD DETECTION MONITORING OF INSULATOR SAMPLE 4. 108

APPENDIX C.4: EXPERIMENTAL RESULTS FROM PD DETECTION MONITORING OF INSULATOR SAMPLE CX2. 109

APPENDIX C.5: EXPERIMENTAL RESULTS FROM PD DETECTION MONITORING OF INSULATOR SAMPLE CX1. 110

APPENDIX C.6: EXPERIMENTAL RESULTS FROM PD DETECTION MONITORING OF INSULATOR SAMPLE A. 111

APPENDIX C.7: EXPERIMENTAL RESULTS FROM PD DETECTION MONITORING OF INSULATOR SAMPLE B. 112

APPENDIX C.8: EXPERIMENTAL RESULTS FROM PD DETECTION MONITORING OF INSULATOR SAMPLE C. 113

APPENDIX C.9: EXPERIMENTAL RESULTS FROM PD DETECTION MONITORING OF INSULATOR SAMPLE CX. 114

List of Figures

Figure 1.1: Porcelain line post insulators, (a) a 33kV capless 4kN (900mm creepage) insulator and (b) a 33kV capped 4kN (786mm creepage) insulator. 2

Figure 1.2: A fragment of a porcelain post insulator with embedded electrode (metal insert), which failed under windloading. The photograph shows PD activity at the sulphur cement to porcelain interface and sulphur cement that has filled an extensive stress fracture. Also visible is the fault plane of the failed insulator. 4

Figure 2.1: (a) Extruded Tube ready for turning, and (b) turning in progress. 10

Figure 2.2: (a) Insulator rejected due to crack prior to glaze application, and (b) insert hole at insulator base coated with unfired porcelain chips with stress fractures visible at the top of the hole. 11

Figure 2.3: (a) Insulators stacked ready for glazing, (b) glazed insulators stacked and ready for firing, and (c) kiln lowered over stacked insulators. 11

Figure 2.4: Insulator shrinkage due to the drying out. 12

Figure 2.5: Heated sulphur cement mixture. 13

Figure 2.6: (a) Glazed insulator revealing hole for metal insert, (b) insertion of metal insert, (c) jig is positioned over insulator base, and (d) sulphur cement is poured into the cavity. 14

Figure 2.7: (a) Insulator is bolted to test table and the test arm is positioned against the free end of the insulator body, and (b) insulator deflecting under cantilever loading. 15

Figure 2.8: (a), (b) and (c) are failed insulators showing clear evidence of internal flaws. 16

Figure 3.1: 33kV 4kN (900mm creepage) capless porcelain line post insulator. 21

Figure 3.2: Flow diagram of simulation method followed [1]. 23

Figure 3.3: Insulator profiles, (a) manufacturer and (b) edited for importing into SLIM [1]. 24

Figure 3.4: Blown up section of base of insulator with void visible in the sulphur cement [1]. 25

Figure 3.5: Data paths for base of the insulator without void [1]. 26

Figure 3.6: Electric field vectors (a) at conductor surface and (b) inside sulphur cement [1]. 26

Figure 3.7 Electric field strength for path A to B at 19kv without a void [1]. 26

Figure 3.8 Electric field strength for path C to D at 19kV without a void [1]. 27

Figure 4.1: A schematic diagram of an image of an object of widely varying thickness [2]. 32

Figure 4.2: X-ray paths 'a' along diameter and 'b' at edge of solid cylinder. 32

Figure 4.3: Geometric unsharpness (s is shown large for clarity) [2]. 33

Figure 4.4: Film unsharpness [2].The density curves are magnified along the X-axis for clarity. (a) density distribution across image of sharp edge, assuming U_f=0, (b), (c) and (d) density distribution due to film unsharpness. (a) theoretical; (c) with grain; (d) smoothed. 36

Figure 4.5: Curve of U_f against radiation energy, for typical radiographic film (experimental) [2]. 37

Figure 4.6: Inverse Square law [2]. 37

Figure 4.7: Distortion of image of elongated void due to radiation beam angle [2]. 37

Figure 4.8: A dielectric circuit [5]. 38

Figure 4.9: Relationship between the apparent charge and the energy p of the discharge [5]. 39

Figure 4.10: Discharge magnitude in pC versus applied voltage in kV as a function of discharge type or void size [6]. 41

Figure 4.11: E.R.A. Standard PD detector circuit [9]. 41

Figure 4.12: E.R.A. Modified PD detector circuit [9]. 42

Figure 4.13: E.R.A. Balanced PD detector circuit [9]. 42

Figure 4.14: (a) Discharges in voids in insulation; (b) Discharges in voids bounded on one side by conductor and the other by dielectric; (c) Corona discharges; (d) Contact discharges in a capacitive circuit [9]. 43

Figure 4.15: X-Y diagram of a void of limited dimensions, e.g. some square millimetres by 0,5 mm thickness [5]. 44

Figure 4.16: X-Y diagram of a discharge in a more extended void [5]. 44

Figure 4.17: X-Y diagram of a surface discharge, discharges in a large gap or a long interface [5]. 45

Figure 4.18: Dielectric bound voids yielding X-Y diagrams in figures 4.15 and 4.16 [5]. 45

Figure 4.19: Wave reflection at an interface [11]. 46

Figure 4.20: Refraction of a Longitudinal wave [11]. 47

Figure 4.21: Basic principle of ultrasonic testing with a compressional probe, (a) set-up (b) standard A-scan display. 49

Figure 4.22: Pulse-Echo Method illustrated with the corresponding oscilloscope display [11]. 49

Figure 5.1: Three types of porcelain post insulator samples donated by the manufacturer. 53

Figure 5.2: Linear electron accelerator [5]. 54

Figure 5.3: Schematic diagram of the X-ray set-up indicating the defect-to-film distance measurement. 56

Figure 5.4: Insulator inverted in a glass tank filled with a saturated saltwater solution so that only two sheds are exposed above the surface of the solution. (a) schematic diagram and (b) photograph. 58

Figure 5.5: Typical E.R.A. Input Unit used in the detection circuit. 59

Figure 5.6: Standard PD Detection circuit with high voltage components and earthing visible. 60

Figure 5.7: Standard PD Detection circuit with E.R.A. Discharge Detector Model 3 and Control Gear clearly visible in the foreground. 60

Figure 5.8: Surface discharges on the base of insulator 2 during PD detection. (a) at 13.5kV and (b) at 42kV. 62

Figure 5.9: Dismantled 40kHz ultrasonic burglar alarm transducer. 65

Figure 5.10: (a) Pulse-echo experiment with transmitter and receiver mounted on M20 (20mm) bolt which is threaded into the insulator metal insert, and (b) view of the transmitter and receiver on the M20 bolt with oscilloscope and function generator leads attached. 65

Figure 5.11: Change of flight experiment with transmitter and receiver mounted on separate lead electrodes each geometrically 180^0 apart on the insulator circumference. (a) experimental set-up and (b) close up of a lead electrode with the transducer mounted on it. 67

Figure 6.1: X-ray images of (a) 22kV 620mm creepage and (b) 33kV 1120mm creepage insulators showing the position of their insert holes relative to the insulator sheds with no metal inserts fitted. 69

Figure 6.2: Artistic impression of the embedded electrode portion showing, (a) focus areas within the sulphur cement used to give the location of voids and (b) points of small radius curvature on mild steel insert. 70

Figure 6.3: X-ray image of sample insulator 2. (a) digital image at 0^0, (b) artistic impression of embedded electrode area at 0^0, (c) digital image at 90^0, (b) artistic impression of embedded electrode area at 90^0. 72

Figure 6.4: X-ray image of sample insulator 3. (a) digital image at 0^0, (b) artistic impression of embedded electrode area at 0^0, (c) digital image at 90^0, (d) artistic impression of embedded electrode area at 90^0. 73

Figure 6.5: X-ray image of sample insulator 4. (a) digital image at 0^0, (b) artistic impression of embedded electrode area at 0^0, (c) digital image at 90^0, (d) artistic impression of embedded electrode area at 90^0. 73

Figure 6.6: X-ray image of sample insulator CX2. (a) digital image at 0^0, (b) artistic impression of embedded electrode area at 0^0, (c) digital image at 90^0, (d) artistic impression of embedded electrode area at 90^0. 74

Figure 6.7: X-ray image of sample insulator CX1. (a) digital image at 0^0, (b) artistic impression of embedded electrode area at 0^0, (c) digital image at 90^0, (d) artistic impression of embedded electrode area at 90^0. 74

Figure 6.8: X-ray image of sample insulator A. (a) digital image at 0^0, (b) artistic impression of embedded electrode area at 0^0, (c) digital image at 90^0, (d) artistic impression of embedded electrode area at 90^0. 75

Figure 6.9: X-ray image of sample insulator B. (a) digital image at 0^0, (b) artistic impression of embedded electrode area at 0^0, (c) digital image at 90^0, (d) artistic impression of embedded electrode area at 90^0. 75

Figure 6.10: X-ray image of sample insulator C. (a) digital image at 0^0, (b) artistic impression of embedded electrode area at 0^0, (c) digital image at 90^0, (d) artistic impression of embedded electrode area at 90^0. 76

Figure 6.11: X-ray image of sample insulator CX. (a) digital image at 0^0, (b) artistic impression of embedded electrode area at 0^0, (c) digital image at 90^0, (d) artistic impression of embedded electrode area at 90^0. 76

Figure 6.12: X-Y diagram of PD in insulator sample 2. 83

Figure 6.13: X-Y diagram of PD in insulator sample 3. 83

Figure 6.14: X-Y diagram of PD in insulator sample 4. 84

Figure 6.15: X-Y diagram of PD in insulator sample CX2. 84

Figure 6.16: X-Y diagram of PD in insulator sample CX1. 85

Figure 6.17: X-Y diagram of PD in insulator sample A. 85

Figure 6.18: X-Y diagram of PD in insulator sample B. 86

Figure 6.19: X-Y diagram of PD in insulator sample C. 86

Figure 6.20: X-Y diagram of PD in insulator sample CX. 87

Figure 6.21: Oscilloscope traces of the reflected waves received by the Receiver transducer for (a) M20 bolt in air, (b) M20 bolt in sample insulator A and (c) M20 bolt in sample insulator CX. 88

Figure 6.22: Zoom of the first 2.5 time divisions of figure 6.21. 89

List of Tables

Table 2.1: Summary of flaws found in each of the four photographed insulators. 16

Table 3.1: Electric field strengths for the defined paths at 19kV and 1MV. 27

Table 3.2: Estimated values of maximum electric field strength inside voids on paths AB and CD. 28

Table 5.1: Expected total unsharpness values for the X-ray images of the three types of insulator samples. 55

Table 5.2: C_x values for each sample insulator inverted in a saltwater solution so that only the upper two sheds are exposed. 63

Table 6.1: Summary of the flaws identified from the X-ray images shown in figures 6.3 to 6.11. 71

Table 6.2: Summary of the inception and extinction voltages, and maximum discharge magnitude of each of the nine sample insulators. 78

Glossary of Terms

Contrast	The contrast of an X-ray image is the relative brightness between the image and the adjacent background.
Exposure, E	The dose of X-ray radiation striking the emulsion of the X-ray film in *Roentgen* or *C/kg* (SI unit).
Extinction Voltage	The AC terminal voltage at which the discharges extinguish if the voltage is decreased after discharges have started.
Gradient (of an X-ray film)	Different X-ray film types have unique characteristic curves of density versus exposure (D/Log E curve). The steeper the gradient of the curve, G_D, at a particular point on the curve that relates to a corresponding exposure, the higher the contrast on the radiograph.
Graininess	The visual appearance of the lack of homogeneity of density on a processed radiograph is called "graininess".
Half-value layer	The thickness of a material which will absorb one-half of the intensity of the radiation.
Inception Voltage	The AC terminal voltage across the sample at which discharges start to occur when the voltage is increased.
Density (Photographic)	When an X-ray image is viewed on an illumination screen the image observed is made up of areas of different brightness, which is indicative of the variation in the local densities of the developed emulsion. The higher the density,D, the darker the image.

Introduction

ESKOM embarked on a programme to supply cost effective electricity to all South Africans. One of the techniques developed to assist in this challenge of mass electrification makes use of the single-wire earth return (SWER) principle. SWER lines operate at 19kV phase-to-earth and are teed-off existing 33kV distribution networks [1]. These lines use 33kV capless porcelain line post insulators.

In this chapter the history of porcelain insulators is discussed, the background of the investigation is given and the aims and structure of this thesis are stated.

1.1 A Brief History of Porcelain as a High Voltage Insulator

Prior to 1878 porcelain was mainly used to insulate telegraph lines [2]. With the advent of electricity supply to consumers in the 19th century, the first power line insulators were scaled-up copies of the telegraph porcelain pin types.

These power lines were plagued by outages caused by the serious shortcomings of these insulators in a power distribution environment. The problems experienced were:

- puncture by electric stresses of ceramics which contained pores or flaws,
- cracks caused by differential expansion or corrosive effects in metal or cement, and
- flashover from dirt in combination with humidity.

These problems initiated, a succession of advances and retreats rather than an orderly progression, and continues an erratic course up to the present time. Porcelain went through a massive wave of evolution between the 1890's and the 1930's [3]. It established itself as the superior material when demand for high voltage insulators increased at the turn of the 20th century. By the 1970's process, design and standards were better established and manufacturers put their focus on quality and productivity.

Porcelain as a high voltage insulator now shows an incomparable study of more than a hundred years of evolution in process and engineering. With recent achievements contemporary porcelain insulators offer significant advantages. Benefits compared to

traditional porcelain insulators, includes flexible design, convenient prototype manufacturing, short lead-times, proven reliability and widespread established standards.

1.2 General Background to this Investigation

In 1986 a different design of porcelain line post insulator became commercially available. Previous insulators had an external metal electrode at the insulator base, but the new design uses substantially less metal, as an embedded electrode is fitted into the insulator's base. The capless (embedded electrode) and the capped (external electrode) insulators can be seen in figure 1.1.

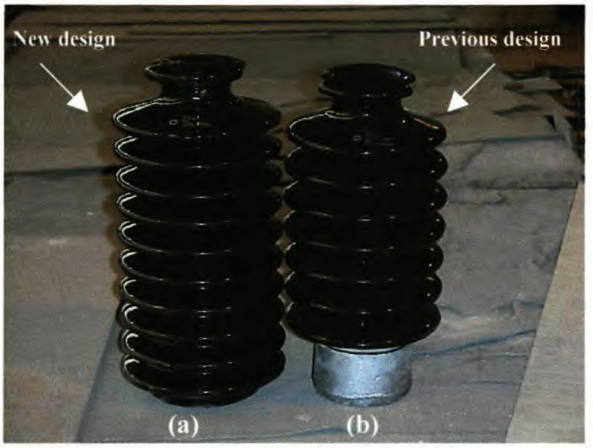

Figure 1.1: Porcelain line post insulators, (a) a 33kV capless 4kN (900mm creepage) insulator and (b) a 33kV capped 4kN (786mm creepage) insulator.

Various models of the capless porcelain line post insulator are locally produced and are used by ESKOM on their three phase and single-wire earth return (SWER) power lines. This study is based on the 22kV 4kN (620mm creepage) insulator, 33kV 4kN (900mm creepage) insulator, and the 33kV 4kN (1120mm creepage) porcelain post insulators with embedded electrodes as shown in figure 5.1.

Unexplained failures occurred in 2000 on the 33kV SWER power lines in ESKOM's Southern Region. During a meeting held on 14 May 2000 it was reported that approximately ten 33kV (4kN, 900mm creepage) line post insulators had failed during

the previous few months. Typically, the broken insulators resulted in the live conductor hanging just above the ground creating a potentially lethal condition.

The insulators used on these lines were of the type shown in figure 1.1(a). This was a new design with the metal spindle for fixture to the cross-arm directly embedded into the insulator's porcelain base. The previous design, shown in figure 1.1 (b) had an external electrode at the insulator's base.

A typical failed insulator recovered from these lines had the lower four sheds of the the ten shed insulator completely shattered, resulting in the line-drop described above. At the above mentioned meeting it was surmised that the insulator failure was due to lightning. Most of the subsequent failures showed signs of lightning damage to the insulators.

A recovered fragment of a damaged insulator is shown in figure 1.2. This insulator is suspected of breaking under mechanical stress under wind loading conditions (and not due to lightning in this case). However, inspection of the fragment showed evidence of partial discharge activity in the form of electrical treeing in the vicinity of the sulphur cement to porcelain interface. The sulphur cement has the shape of the insert hole, which has a flat top with a small radius of curvature at the edges.

Another interesting feature was an extensive stress fracture (see section 2.2) that was filled with sulphur cement. A mechanical fault plane, involving this stress crack, covers 60% of the insulator's diameter. The fault plane was present in all failed insulators.

The hypothesis can thus be stated (also made during the above mentioned meeting) that the partial discharge activity occurred at power frequency voltage and eroded a path through the insulator and when exposed to wind loading or lightning the insulator shattered.

Although the above failure was due to wind loading, it is suspected that a severe lightning stroke would also have caused failure.

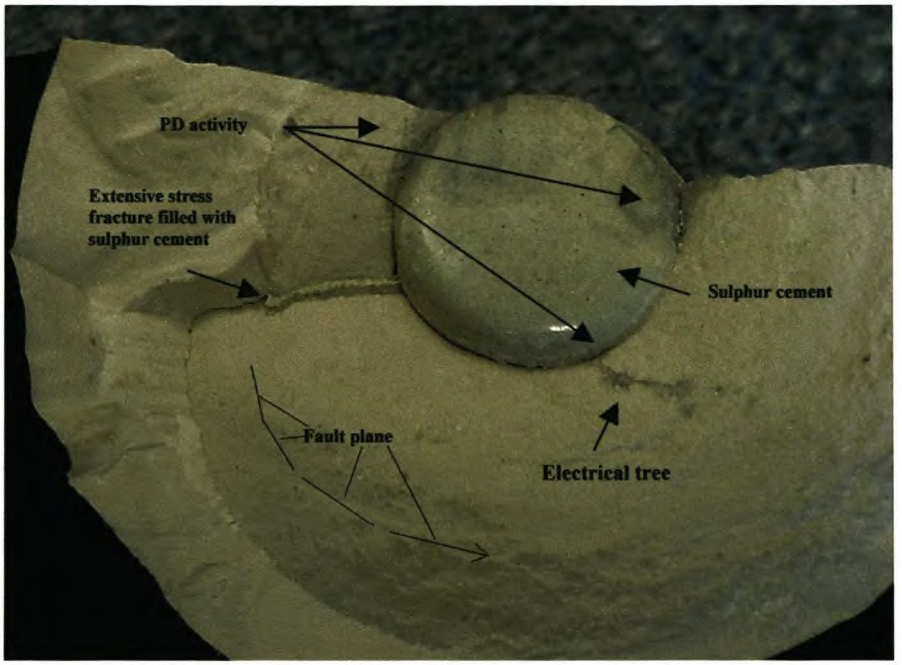

Figure 1.2: A fragment of a capless porcelain post insulator, which failed under windloading. The photograph shows PD activity at the sulphur cement to porcelain interface and sulphur cement that has filled an extensive stress fracture. Also visible is the fault plane of the failed insulator.

The voids that cause PD activity are thought to be due to the geometry of the insert hole that houses the embedded electrode. The top of the hole was flat with small radius of curvature at the edges leading to stress fractures as a result of the drying out during the insulator manufacturing process. The shape of the top of insert hole was subsequently changed to a semicircular cross-section in the hope that this would reduce the stress fracturing. At this time the manufacturer provided no distinguishing features for identification of insulators with the different insert hole shapes.

1.3 Aims of the Thesis

It was hypothesised that the change in insulator design, specifically the insert hole and embedded electrode in combination with the surrounding insulator materials, had led to the partial discharge activity in this region of the insulator. The manufacturing process, materials used, and the electric field of the insulator would be investigated. Non-destructive testing techniques (NDT) would then be considered for the detection of internal flaws in the insulators.

The aims of this work are:

- To identify NDT techniques that will most likely detect internal flaws in the capless porcelain line post insulator.
- To evaluate these NDT techniques through experimentation, to determine their effectiveness in detecting insulator internal flaws.
- To comment on the most suitable NDT technique for incorporation into the quality control process of these insulators.
- To indicate further work required for insulator NDT quality control and confirmation of the failure mode of these insulators.
- To review the insulator manufacturing process and materials used for the purpose of finding the possible cause/s of void formation in the embedded electrode region of the insulator.
- To determine whether a void in the vicinity of the embedded electrode will experience PD activity at nominal system voltage and/or under lightning conditions using an electric field simulation software package.

It should be noted that it is not the aim of this thesis to explain the failure mode of the insulators, although wherever evidence that pertains to the possible failure mode of these insulators presents itself this will be mentioned.

1.4 Structure of this Thesis

Chapter 1: An introduction to the problem experienced with the porcelain post insulator with a users perspective of the reason for failure and the aims of the thesis.

Chapter 2: The materials, their dielectric properties and the manufacturing process of the capless porcelain line post insulator are discussed giving the physical location and the causes of internal flaws.

Chapter 3: The electric field inside the insulator is analysed using computer simulation software and specific reference is made to

the effect of a void on the electric field. Studies are conducted at the nominal system voltage for a SWER powerline and 1MV to simulate lightning potential.

Chapter 4: The theory of the three non-destructive testing (NDT) techniques used in this thesis are described. The techniques are industrial radiography, partial discharge detection and ultrasonic testing.

Chapter 5: The three NDT techniques introduced in chapter 4 are used in experiments to determine whether voids are present in the nine sample insulators.

Chapter 6: The results obtained from the NDT experiments are presented and the results analysed. The validity of the NDT methods as tools for identifying internal flaws within the sample insulators are commented on.

Chapter 7: The study conducted on the capless porcelain line post insulator is reviewed and final concluding remarks and recommendations are made.

Appendix A: Reference tables and operating procedure for the E.R.A. Discharge Detector Model 3.

Appendix B: Acoustic characteristics of some non-piezoelectric materials.

Appendix C: Experimental results from PD detection monitoring of the nine sample insulators.

References

1. Ferguson,I.A. et al., "Distribution Standard Part 4: MV Reticulation Section 6: 19kV Single-Wire Earth Return (SWER) Overhead", ESKOM Distribution Standard, August 2003.
2. Looms,J.S.T, "Insulators for High Voltages", IEE Power Engineering Series 7, Peter Peregrinus Ltd, London, UK, 1990.
3. Axelson, R et al., "Development Trends Regarding Improvements of Porcelain Insulators", IEEE Volume 1 October, 1998.

The Materials and Process of Manufacture of Capless Porcelain Line Post Insulators

In the previous chapter the background relating to the failure of the capless porcelain line post insulators was introduced. As it appeared that manufacturing flaws may have an influence on these failures, it is necessary to investigate the materials and processes used in the manufacture of the insulators. The location and causes of the internal flaws are also investigated.

2.1 The Constituents of Ceramic Materials

The main body of the porcelain used for the manufacture of insulators is a mixture of the following raw materials mixed together in the proportions indicated below:
Ball Clay 25%; Kaolinite 19%; Silica 28% and Potassium Feldspar 28% [1].

Ball Clay

The term "ball clay" is derived from the cubes or balls in which the clay used to be during mining operations in the United Kingdom. The ball clay is sourced from the farm Vrede in Stellenbosch and is characterized by its fine grain size and high organic content [1]. Ball clay has a high plasticity and dry strength. Its disadvantages are its fired colour (sandy brown) and low refractoriness due to high percentages of alkalis and iron content.

Kaolinite

This clay, also known as Crous clay, occurs naturally and is essentially composed of the clay mineral kaolinite with small amounts of silica, mica, feldspar and partly decomposed feldspar, all from native rock from which the clay was formed [1]. Its fired colour is creamy (off white) due to its low content of colouring impurities (iron and titanium compounds).

Silica

Silica occurs in nature as quartzite, ganister and silica sand [1]. In ceramic bodies silica reduces the drying shrinkage of the body and also reduces the plasticity. During firing it "opens up" the body to allow for gases to escape without distorting the ware,

and combines with the fluxing ingredients to form a glass, which is responsible for the strength of the ware. Its fired colour is white.

Potassium Feldspar

Potassium Feldspar or "orthoclase" contains some soda feldspar, iron oxide and quartz [1]. This material is used as a flux and it therefore lowers the fusion temperature of the mixture to which it is added. The materials generally regarded as fluxes are high in alkali content. Its fired colour is white.

2.2 The Manufacturing Process of Porcelain Insulators

The manufacturing process entails the preparation and mixing (sliphouse), turning, glazing, firing, cementing and quality control and testing.

Sliphouse

This is the first step of the manufacturing process where the raw materials are individually refined and brought into specification after which they are mixed into a homogenous body slip [1]. Refining implies grinding and screening. The silica and feldspar are milled (ground), and the ball clay and kaolinite are sieved (screened) to obtain their respective specified particle sizes.

Next the separate raw materials are mixed together in the appropriate proportions to form a homogenous body slip. The body slip then passes through the filter pressing stage, where it is de-watered producing filter press cakes. Wet and dry sections of the filter press cakes are then mixed together, extruded and cut into approximately 400mm lengths for ease of loading and handling. The extruded lengths are then placed in the souring room (for 12 to 24 hours), which is an ageing process to improve the clay. After the souring room the extruded lengths are put through a de-airing extruder that removes the air from the clay under vacuum and compacts it into a dense homogenous tube. The homogenous tubes are then subjected to a drying process.

Turning

During the turning process the insulator is shaped from the extruded tube, as shown in figures 2.1 (a) and (b). This increases the surface area of the insulator and therefore the creepage distance, by the formation of the insulator sheds. During the turning stage the hole that houses the embedded metal insert at the base of the insulator is formed.

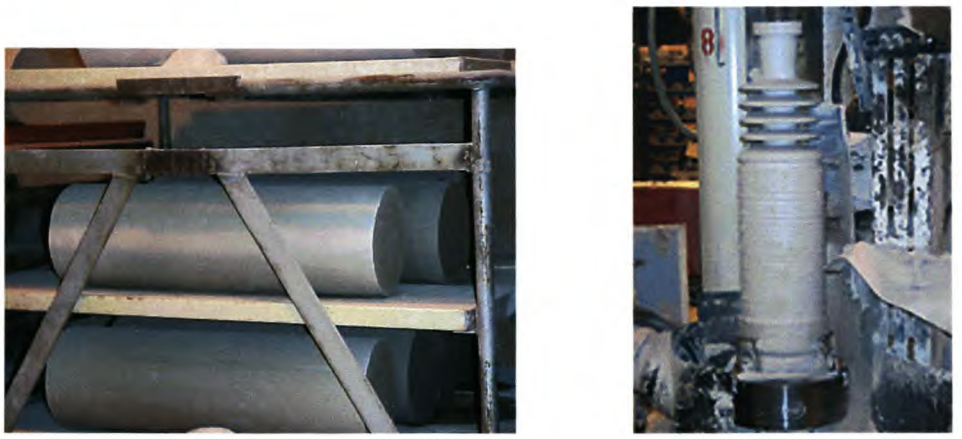

(a) (b)

Figure 2.1: (a) Extruded Tube ready for turning, and (b) turning in progress.

Glazing

The newly formed insulator is then passed through another drying process to remove the remaining moisture. After the insulator has cooled down it is inspected and the glaze is then applied by dipping the insulator into the glaze mixture [1]. This is a thin layer of "glass" which is applied to improve the strength of the insulator and to assist in keeping it clean during service. Glaze compositions are similar to glass with an oxide pigment colourant and have a lower melting point than the porcelain body to form a smooth surface. The insulator identifying markings are then applied. Figures 2.3 (a) and (b) show insulators prior to and after glazing respectively.

During a visual inspection of the insulator in figure 2.2 (a), a vertical crack the full height of the insulator as detected, resulting in the insulator being rejected.

The hole at the base of the insulator is coated with a combination of glaze and granulated porcelain as shown in figure 2.2 (b) and once fired provides a hardened rough surface for the sulphur cement to bond (grip) to the insulator's porcelain body.

Also shown in this figure are some stress fractures due to the drying and machining processes.

(a) (b)

Figure 2.2: (a) Insulator rejected due to crack prior to glaze application, and (b) insert hole at insulator base coated with unfired porcelain chips with stress fractures visible at the top of the hole.

Firing

The unfired insulators as shown in figure 2.3, are then placed in the kiln for a period of approximately seven days during which the temperature is increased from ambient temperature to 1200°C according to a firing schedule [1]. The fired insulators are then cooled down in a controlled manner with the kiln still in place. Figure 2.4 shows the extent of the shrinkage of the insulator body from just prior to glazing until after the firing process is completed.

(a) (b) (c)

Figure 2.3: (a) Insulators stacked ready for glazing, (b) glazed insulators stacked and ready for firing, and (c) kiln lowered over stacked insulators.

Laboratory

The laboratory plays a vital role in quality control throughout the entire manufacturing process [1]. Physical and chemical tests are performed by the laboratory. Physical tests include bulk density and specific gravity of raw materials, dimensional change (shrinkage), strength – modulus of rupture, fluid properties of slips, particle size and porosity. Chemical tests refer to the chemical analysis of raw materials.

Figure 2.4: Insulator shrinkage due to drying out.

2.3 Inspection and Screening Tests on Completed Porcelain Components

The completed glazed porcelain insulators are now inspected and tested in accordance with IEC 168.

The specification requires visual inspections to be carried on porcelain post insulators for compliance to drawings with respect to the mounting of metallic fittings, glaze colour, glaze free from cracks and other defects, glaze smoothness, spots without glaze, chips, inclusions and pinholes in the glaze [2]. The manufacturer performs a visual inspection on each insulator. Rejects are identified and recorded and insulators to be re-glazed are identified [1].

Mechanical shock testing is performed by the manufacturer on each fired insulator by placing it horizontally and hitting the insulator on the base with a plastic mallet sending shock waves down the unit. Any defect will cause the insulator to crack or the sheds to come apart [1].

2.4 Assembly of the Insulator

The metal fixing attachment has to be fitted to the porcelain insulator. The material used for this purpose can be a lead antimony alloy, Portland cement or sulphur cement. Sulphur cement as used in the insulators under investigation, consists of sulphur, silica flour and a sand of a specific particle size. The three materials are mixed together in the appropriate proportions and heated to 150^0C. Since sulphur has

a melting point of 112.8^{0}C it acts as the wetting medium [7]. Figure 2.5 shows the heated sulphur cement mixture. The mixture is kept at 150^{0}C and is agitated to keep the silica and sand suspended in the molten sulphur. Once the mixture cools the sulphur solidifies and binds the silica and sand together. The advantage of sulphur cement over Portland cement is that the setting period is much shorter.

Figure 2.5: Heated sulphur cement mixture.

The insulator is inverted so that the metal insert hole is facing upwards. The metal insert centreing jig is placed over the base of the insulator with the metal insert and the sulphur cement is poured into the cavity to cement the metal insert to the main body of the insulator. The suphur cement sets rapidly (two minutes as sulphur solidifies at 112.8^{0}C) as it cools and is allowed to completely harden overnight. The cementing process is illustrated in figure 2.6. The insulator is now ready for the routine mechanical tests.

2.5 Routine Tests on the Complete Insulator

The completed insulators are subjected to routine electrical and mechanical tests in accordance with IEC 60168.

According to IEC 60168 the porcelain post insulator can be classified as a design category 3 insulator (puncture proof) and according to table 5 (routine tests applicable to post insulators) of the standard, no routine electrical test is required [2]. The manufacturer also performs no routine electrical tests.

This specification also states that the normal mechanical test load shall be equal to 50% of the specified mechanical failing load [2]. The minimum specified mechanical failing loads for line post insulators are available in IEC 60273 [3]. The test load shall be applied in four mutually perpendicular directions, each for a minimum time of three seconds. The insulator is mounted on a rigid base, and the load applied at the free end of the insulator in a direction perpendicular to the axis of the insulator. Alternatively, by agreement between the purchaser and the manufacturer at the time of ordering, a bending test with a load up to 70% of the specified mechanical failing

load may be applied in more than one direction, each for a time of three seconds. By agreement between the purchaser, ESKOM, and the manufacturer, a cantilever test is performed routinely on each insulator to 60% of minimum specified failing load [1]. The cantilever test is shown in figure 2.7.

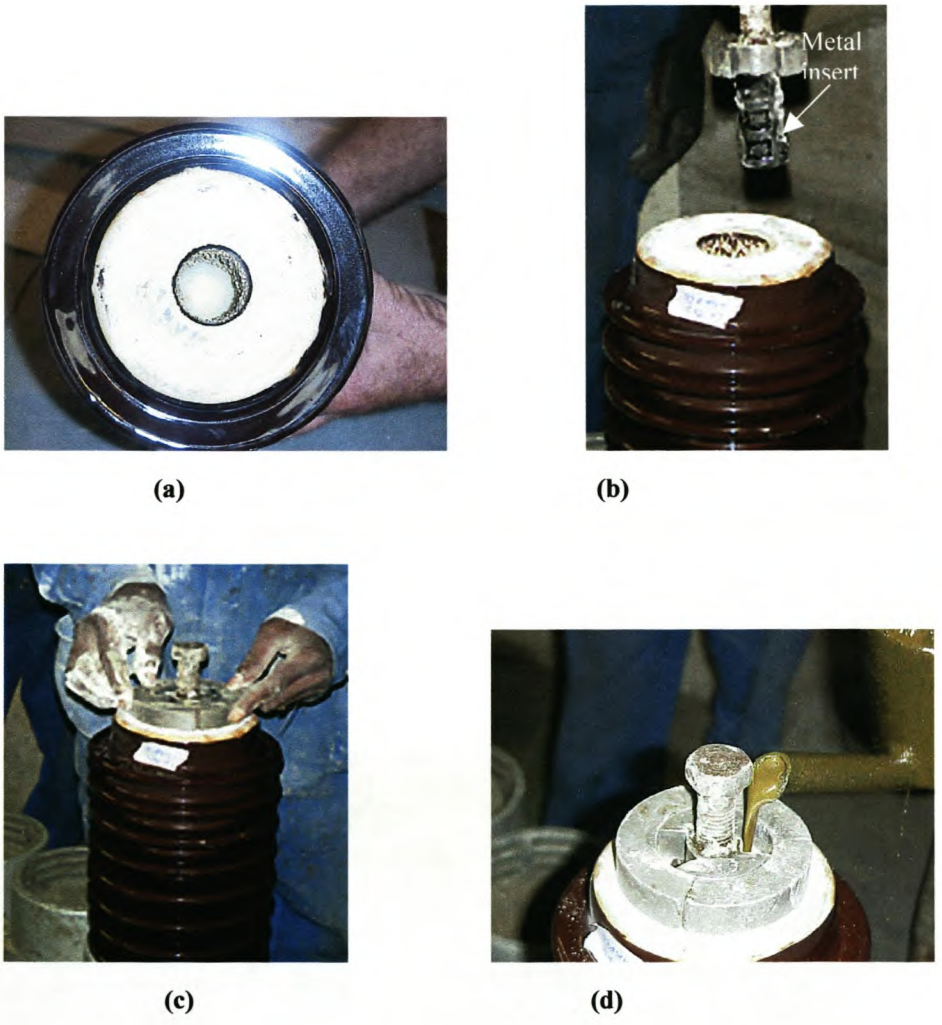

Figure 2.6: (a) Glazed insulator revealing hole for metal insert, (b) insertion of metal insert, (c) jig is positioned over insulator base, and (d) sulphur cement is poured into the cavity.

(a) (b)

Figure 2.7: (a) Insulator is bolted to test table and the test arm is positioned against the free end of the insulator body, and (b) insulator deflecting under cantilever loading.

2.6 Discussion of the Manufacturing Process

In this section the observations made in the previous sections are analysed to obtain information that would assist in reaching the main objective of this thesis.

2.6.1 Location and Types of Internal Flaws

Figure 2.2 (b) reveals stress fractures at the top of the hole at the base of the insulator. When the cementing in section 2.4 takes place these fractures will either be filled with the sulphur cement or even worse air can become entrapped. Both the air and the sulphur cement have permittivities that are lower than that of porcelain and under the application of an alternating voltage electric field enhancement will occur with possible discharges inside these fractures.

Figures 2.8 (a), (b), (c) and (d) consist of four damaged insulators photographed during a visit to the insulator factory. They do not represent a specific batch of insulator samples, but are only presented here as evidence of the types of internal flaws that are typically found with this type of insulator. Figures 2.8 (a), (b) and (c) are large fragments of three porcelain post insulators that were loaded to failure during cantilever testing and figure 2.8 (d) is a cut through of a porcelain post insulator (the metal insert has not yet been cemented into position). The pencil markings on figures 2.8 (b) and (c) indicate that during cantilever testing, failure occurred well in excess of the specified minimum bending failure load of 4kN. This

indicates that they are mechanically sound, yet their electrical performance is in question due to their internal flaws.

Table 2.1 is a summary of the different types of flaws found in each of the four photographed insulators.

Table 2.1: Summary of flaws found in each of the four photographed insulators.

Figure no.	Void in Sulphur cement	De-bonding	Void in Porcelain	Porcelain stress fractures
2.8 (a)	yes	yes	no	yes
2.8(b)	yes	yes	no	no
2.8 (c)	yes	no	no	yes
2.8 (d)	Not applicable	Not applicable	yes	yes

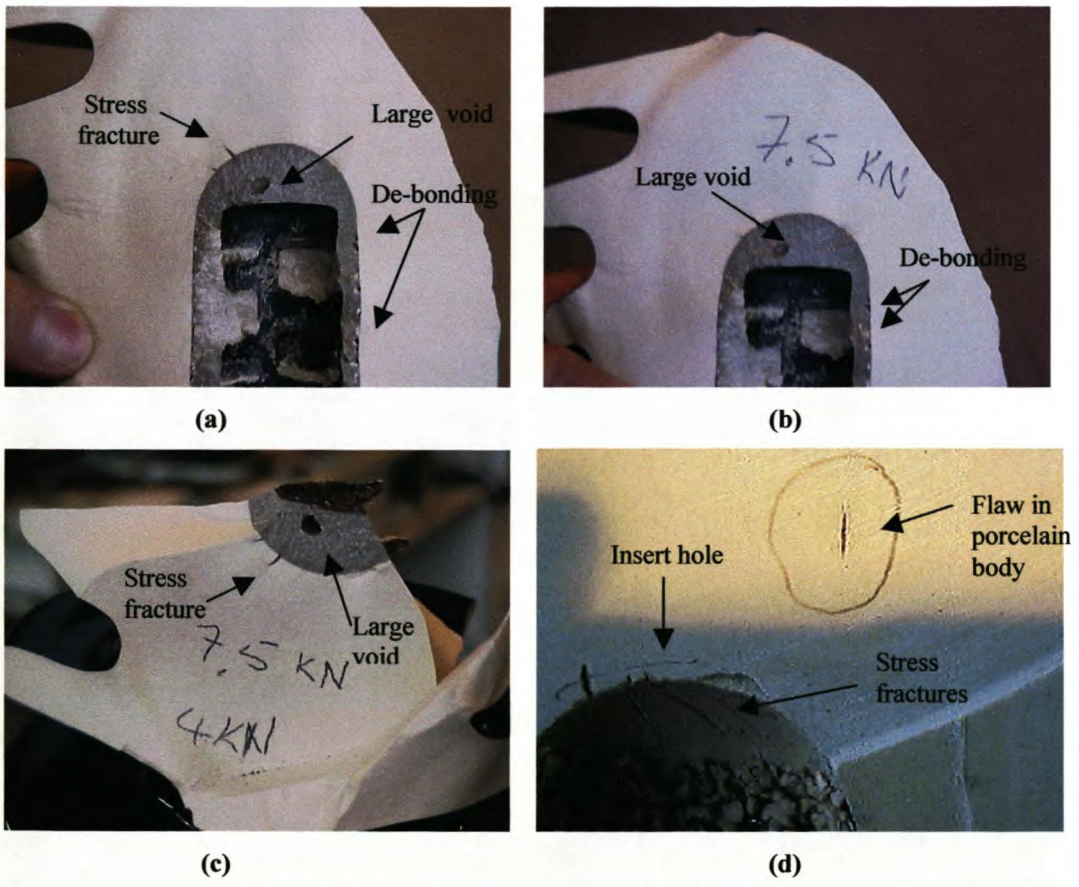

Figure 2.8: (a), (b) and (c) are failed insulators showing clear evidence of internal flaws.

2.6.2 The Causes of Internal Flaws

The voids in the sulphur cement are due to this fast setting cement as air entrapment cannot easily be prevented and no provision is made during the manufacturing process to prevent air entrapment.

De-bonding between the sulphur cement and the porcelain body of the insulator is less obvious than void formation in the sulphur cement as can be seen in figures 2.8 (a) and (b). In figure 2.2 (b) it is clear that the manufacturer has made what appears to be an adequate surface for the sulphur cement to bond (grip) to the porcelain, but de-bonding still occurs. In chapter 6 further evidence of de-bonding will be seen in the X-ray images.

The cause of the stress fractures at the top of the metal insert holes seen in figures 2.2 (b), 2.8 (a), (c) and (d) are a function of the geometry of the hole and the drying out of the porcelain.

The cause of the flaw in the main porcelain body of the insulator is unknown. Porcelain is a very stable material and it can be assumed that discharges of many thousands of discharges of picocoulombs (pC) are harmless [6]. Even in view of this latter statement it is suggested that the cause of such a flaw be investigated.

It is not the intention of this thesis to offer solutions to these manufacturing problems.

2.6.3 Dielectric Materials Used

The two non-metallic materials that are used in the manufacture of these porcelain post insulators are porcelain and sulphur cement. Porcelain is a tried and tested dielectric with a relative permittivity, ϵ_r, of 6 – 7 [4]. Sulphur Cement on the other hand is not a recognised dielectric.

Sulphur has a relative permittivity, ϵ_r, of 3.69 – 4.45 and a loss factor, tanδ, of 0,0005 [4]. A good dielectric has a tanδ < 10.10^{-4} [5]. Permittivity and tanδ values are not available for the other sulphur cement ingredients, silica flour and sand.

A cylindrical sample of hardened sulphur cement was prepared by the insulator manufacturer for electrical testing. This sample was rather large and had to be cut into smaller slices. The smallest slice that could be cut from this sample without the sulphur cement fracturing had a thickness of 10.65mm. A three-electrode arrangement (guard electrode included) was used to measure the insulation resistance of the sulphur cement slice, from which the resistivity of the cement could then be calculated. The measuring electrode had a diameter of 50mm. A 10kV megger was used to measure the insulation resistance of this slice and each time a reading was taken the megger displayed, >500GΩ. Two further sulphur cement slices of 12.7mm and 13mm were also meggered for confirmation of the 10.65mm slice megger reading and gave the same result. The resistivity could therefore not be calculated, as a definite insulation resistance reading could not be obtained with the available megger. It was concluded from the megger tests that the sulphur cement is a dielectric.

The capacitance of the 10.65mm thick slice of sulphur cement was measured using the same three-electrode configuration and an AVO-Delta 2000 10kV Automated Insulation Test Set. The permittivity of the sulphur cement was then determined to be 3.95, which is within the range (3.69 – 4.45) of the permittivity of sulphur.

Conclusion

- Stress fractures occur in the porcelain at the top of the metal insert hole due to the geometry of the hole and the drying out of the porcelain.
    - Three of the damaged insulators photographed had stress fractures.
    - The stress fractures found, were less severe than those seen in figure 1.2. This could be attributed to a change in the shape of the top of the insert hole which is now semicircular in cross section.
    - Stress fractures are as a result of the insulator design and as such could be present in most of the insulators manufactured.

- Sulphur cement will fill the stress fractures or air will become entrapped in them and this can lead to discharge activity.
- Stress fractures can be detected by a visual inspection prior to the fitting and cementing of the metal insert.

- De-bonding occurs in places at the sulphur cement to porcelain interface.
  - Two of the insulators photographed exhibited de-bonding at their sulphur cement to porcelain interface.
  - De-bonding is a result of the insulator design and as such could be present in most of the insulators manufactured.
  - De-bonding leads to the formation of voids and this can lead to discharge activity.
  - Existing quality control during the manufacturing process is unable to detect de-bonding.

- Voids form inside the sulphur cement during the manufacturing process.
  - Three of the insulators photographed had large voids present in their sulphur cement.
  - Void formation in the sulphur cement is as a result of this fast setting cement and the lack of provision made in the production process to prevent air entrapment. These voids could therefore be present in most of the insulators manufactured.
  - Sulphur cement is a dielectric and therefore voids can lead to discharge activity.
  - Existing quality control during the manufacturing process is unable to detect the voids in the sulphur cement.

- Voids can form in the porcelain body of the insulator.
  - Only one of the insulators photographed displayed a void in its porcelain body.
  - Void formation in the porcelain cannot be attributed to the insulator design and as such should not be present in most of the insulators manufactured.

- Porcelain is a very stable material and this insulator has a large solid porcelain body, therefore the presence of a limited void is harmless [6].

References

1. Van Niekerk,C, "Cullinan Industrial Porcelain Production Manual", in house technical manual, July 1994.
2. International Electrotechnical Commission (IEC) Standard 60168, "Tests on Indoor and Outdoor Post Insulators of Ceramic Material or Glass for Systems with Nominal Voltages Greater than 1000V", edition 4.2, 2001.
3. International Electrotechnical Commission (IEC) Standard 60273, "Characteristics of Indoor and Outdoor Post Insulators for Systems with Nominal Voltages Greater than 1000V", 1990.
4. Von Hippel,A.R, "Dielectric Materials and Applications", The MIT Press,1961.
5. Kreuger.F.H, " Industrial High Voltage", Vol. 1, page132, Delft University Press, 1991.
6. Kreuger,F.H., "Partial Discharge Detection in High Voltage Equipment", Butterworths, 1989.
7. Uvarov,E.B. et al., "The Penguin Dictionary of Science", Penguin Books, fifth edition, 1979.

Electric Field Simulation Study

As shown in chapter 2 the use of sulphur cement makes the insulator prone to void formation and this is also confirmed by the radiographic images in chapter 5. In this chapter the electric field inside the insulator is analysed using computer simulation software and specific reference is made to the effect of the voids on the electric field. The electric field simulation should indicate whether the internal voids experience discharge activity when exposed to 19kV r.m.s. (26.87kV peak) or 1MV impulse potential. The 19kV was chosen as this represents the phase-to-earth operating potential for a SWER overhead line configuration and the 1MV represents the magnitude of lightning potential.

This chapter makes use of the computer simulation study conducted by Visser and Borrill [1]. The study was limited to a void on the insulator's axis of symmetry.

An electric field simulation study was conducted in order to determine the potential distribution and electric field strengths in the dielectric material around the embedded metal insert at the base of insulator. The insulator was simulated at both voltages, firstly without and then with a void in the sulphur cement dielectric.

A 33kV 4kN (900mm creepage) capless porcelain line post insulator shown in figure 3.1 was chosen as the simulation test insulator.

Figure 3.1: 33kV 4kN (900mm creepage) capless porcelain line post insulator.

The SLIM finite element electrostatic software module [2] was used in the simulation studies. This software generates two dimensional (2D) static solutions, which is not ideal, as it does not allow the modelling of the cylindrical conductor. It was however considered suitable as the insulator is rotationally symmetrical and the region near the embedded electrode could be modelled accurately.

The simulation results obtained from this study and

conclusions are included in this chapter.

3.1 Software package

SLIM is a professionally engineered, fully integrated collection of software modules that provides facilities for the generation and solution of electromagnetic finite element models [2]. The SLIM 2D electrostatic module was used in this study and allows for the solution and post-processing of electric fields in the Cartesian and axis-symmetric geometries. The electrostatic modules are available from a menu driven user interface. The program uses window-based environments in which the software modules may be used concurrently and thus allow the user to move freely between tasks.

The generation of 2D meshes is achieved using semi-automatic, interactive or fully automatic, command driven routines [2]. The fully automatic, transparent mesh generation procedure was used, reducing user intervention in the definition of problem boundaries and level of discretisation, allowing full parametric model definition. The use of the fully automatic mesh generation also enables the user to interface the SLIM software with AutoCAD files [3]. This is necessary as the manufacturer's insulator profiles are AutoCAD files and time is saved if these files can be used.

The wide range of SLIM finite element solvers covers a broad base of electric field analysis. The solvers are supported by a series of interactive, graphical based data preparation tools [2].

The 2D static solution used includes the modelling of dielectric and semi-conducting materials with anisotropic permittivity and conductivity, and of perfectly conducting surfaces. Only materials with isotropic permittivity were used in this study [1].

The system provides a comprehensive, command-driven, windows based post processing system with an extensive graphical user interface to assist the user. Full facility for the display of the surface contours, line or block fills, or vector data as colour coded or scaled arrows is supported.

Information along complex paths defined in the post-processor can be displayed in graph form [2].

3.2 Preliminary Study

Visser and Borrill [1] tested the SLIM electrostatic module by simulating a simple configuration in order to gain confidence in the results obtained from the software package. An ideal parallel place capacitor consisting of three dielectrics was simulated and the SLIM results were compared with those obtained from mathematical calculations. The potential distribution, V, the electric field strength, E, and electric flux density, D, in each of the dielectrics were compared. The results of this comparison showed that the simulated and calculated values compared well with a maximum deviation of only 0.05%, showing that the simulated results are accurate.

3.3 Flow diagram

A flow diagram outlining the simulation method followed in the electric field simulations is shown in figure 3.2.

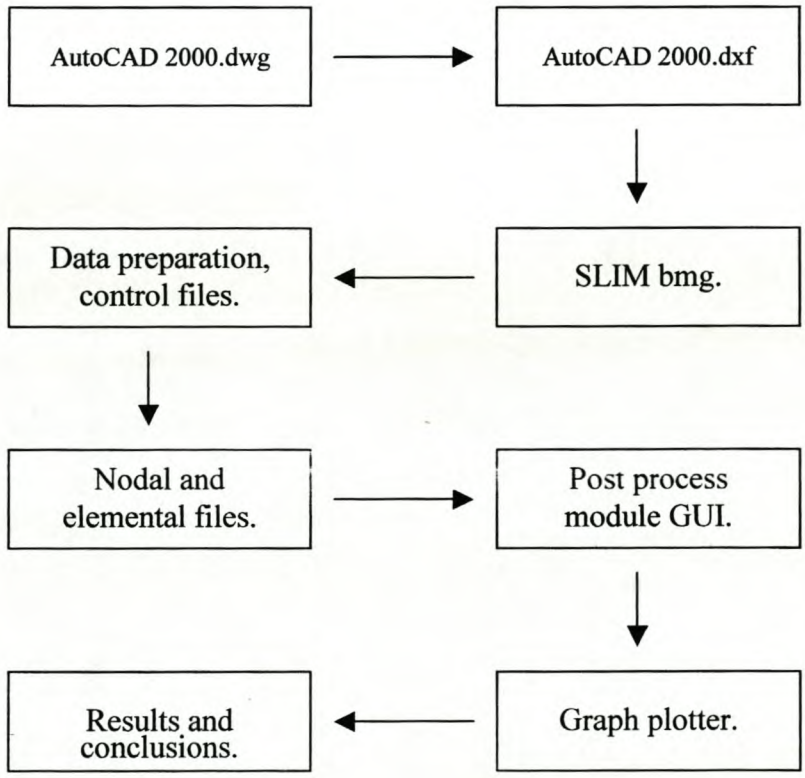

Figure 3.2: Flow diagram of simulation method followed [1].

3.4 Insulator Electric Field Simulation

3.4.1 Insulator profile

The 33kV insulator profile was received from the insulator manufacturer as an AutoCAD file. This file was then edited and interfaced with the SLIM electrostatic software module so that the simulations were based on actual geometric measurements [1]. The manufacturer and edited insulator profiles are shown in figure 3.3.

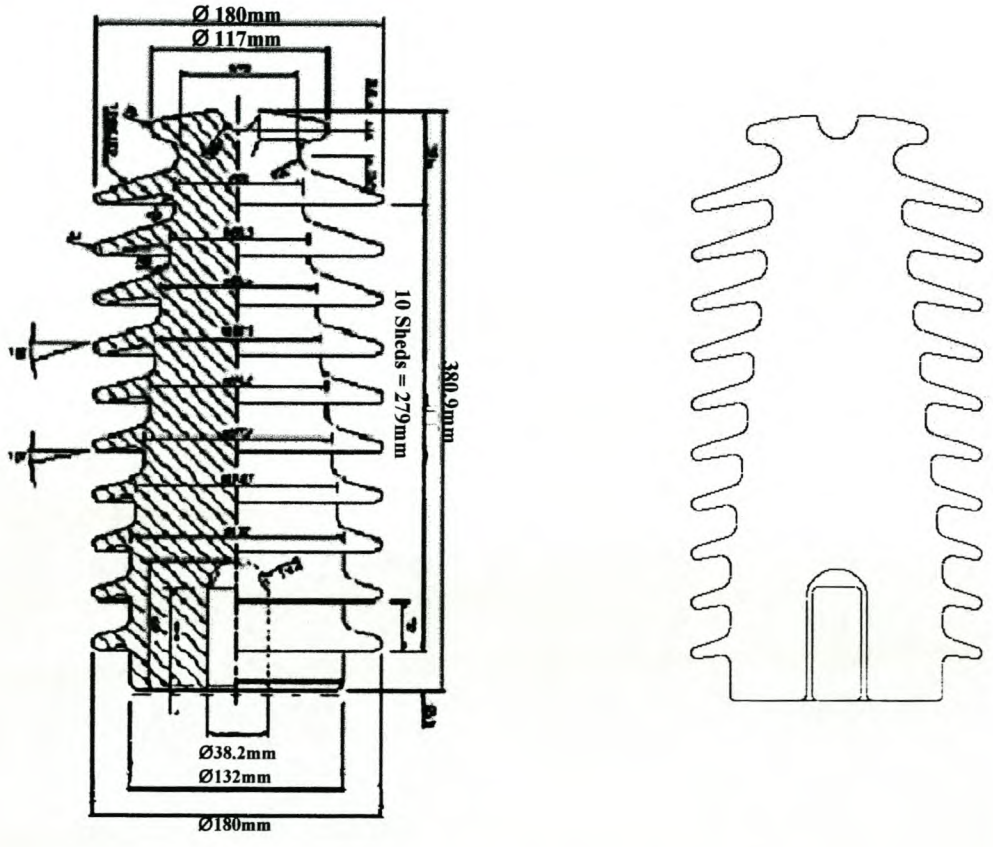

(a) (b)

Figure 3.3: Insulator profiles, (a) manufacturer and (b) edited for importing into SLIM [1].

3.4.2 Software Simulation

The insulator was simulated at 19kV without and then with a void inside the sulphur cement. The void was placed inside the sulphur cement above the embedded electrode (metal insert) on the axis of symmetry of the insulator. A blown up section of the base

of the insulator is shown in figure 3.4 where the porcelain body of the insulator, sulphur cement, embedded electrode and the void are clearly visible.

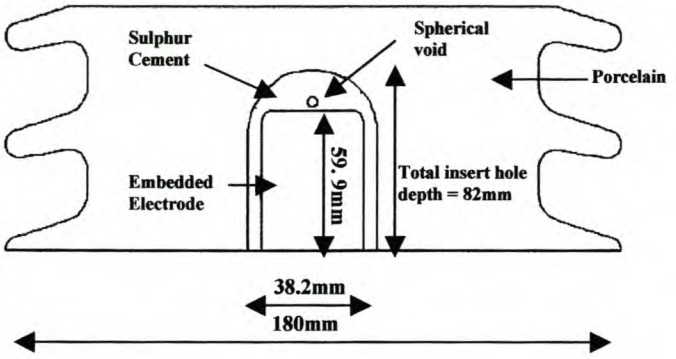

Figure 3.4: Blown up section of base of insulator with void visible in the sulphur cement.

The following permittivities obtained from chapter 2 were used in the simulation:

- Porcelain, $\varepsilon_r = 7$
- Sulphur cement, $\varepsilon_r = 3.95$
- 3mm diameter air filled void, $\varepsilon_r = 1$

A typically used conductor of diameter 6.35mm served as the high voltage electrode and the embedded electrode as the earth electrode. Both the conductor and embedded electrodes were assigned the conductivity of steel, which is selectable in the program. The conductor was modeled as a sphere to allow for the axis-symmetric simulation study. The field strength is depicted using field vectors and to be able to display the points of highest stress the lowest field vectors were eliminated. This is necessary to be able to identify the points of highest electrical field stress, as these would otherwise not be visible on the field vector display.

Once the field vectors are displayed, the areas of highest stress can be identified. In order to draw graphs of potential distribution and electric field strength for these highly stressed paths the software requires the user to define these paths. This is done by the drawing of simulation line through the dielectric to the electrode as shown in figure 3.5, so that the necessary data may be obtained [3].

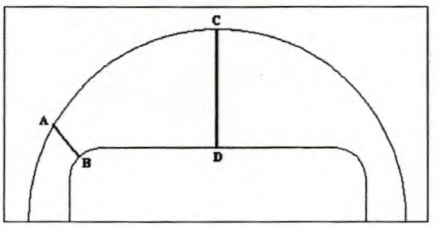

Figure 3.5: Data paths for the base of the insulator without void [1].

3.5 Simulation Results

This section will highlight the outcomes of the simulation study conducted by Visser and Borrill[1]. The results obtained are for the defined paths shown in figures 3.5.

Figures 3.6 (a) and (b) show clearly that there are three points of highest stress for the insulator and these are around the conductor surface at the top of the insulator and at the curved edges of the embedded electrode inside the insulator base.

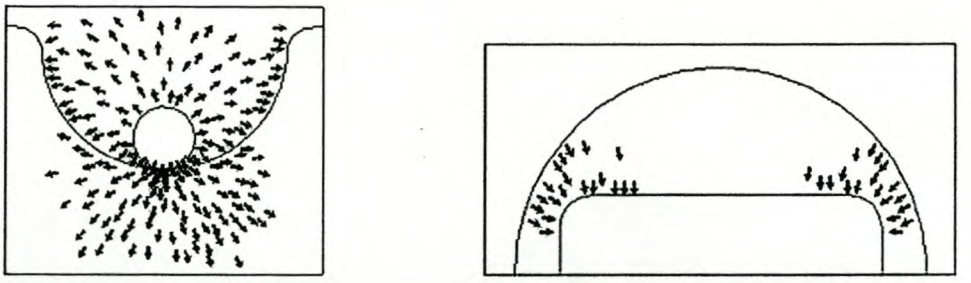

(a) **(b)**

Figure 3.6: Electric field vectors (a) at conductor surface and (b) inside sulphur cement [1].

The computed graphs for the electric field strength along paths AB and CD are shown in figures 3.7 and figure 3.8 respectively. It should be noted that the fields are reasonably uniform in these regions.

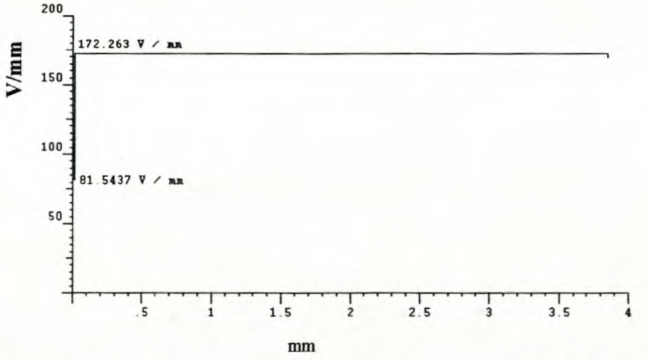

Figure 3.7: Electric field strength for path A to B at 19kv without a void [1].

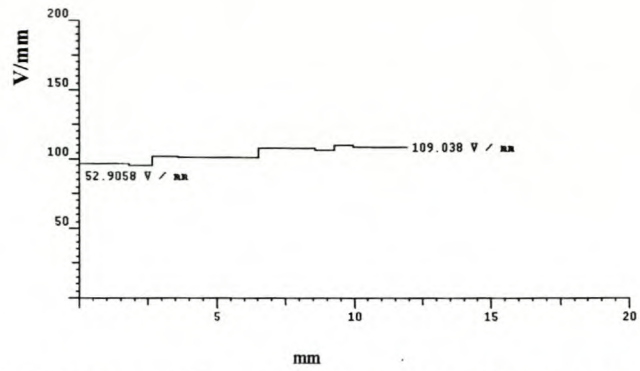

Figure 3.8: Electric field strength for path C to D at 19kV without a void [1].

From the 19kV simulation results the corresponding values for 1MV can be linearly extrapolated.

Attempts to simulate the presence of a 3 mm spherical void as indicated in figure 3.4 were unsuccessful as sufficient accuracy could not be obtained due to the small size of the void.

The results are summarised in table 3.1. In this table the r.m.s. values are converted to peak values and the linearly extrapolated values for 1MV are also given.

Table 3.1: Electric field strengths for the defined paths at 19kV and 1MV.

	$19kV_{r.m.s.}$		1MV
	E ($kV_{r.m.s.}$/mm)	E (kV_{peak}/mm)	E (kV/mm)
Path AB	0.172	0.243	9.053
Path CD	0.109	0.154	5.737

The value of the maximum field strength in a spherical void, should it exist in the regions of high electric field strength can be estimated, using field theory principles as given by Kreuger [4]. It can be shown that the existence of a gas void in a solid dielectric with a relative permittivity of ε_r raises the maximum field strength to a value E_{void}, where $E_{void} = \frac{3\varepsilon_r}{1+2\varepsilon_r} E$ and E is the average electric field strength that would exist in the solid dielectric just prior to the insertion of the void.

Based on this formula the maximum field strength in the voids along paths AB and CD would be as given in table 3.2, using $\varepsilon_r = 3.95$ (see section 2.6.3).

Table 3.2: Estimated values of maximum electric field strength inside voids on paths AB and CD.

	$19kV_{r.m.s.}$		1MV	
	E (kV_{peak}/mm)	E_{void} (kV_{peak}/mm)	E (kV/mm)	E_{void} (kV/mm)
Path AB	0.243	0.323	9.053	12.05
Path CD	0.154	0.205	5.737	7.636

3.6 Analysis of Results

The computed maximum electrical field strength values for normal power frequency energisation are all below the breakdown threshold for air under normal atmospheric conditions (3kV/mm). The values for lightning are well above this inception value.

A condition that would aggravate the situation with power frequency conditions would be the existence of a conducting pollution layer on the upper part of the insulator. This would bring the high potential closer to the metal insert area at the insulator base. Higher internal stresses would occur in the voids in the sulphur cement and partial discharge activity will result.

Conclusions

The evaluation of the SLIM 2D electrostatic software module and the analysis of the simulation results led to the following concluding remarks:

- Attempts to simulate the presence of a 3 mm spherical void as indicated in figure 3.4 were unsuccessful, as sufficient accuracy could not be obtained due to the small size of the void.
- The value of the maximum field strength in a spherical void along paths AB and CD were estimated, using field theory principles.
- The areas of highest electrical field stress inside the insulator were successfully identified.
- In the absence of a void the electric field strength is highest in the sulphur cement at the curved edges of the embedded electrode.
- When a void is inserted inside the sulphur cement, the electric field strength is highest inside the void. This is due to the void in the sulphur cement

experiencing field enhancement due to its permittivity being lower than that of the sulphur cement.

- The electric field strength inside the void when 19kV r.m.s. (26.87kV peak) is applied to the insulator is not high enough to cause a discharge inside the void.
- The electric field strength inside the void when 1MV is applied to the insulator will cause a discharge inside the void. The electric field strengths inside the 3mm void for paths AB and CD are 17.022 kV/mm and 10.788kV/mm respectively. Both of these electric field strengths are well above the 3kV/mm breakdown strength of air.
- A void near the curved edge of the embedded electrode where the electric field strength is high would create discharges of a greater magnitude than a void situated on the axis of symmetry of the insulator.
- The existence of a conductive pollution layer on the upper part of the insulator would initiate partial discharges in the voids in the sulphur cement under power frequency conditions.

References

1. Visser,J, "The Use of an Electrostatic Software Package to Simulate the Electric Stresses In and Around a Porcelain Post Insulator", B.Tech Thesis, Supervised by Borrill,L, Cape Technikon, South Africa, 2001.
2. Alstom Research and Technology Centre, "Slim Electromagnetic Engineering for Microsoft Windows 95+", NT4.0, 2000, UM-Slim-067, Manufacturers Manual.
3. Visser,J, Voss,E, and Borrill,L, "The Use of an Electrostatic Software Package to Simulate the Electric Stresses in and Around a Porcelain Post Insulator", South African Universities Power Engineering Conference, 2002.
4. Kreuger,F.H., "Industrial High Voltage", Delft University Press, Volume 1, 1991.

Non-Destructive Testing Techniques

This chapter describes the theory of the three non-destructive testing (NDT) techniques used in this thesis. These techniques are industrial radiography, partial discharge detection and ultrasonic testing.

4.1 Industrial Radiography

The discovery of X-rays by W.C. Roentgen in 1895 and the discovery of radioactivity by Becquerel in 1896 have lead to the development of industrial radiography [1]. One of the best-established and widely used non-destructive testing (NDT) methods is radiography. Radiography is the use of X-rays and gamma-rays to produce a radiograph of a specimen, showing any changes in thickness, defects (internal and surface), changes in structure, and assembly details [2].

Gamma-rays are electromagnetic radiation of exactly the same physical nature as X-rays [2]. Gamma-rays cannot be produced by an electrical apparatus as is the case with X-rays, but arise from the disintegration of the atomic nuclei within some radioactive substances. Since the energy of gamma-radiation emitted by a particular radioactive substance and its intensity cannot be controlled, X-ray radiography was chosen to examine the porcelain post insulator for internal defects.

The procedure for producing a radiograph is to have a source of X-ray radiation on one side of the specimen to be examined and a detector of the radiation (the film) on the other side [2]. X-rays are partially absorbed during the passage through a thickness of material and this enables it to produce a radiographic image. The energy of the radiation must be chosen so that sufficient radiation is transmitted through to the detector. The detector is a sheet of photographic film, held in a light-tight envelope having a very thin front surface, which allows X-rays to pass through. After the film has been exposed for the appropriate time the film is processed photographically. The film is then placed on an illuminated screen, where the differences in X-ray intensity in the X-ray beam transmitted through the specimen can be seen to be produced on the film as differences in blackening, which are seen on the illuminated film as differences in brightness.

Thinner sections of the specimen or cavities within the specimen absorbs less X-rays and will thus allow more X-rays to reach the film during exposure and will result in a higher film density giving a darker appearance on the illuminated film and vice versa.

4.1.1 Units of measurement

The quantity that expresses the ionisation produced by X-rays in air is "exposure" in units called the *roentgen*. "Exposure" is fundamentally a property of the electron beam rather than a measurement of the effect of the beam on the object to be irradiated [3].

The basic quantity that characterizes the energy imparted to matter by ionising particles is the absorbed dose. The unit of absorbed dose is the *rad*. It is defined as the amount of energy imparted to matter per unit mass of irradiated material and is equal to 100 ergs per gram [3]. The output of high energy X-ray equipment is described in units of rads per minute at a distance of one meter.

4 .1.2 Quality of Radiation and Contrast of the Radiation Image

Suppose that for a given homogenous radiation, the half-value layer (HVL) is equal to d [2]. In figure 4.1 for the section of thickness a, the radiation will have to penetrate four HVL's, so that the radiation emerging will be $\left(\frac{1}{2}\times\frac{1}{2}\times\frac{1}{2}\times\frac{1}{2}\right)=\frac{1}{16}$ of the incident radiation. For thickness b, equal to two HVL's, the intensity of the emergent radiation will be $\left(\frac{1}{2}\times\frac{1}{2}\right)=\frac{1}{4}$ of the incident radiation. The contrast of two areas of the same image is the ratio $\frac{a}{b}$ of the radiation intensity corresponding to these two areas. The contrast of the two areas of the image is therefore $\left(\frac{\frac{1}{4}}{\frac{1}{16}}\right)=4$ which is a high contrast.

The HVL for a given material is greater for hard (high energy) radiation than for soft radiation. If a harder radiation with HVL equal to $2d$ is used, the intensity of the two areas of the radiation image will become, respectively, $\frac{1}{4}$ and $\frac{1}{2}$ of the incident radiation. The contrast of the two areas is now equal to 2 and it can be concluded that harder radiation will give a lower image contrast.

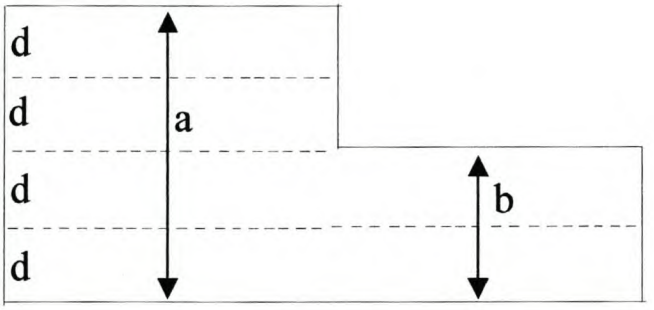

Figure 4.1: A schematic diagram of an image of an object of widely varying thickness [2].

4.1.3 Choice of X-ray source

Consider the solid cylinder with incident X-ray radiation following paths 'a' and 'b' as shown in figure 4.2. There are less HVL's for the X-rays to pass through for path 'b' than for the path 'a'. This will result in a high contrast between the edges (path 'b') and diameter (path 'a') of the cylinder.

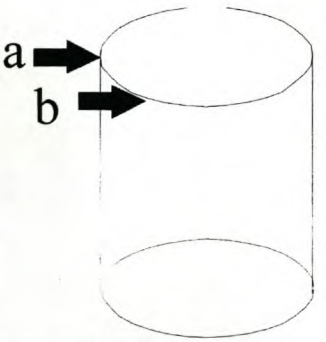

Figure 4.2: X-ray paths 'a' along diameter and 'b' at edge of solid cylinder.

Reducing the contrast is desirable when a radiograph image of an object of widely varying thickness has to be obtained [2]. A lower contrast will make this object more visible on the X-ray image. To reduce the contrast, harder radiation must be used to X-ray the object [4]. This principle is explained in 4.1.2.

The geometrical shape of a porcelain post insulator approximates that of a cylinder with widely varying thickness and therefore a high energy X-ray source is necessary.

High energy X-rays are produced by electron linear accelerators (Linacs), which operate at various energies between 1MeV and 30MeV. The electron beam produced by an electron gun is accelerated to a high energy, which results from the electrons "riding" a high frequency electromagnetic wave traveling in a straight line down an acceleration tube. A magnetron generates microwaves within the main wave- guide, which continuously supply energy to the electrons. These high energy electrons then strike a tungsten target and X-rays are released. The diameter of the cone of X-rays produced or the diameter of useful X-ray field gets smaller as the electron energy is raised which requires a large source-to-film distance, F, as seen in figure 4.3, in order to expose a large size radiograph.

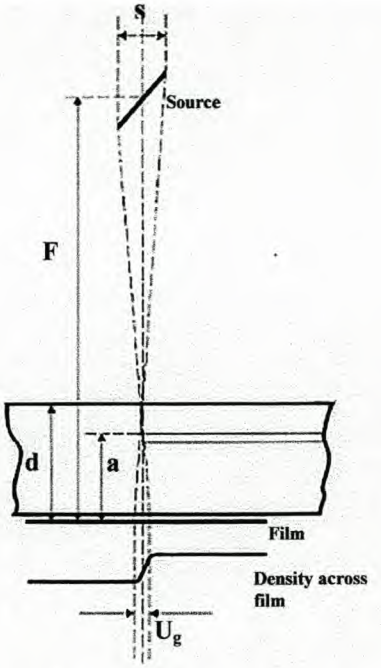

Figure 4.3: Geometric unsharpness (s is shown large for clarity) [2].

4.1.4 Intensifying Screens

The degree of photographic effect of the X-rays depends upon the amount of radiation energy absorbed by the sensitized coatings of the film [2]. This is of the order of 1% for radiation of medium penetrating power. The remaining radiation passes through the film and is consequently not used. To overcome this, the film is sandwiched between two intensifying lead screens. Under the action of X-rays these screens emit electrons and the result is an extra photographic effect upon the film emulsion layers. Close contact between the film and the screens is essential in order to obtain sharp images.

The lead screens are made from a thin sheet of lead foil. The front screen (on the object side of the film) must be matched to the hardness of the radiation being used, so that it will pass the primary radiation while stopping as much as possible of the secondary radiation (scattered radiation).

The overall effect of using lead intensifying screens is an improvement in the contrast of image detail, due to the reduction of scatter, and a decrease in the exposure time

when the intensifying effect is greater than the attenuation produced by the absorption in the front screen.

4.1.5 Choice of X-ray film and Processing

As already stated in 4.1.2 hard radiation gives a less contrasted radiograph, which means that defects will be less easy to discern. The reduction in contrast when using hard X-ray radiation must be partially compensated for if defects or voids within the insulator are to be seen on the radiograph. Hard radiation allows for shorter exposure times which makes it possible to use fine-grain X-ray films [2]. The Agfa-Gevaert Structurix D4 is a fine grain film, which is utilised to attain the film gradient necessary to improve the contrast of the radiograph.

The processing of the X-ray film after exposure to X-rays should be done using an automatic processor, as this will reduce processing times making radiograph results available sooner. It also standardises the processing, and consequently the exposure technique as well, and improves the quality and reliability of X-ray non-destructive testing [2].

4.1.6 Radiograph Viewing

The radiograph is placed on an illuminated screen (light box) of appropriate brightness for the film density. The film must be masked to avoid glare from around the edges or from low density areas.

The provision of good film viewing conditions is very important and it is possible to have information on a radiograph that is not seen because of poor viewing conditions.

The defect or void size inside the insulator can be determined by measuring its size on the radiograph and then by studying figure 4.3 the image size can be reduced using trigonometry to give an indication of the actual defect or void size.

4.1.7 Defect Discernibility

This section highlights some of the major issues that must be considered to ensure that defects and voids are visible on the radiograph and is taken from Halmslaw [2].

Three factors determine the visibility of defects in a radiograph:

1. Geometrical factors – dimensions of the source, source–to-object distance and defect-to-film distance.
2. The properties of the film – Graininess, contrast, fog, and inherent unsharpness.
3. The quality of the radiation – Soft or hard radiation.

4.1.7.1 Geometric Unsharpness, U_g

X-ray sources always produce radiographs with a certain amount of blurring which is termed the "geometric unsharpness" [2]. This is due to the finite dimensions of the target focal spot or X-ray source size.

The magnitude of unsharpness, U_g, from figure 4.3 is given by:

$U_g = \frac{s.a}{F-a}$, in which s is the effective diameter of the source of radiation,

F is the source–to-film distance (s.f.d.), and a is the defect-to-film distance.

The maximum value of U_g related to a defect situated at a maximum distance from the film (and for which a = d), can be calculated from the formula:

$U_g = \frac{s.d}{F-d} \cdots (4.1)$, where d is the thickness of the object.

From equation 4.1 it appears that, U_g can be reduced to any value by increasing the s.f.d. but this distance cannot be made unnecessarily large without avoiding an excessively long exposure time.

This formula also indicates that the geometric unsharpness assumes more and more importance as the distance between the defect and the film increases, and therefore every effort must be made in practice to keep this distance to a minimum. The object must be positioned to bring the defect as near as possible to the film.

4.1.7.2 Inherent (Film) Unsharpness, U_f

As X-rays penetrate a photographic emulsion, they liberate electrons [2]. These electrons fly off in all directions, and other silver halide crystals with which they come into contact may then become developable. The result is that when the exposed

film is developed, grains of silver form not only in the exposed portions but also (albeit to a lesser degree) in a volume of emulsion surrounding the exposed point. This cross-sectional area represents the "inherent unsharpness" or "film unsharpness", U_f, and its width is governed by the distance traveled by the electrons through the emulsion and consequently depends on the energy of the X-rays.

Even in the absence of geometric unsharpness, film unsharpness can be present if the radiation energy is high enough. Consider a sharp steel step as shown in figure 4.4 that is radiographed with high energy X-rays there will be a gradual transition of film density across the image of the "edge". Without any film unsharpness, the film would show an absolutely sharp transition between the two densities as shown in figure 4.4 (a). In practice the density change across the image is as shown in figures 4.4 (b), (c) and (d). The width of the transitional area, expressed in millimetres, is the measure of the film unsharpness.

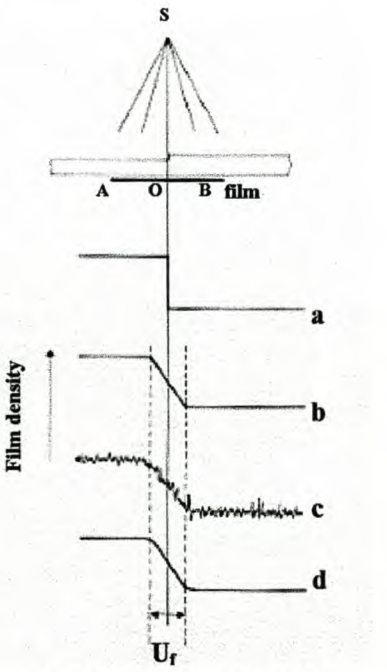

Figure 4.4: Film unsharpness [2]. The density curves are magnified along the X-axis for clarity. (a) density distribution across image of sharp edge, assuming U_f=0, (b), (c) and (d) density distribution due to film unsharpness. (a) theoretical; (c) with grain; (d) smoothed.

4.1.7.3 Total Unsharpness, U_T

In order to obtain the best possible practical defect sensitivity it is necessary to consider the total unsharpness on a radiograph. The combination of U_g and U_f is U_T and is given by $U_T = \sqrt{U_F^{\,2} + U_G^{\,2}}$ [3].

4.1.7.4 Choice of Source-to-film Distance (s.f.d.)

Total unsharpness must be kept to a minimum if maximum detail is to be visible on the radiograph. This is done by determining the value of U_f from figure 4.5 for the radiation to be used, and then making $U_g = U_f$ which enables the desirable F to be calculated using equation 4.2 below.

$F = \frac{t(U_T + s)}{U_T} \cdots (4.2)$, where t is the specimen thickness.

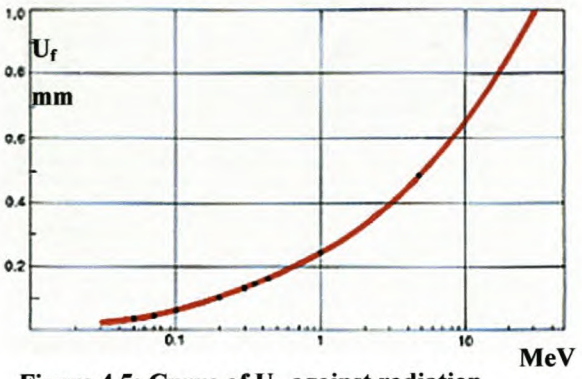

Figure 4.5: Curve of U_f against radiation energy, for typical radiographic film (experimental) [2].

4.1.7.5 The Inverse Square Law

The intensity of the radiation per unit area of film is inversely proportional to the square of the F .

Consider figure 4.6, at a distance of $2F$ from the source, the beam of rays will cover an area (b) which is 4 times greater than that at a distance F with area (a). Consequently the intensity per unit of surface area (b) will be cut by ¼ or $½^2$ of the value at (a).

If, therefore, the intensity per unit area is equal to I_1, at a distance F and equal to I_2 at a distance $2F$ the equation 4.3 below is true.

$$\frac{I_2}{I_1} = \frac{F^2}{(2F)^2} \cdots (4.3)$$

Alternatively the equation, $\frac{t_1}{(F_1)^2} = \frac{t_2}{(2F)^2}$ where t_1 and t_2 are the exposure times (or rads) can be used [3].

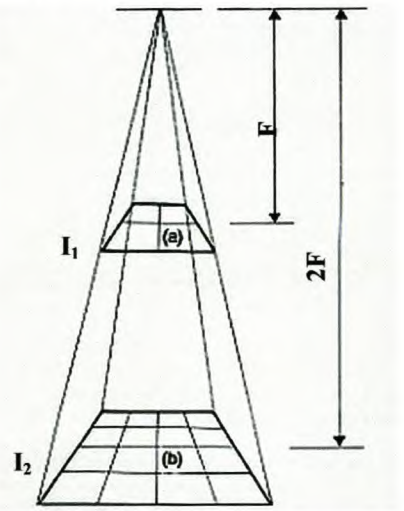

Figure 4.6: Inverse Square law [2].

4.1.7.6 Prevention of Image Distortion

On a radiograph, a three dimensional specimen is presented on a two dimensional plane (the film) and the appearance of both the specimen and any defects depends on the orientation of the beam of radiation. In figure 4.7 the image of a void may be circular or elongated according to the beam angle.

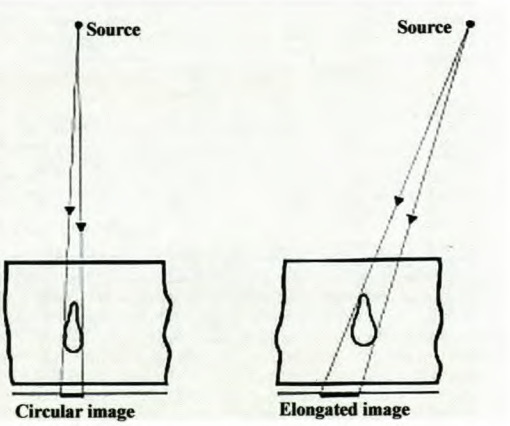

Figure 4.7: Distortion of image of elongated void due to radiation beam

In general the beam of radiation should be at right angles to the film.

4.2 Partial Discharge Detection

Partial discharge (PD) is a localized electrical discharge that only partially bridges the insulation between conductors and which may or may not occur adjacent to a conductor [13]. Although the magnitude of such discharges is usually small, they cause progressive deterioration and may lead to ultimate failure [5]. It is therefore essential to detect their presence in a non-destructive manner. There are three generally distinguishable types of partial discharges, namely internal (including discharges in electric trees), surface and corona discharges [6]. The partial discharge type encountered in porcelain post insulators is of the internal type. Internal discharges occur in inclusions of low dielectric strength such as gas filled voids [5]. If voids are present inside a porcelain post insulator they will be located entirely within a solid dielectric, or between a conductor and a solid dielectric, or at the interface of two solid dielectrics.

If PD activity is detected then voids are then present in the dielectric of the insulator.

4.2.1 Choice of PD Measurement Parameter

The deterioration of a dielectric is related to the charge transfer in the defect, but this charge cannot be measured with a discharge detector [5]. The discharges in a void cause current impulses in the leads attached to the test object. The displacement of charge q in the leads of the test object is given by $q = b\Delta V \cdots (4.4)$, where ΔV is the volt-drop across the void and b is the capacitance of the dielectric in series with the void as shown in figure 4.8.

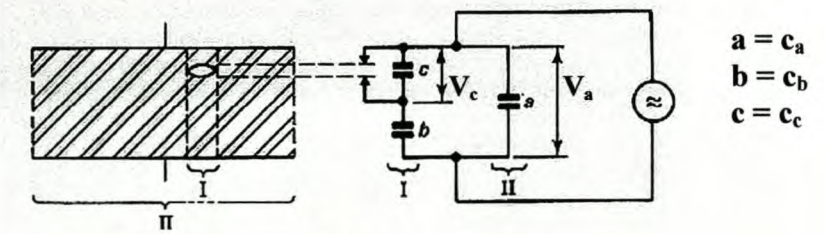

Figure 4.8: A dielectric circuit [5].

This causes a volt-drop $\frac{b\Delta V}{(a+b)}$ in the test object. Most discharge detectors respond to this volt-drop and are thus capable of determining q. Capacitance b in series with the void is not related to the void and q seems not to be a good choice. This apparent charge q that flows through the lead of the test object can be related to the energy p of the discharge as follows:

$$p = \frac{1}{2}c_c(U^2 - V^2)$$
$$= \frac{1}{2}c_c(U - V)(U + V)$$
$$= \frac{1}{2}c_c \times \Delta V \times (U + V) \cdots (4.5)$$

where c_c is the capacitance of the void as shown in figure 4.9(a), U is the breakdown voltage of the void and V is the voltage at which the discharge across the void extinguishes as depicted in figure 4.9(b).

If V is neglected, the answer becomes about 10% too low and equation 4.5 becomes:

$$p \cong \frac{1}{2}c_c \times \Delta V \times U \cdots (4.6) \text{ and}$$

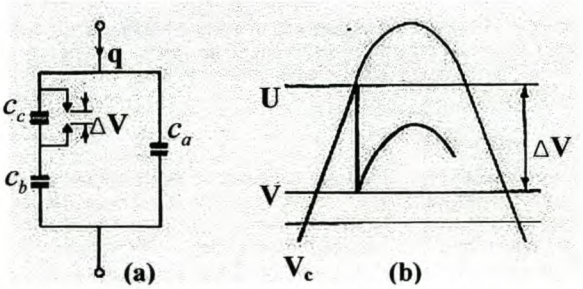

Figure 4.9: Relationship between the apparent charge and the energy p of the discharge [5].

$U = \frac{c_b}{c_b + c_c} \times \hat{V}_i \cdots (4.7)$, where $\hat{V}_i$ is the inception voltage at which the sample starts to discharge. Then substituting (4.7) into (4.6):

$$p \cong \frac{1}{2}c_c \times \Delta V \frac{c_b}{c_b + c_c} \times \hat{V}_i \cdots (4.8)$$

Neglect c_b as compared to c_c, so that the answer becomes several percent too high and the previous neglect is almost cancelled out. Then using equation 4.4, equation 4.8 becomes:

$$p \cong \frac{1}{2}c_b \times \Delta V \times \hat{V}_i$$
$$\cong \frac{1}{2} \times q \times \hat{V}_i \cdots (4.9)$$

The inception voltage usually is expressed in volts r.m.s. so that equation 4.9 becomes:

$$p \cong 0.7 \times q \times \hat{V}_i \cdots (4.10)$$

The discharge magnitude q is thus a reasonably good measure for the discharge energy p at the discharge site, which causes the deterioration of the dielectric.

The apparent charge q is not equal to the charge transfer in the void. The charge transfer in the void is usually several tens of times larger than the apparent charge q.

4.2.2 Discharge Inception and Extinction in Dielectric Voids.

This section highlights the relevant parameters to be considered with respect to the PD within an internal void and is summarised from Hall and Russek [8].

The discharge inception and extinction voltages depend upon the void depth or thickness in the direction of the applied electric field. The inception voltage increases with increasing void depth. The extinction voltage is usually lower than the inception voltage.

The discharge and extinction stresses depend upon the void depth or thickness in the direction of the applied electric field. The inception stress decreases with increasing void depth.

Void diameter (transverse to the applied field) has no effect on the inception level of voids of the same depth.

The thickness of the neighbouring dielectric has no effect on the inception level of a void.

The nature of the neighbouring dielectric has no significant effect on the inception level in an enclosed void.

Discharges in dielectric voids conform to Paschen's law.

4.2.3 Discharge Magnitude

The magnitude of the discharge in a void in picocoulombs (pC) is related to applied AC voltage and is a function of discharge type and void size as illustrated in figure 4.10 [6]. The discharge magnitude $q = c_b \Delta V$ can be related to the size of the discharge site as follows: $q \cong \varepsilon \times A \times \Delta V \times (\frac{1}{d})$ [5]. Thus the discharge magnitude q increases with the area A of the discharge site and with the ignition voltage ΔV, which in its turn increases with the thickness of the discharge site. Consequently the discharge magnitude increases with the volume of the void in the case of internal discharges.

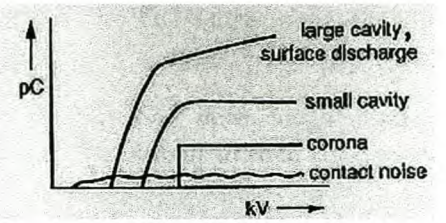

Figure 4.10: Discharge magnitude in pC versus applied voltage in kV as a function of discharge type or void size [6].

4.2.4 Selection of Test Circuit Configuration

An A.C. voltage source is necessary in a PD detector circuit in order to achieve pd activity as can be seen from figure 4.9(b).

The test circuit chosen must take into consideration the test requirements that are determined by the available test equipment, the uniqueness of the test sample and the design of the experiment. The PD detector test circuits considered were the standard circuit, the modified circuit and the balanced circuit.

The standard test circuit (figure 4.11) is constructed with great ease and allows the components of the assembled high voltage test circuit to be verified as being discharge free before the test sample is inserted into the circuit. This circuit suffers from the disadvantage that the stray capacitance of the test transformer must be added to the test samples capacitance. Stray capacitance can lead to errors if the test sample is small, but is negligible with a large test sample.

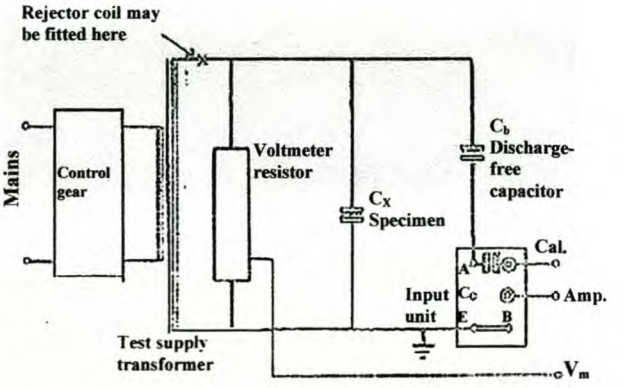

Figure 4.11: E.R.A. Standard PD detector circuit [9].

The modified test circuit (figure 4.12) is better than the standard circuit as the test transformer stray capacitance is added to the capacitance of the discharge free capacitor in the circuit leading to a more pessimistic result. The disadvantages of this circuit are that failure of the test specimen could destroy the input unit, the test sample must be isolated from earth, and the components of the assembled high voltage test circuit cannot easily be verified as being discharge free.

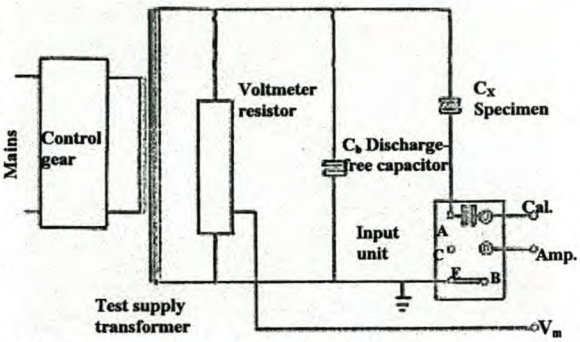

Figure 4.12: E.R.A. Modified PD detector circuit [9].

The balanced test circuit (figure 4.13) requires two nearly identical test samples. The advantages of this circuit include some reduction of the interference pick up and elimination of transformer stray capacitance effects. It is also possible to test to a much higher voltage than with the unbalanced circuits. The main disadvantage is the need to provide two test samples and if discharges are found the need to determine which sample is discharging.

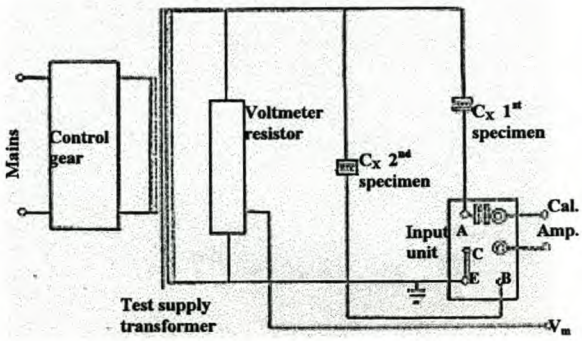

Figure 4.13: E.R.A. Balanced PD detector circuit [9].

The Standard test circuit is the more suitable circuit as it allows for easy verification over the test voltage range, of the condition of the available high voltage test circuit components by ensuring that unwanted discharges are not present before the test sample is inserted into the circuit. It is also suited to the design of the experiment to be conducted.

4.2.5 Recognition of Discharges

The Recognition of observed discharges is necessary to identify the nature, size and location of gas filled voids. This section deals with the recognition of discharges using discharge patterns, discharge magnitudes and X-Y diagrams.

4.2.5.1 Determination of discharge magnitudes

The accurate method of determining the magnitude of a discharge seen on the oscilloscope screen of the E.R.A. discharge detector control panel is to use the formula appropriate to the detector circuit chosen. The calibration step wave is matched to the amplitude of the displayed discharge pulse by adjusting the attenuator switches on the E.R.A. discharge detector control panel. The decibel values corresponding to each operated attenuator switch are added together to get a total decibel value. A value for E_q is then read from the table in appendix A.1 using the total decibel value. The value of q is determined using the appropriate detector circuit formula. The formula for the standard detector circuit is $Q_z = E_q C_q (1 + \frac{C_x}{C_b}) \cdots (4.11)$, where the test circuit load is $C_x + C_b$.

4.2.5.2 Discharge Patterns

Discharge patterns displayed on an oscilloscope screen give an indication of the type and origin of the discharges [5]. This can be seen by studying figures 4.14 (a), (b), (c) and (d).

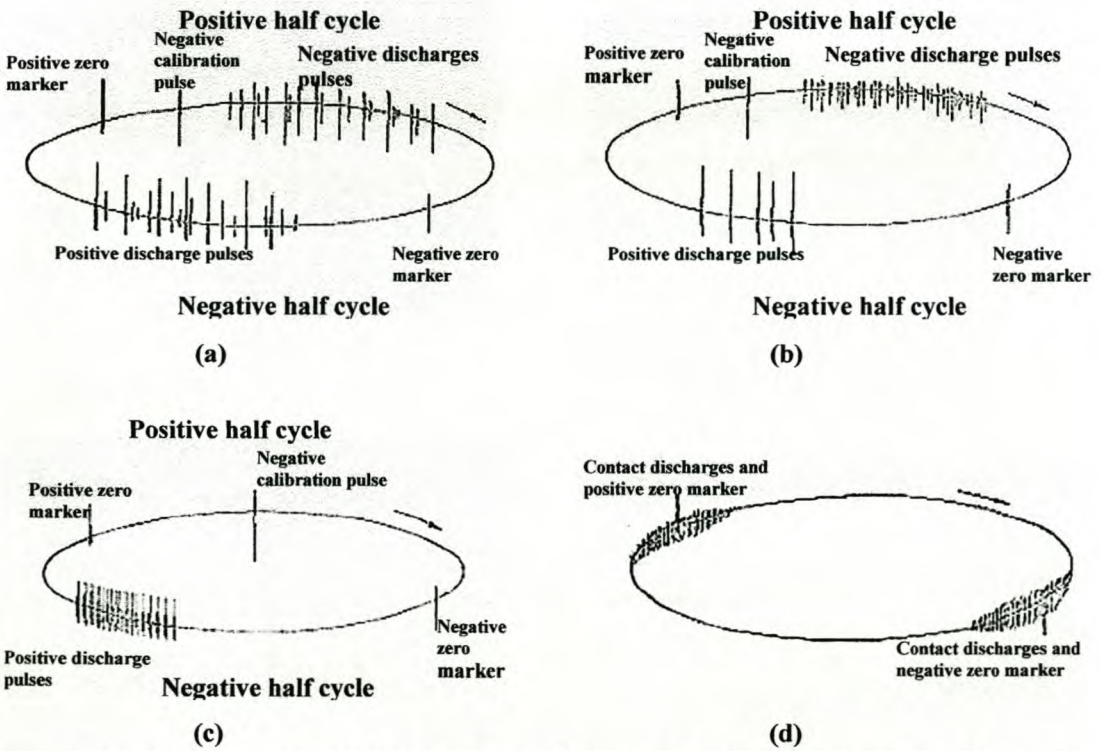

Figure 4.14: (a) Discharges in voids in insulation; (b) Discharges in voids bounded on one side by conductor and the other by dielectric; (c) Corona discharges; (d) Contact discharges in a capacitive circuit [9].

4.2.5.3 X-Y Diagram

The discharge magnitude is recorded as a function of voltage. The test voltage in kV is shown on a linear scale on the x-axis and the discharge magnitude in pC is shown on a logarithmic scale on the y-axis [5]. The X-Y diagram is made first for rising voltage and then declining voltage. A squarely shaped diagram shown in figure 4.15 indicates a discharge in a limited void depicted in figure 4.18. A triangular shaped diagram as shown in figure 4.16 indicates a discharge in a larger void depicted in figure 4.18, where the discharges can expand first and remain constant when the entire void has been filled with discharges. An ever increasing diagram as shown in figure 4.17 points to a surface discharge, or a discharge in a large gap or to discharges in an interface.

Analysis of both the oscilloscope evidence and the X-Y diagram will assist in determining the nature of the void or defect.

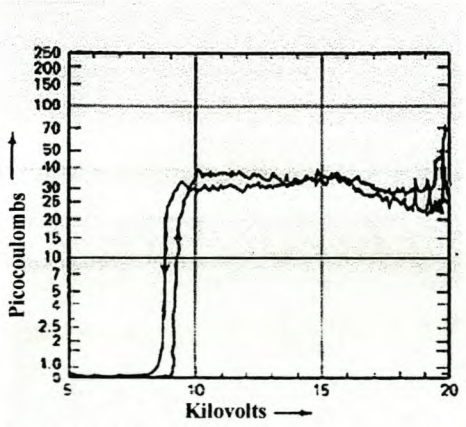

Figure 4.15: X-Y diagram of a void of limited dimensions, e.g. some square millimetres by 0,5 mm thickness [5].

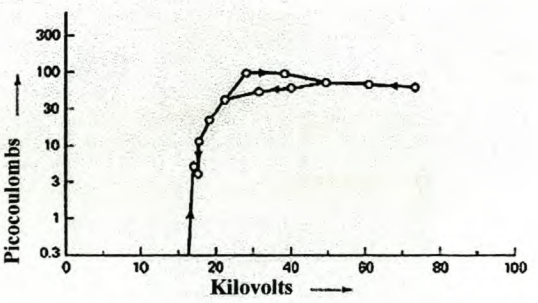

Figure 4.16: X-Y diagram of a discharge in a more extended void [5].

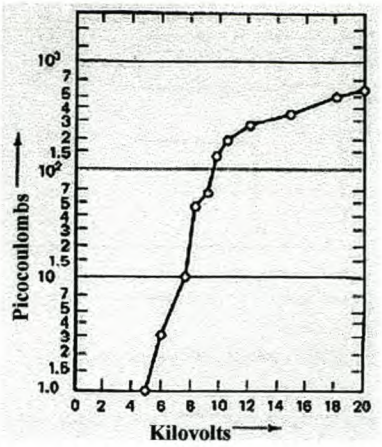

Figure 4.17: X-Y diagram of a surface discharge, discharges in a large gap or a long interface [5].

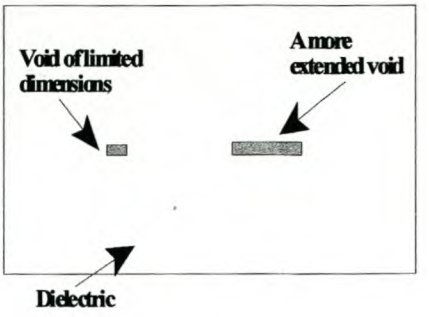

Figure 4.18: Dielectric bound voids yielding X-Y diagrams in figures 4.15 and 4.16 [5].

4.3 Ultrasonic Testing

Any medium whether solid, liquid or gas can be made to oscillate. If the oscillations occur so rapidly that they lie above human audibility limit they are referred to as being ultrasonic and have a frequency above 20 000Hz. The energy contained in ultrasound is transmitted through a medium by atomic or molecular bond forces or by mass attraction [11].

The testing of specimens for internal defect can be done by checking for a changed ringing tone after the work piece has been struck or tapped. This practice is one of the oldest non-destructive methods for detecting internal defects. The transition from audible sound to ultrasonic sound has been made possible by modern methods of generation and detection, which replace the hammer and ear.

When detecting the presence of flaws using ultrasound, the sound wave, which is the carrier of information, is transmitted into the specimen. The returning wave is captured using a receiver so that analysis of the information it carries can be conducted. The ultrasonic transmitter and receiver probes are piezo-electric (or magnetostrictive) devices. The sound pressure of an impinging wave is directly proportional to the electrical potential from the piezo-electric plate and vice versa.

In a longitudinal wave the oscillation and propagation have the same direction [11]. The propagation velocity of a longitudinal wave in a solid material is given by:

$c_l = \sqrt{\frac{E}{\rho}}\sqrt{\frac{1-\mu}{(1+\mu)(1-2\mu)}} \cdots (4.12)$, where E is the elasticity module, ρ is the material density and μ is the Poisson constant.

In a shear wave the oscillation direction is perpendicular to the propagation direction [11]. The propagation velocity of a shear wave in a solid material is given by:

$$c_s = \sqrt{\frac{E}{\rho}}\sqrt{\frac{1-\mu}{(1+\mu)(1-2\mu)}} \cdots (4.13)$$

4.3.1 Reflection and Transmission

When a sound wave is moving towards an obstacle and strikes it perpendicular to its surface, some sound pressure is reflected and some is transmitted.

The acoustic impedance, Z, of a material is specific to a material and given by the equation [10] :

$Z = \rho c \cdots (4.14)$.

Z depends on the elastic properties of the insonified material and has a high value for solids and a lower value for liquids. Z_1 and Z_2 are the acoustic impedances as shown in figure 4.19.

The reflection and transmission coefficients are given by equations 4.15 and 4.16 respectively [12]:

$$r = \frac{Z_2 - Z_1}{Z_1 + Z_2} \cdots (4.15)$$

$$\tau = \frac{2Z_2}{Z_1 + Z_2} \cdots (4.16)$$

These coefficients can be expressed as percentages of the sound pressure of the incident wave.

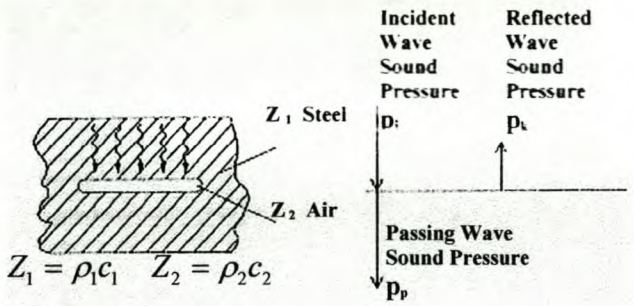

Figure 4.19: Wave reflection at an interface [11].

Examination of equation 4.16 reveals that the transmission coefficient, τ, is small if Z_1 is large. Examination of equation 4.15 reveals that if Z_2 is small, r is large indicating that most on the incident wave will be reflected. This demonstrates that if

the wave were to strike an internal void filled with air, the air that has a low Z (see Appendix B.1) will result in r approaching unity (total reflection of the incident wave) and τ approaching zero (no transmission into the void).

4.3.2 Refraction (Snell's Law)

The impinging wave may not necessarily be perpendicular to a surface where two acoustical media are joined. In the case of oblique incidence a refraction occurs at the interface as shown in figure 4.20.

Incident, reflected and refracted angles can be evaluated by Snell's law in equation 4.17.

$\frac{Sin\alpha_1}{Sin\gamma_1} = \frac{c_{l_1}}{c_{l_2}} \cdots (4.17)$, where α_1 is the incident angle, γ_1 is the refracted angle, and c_{l_1} and c_{l_2} are the longitudinal sound velocities of the incident and refracted longitudinal waves respectively [11].

Equation 4.17 is valid for all kinds of waves and the appropriate velocities must be fitted into the equation.

Figure 4.20 shows all kinds of resulting sound waves.

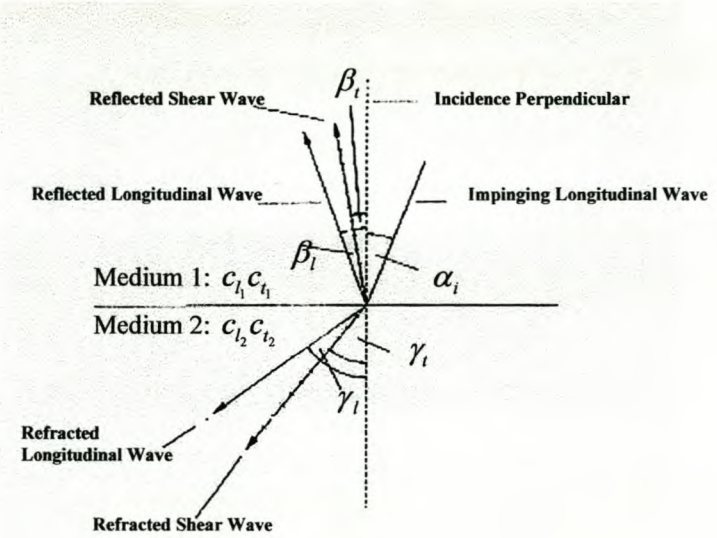

Figure 4.20: Refraction of a Longitudinal wave [11].

4.3.3 Boundaries

There are three cases where boundaries have a strong influence on the propagation of sound, when testing materials [10]:

- The wave has to penetrate boundaries when passing from a generator into a specimen and vice versa.
- Defects within specimens are detected by the effect of their boundaries on the wave (reflection and transmission).
- Other boundaries of the specimen may influence the propagation by interfering reflections or by the intentional guiding (eg. plates or rods) or by reflecting the wave into areas otherwise not accessible.

4.3.4 Pulse-Echo Method of Flaw Detection

Ideally an ultrasonic pulsed wave is generated by a piezo-electric probe and propagates into a specimen with the velocity corresponding to the material the pulsed wave is traveling through [10]. Part of the ultrasound will be reflected if it strikes a flaw in the form of an inhomogeneity and, if this is not too large, the remainder will travel further to a boundary of the specimen and will be reflected back to the receiver. The signal obtained from the receiver is displayed on an oscilloscope. This basic principle of pulse-echo is illustrated in figure 4.21. The horizontal sweep of the oscilloscope is proportional to the time, so that the transit times of the pulse to and from the flaw, and to and from the back wall, correspond respectively to the distances on the screen from the initial peak to the echo peaks corresponding to the flaw and back wall. By calibrating the base line of the oscilloscope in time per unit length the transit times can be read from the screen and the distance, d, of any flaw can be calculated using equation 4.18 if the velocity of sound in the material is known.

$$c = \frac{2d}{t} \cdots (4.18) \text{ or } d = \frac{ct}{2}$$

The signal intensity or echo height is proportional to the traveled distance; the height of the back wall echo decreases the more the back wall is shadowed by the flaw and an important influence that might lead to misinterpretations is the multiple reflection between the front wall and the obstacle [11]. These phenomena are illustrated in figure 4.22.

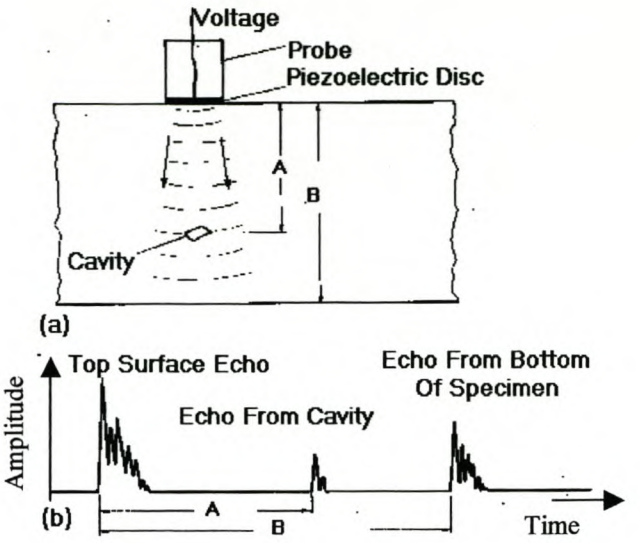

Figure 4.21: Basic principle of ultrasonic testing with a compressional probe, (a) set-up (b) standard A-scan display.

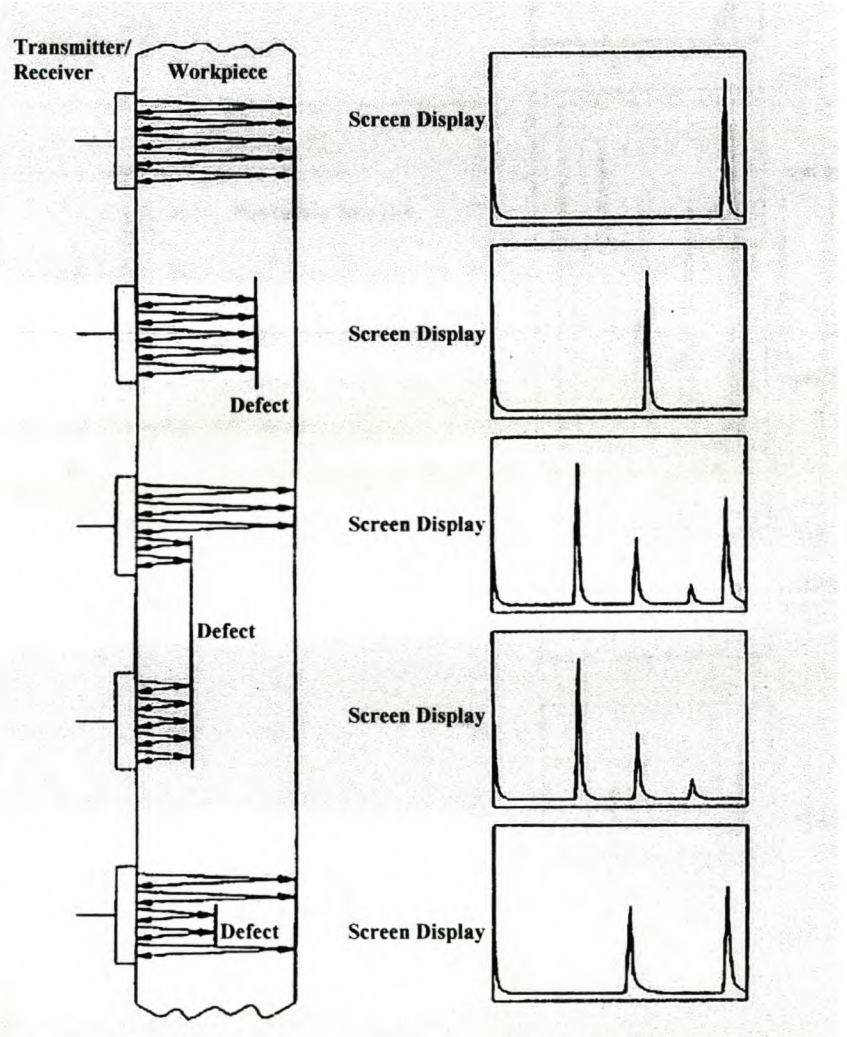

Figure 4.22: Pulse-Echo Method illustrated with the corresponding oscilloscope display [11].

Conclusion

In the previous sections three NDT techniques were reviewed and the following concluding remarks are made:

Industrial Radiography

- A high energy X-ray source is necessary for X-raying porcelain post insulators in order to overcome the high contrast between the thin edges and thicker body sections of the insulator body.
- The loss of contrast that results from using hard radiation can be partially compensated for to allow flaws within the insulator to be seen on the radiograph if a film with a fine grain like Agfa-Gevaert Structurix D4 is used.
- Good viewing conditions are necessary for all the information on the radiograph to be seen.
- Good defect discernibility is governed by the quality of radiation, the properties of the film, dimensions of the source, the source-to-object distance and the defect-to-film distance.

Partial Discharge Detection

- The ability to detect the presence of PD is an indication of the presence of voids inside the porcelain post insulator.
- The inception level of a void is dependant on the depth of the void in the direction of the applied electric field and is independent of the diameter of the void or the nature, or thickness of the neighbouring dielectric.
- The standard PD detector circuit is preferred due to the condition of the high voltage components available and the design of the experiment to be conducted.
- Analysis of both the oscilloscope evidence and the X-Y diagram should assist in determining the nature of a void or defect inside the insulator.

Ultrasonic Testing

- The acoustic impedances of the coupling gel and specimen must be matched as best possible to ensure good transmission of the generated wave.
- Ensure that the transmitter and receiver are perpendicular to the surface of the specimen in order to avoid refraction of the incident wave.
- Voids present inside a specimen will reflect the impinging wave.
- The Pulse-Echo method can detect the presence of a flaw and the distance of the flaw from the front wall.

References

1. Halmslaw,R, "The Early History of X-rays, Gamma-rays and Industrial Radiography", 14th World Conference on Non-Destructive Testing, New Delhi, 8 – 13 December 1996, Vol. 1, pages27 – 34.
2. Halmslaw,R, "Industrial Radiography- Agfa NDT" ,Agfa-Gevaert N.V. , 1991.
3. Heffan,H and Brunty,B.J, "Linatron – High Energy X-ray Applications for Non-Destructive Testing" Diablo Test Associates for Varian Associates, Inc., 1982.
4. Annual Book of ASTM Standards Section 3 "Metals Test Methods and Analytical Procedures", Vol. 03.03 Non-destructive testing 1987.
5. Kreuger,F.H., "Partial Discharge Detection in High Voltage Equipment", Butterworths, 1989.
6. Kreuger,F.H., "Industrial High Voltage", Delft University Press, Volume 2, 1992.
7. Gallagher,T.J. et al., "High Voltage Measurement, Testing and Design", John Wiley & Sons, 1983.
8. Hall,H.C. et al., "Discharge Inception and Extinction in Dielectric Voids", IEE Transactions Measurements Section Paper no. 1618,Vol. 101, part II, 1954.
9. Robinson Electronic Instruments, "E.R.A. Discharge Detector Model 3 System Manual".
10. Krautkramer,J et al., "Ultrasonic Testing of Materials", Springer-Verlag, 1990.

11. Stegemann,D, "Ultrasonic Techniques", NDT Summer School, Pretoria University, Engineering, 1991.
12. Ristic,V, "Principles of Acoustic Devices", John Wiley & Sons, 1983.
13. International Electrotechnical Commission (IEC) Standard 60270, "Partial Discharge Measurements", third edition, 1999.

Design and Set-up of NDT Experiments

In this chapter the three NDT techniques introduced in chapter 4 are used in experiments to determine their ability to detect voids in the nine sample porcelain line post insulators. The manufacturer initially donated six porcelain line post insulators for test purposes. The sample insulators were labelled by the manufacturer and consisted of:

3×33kV 4kN (1120mm creepage) insulators labelled 2, 3 and 4, and

3×22kV 4kN (620 mm creepage) insulators labelled A, B and C.

All six of these insulators were specifically made for this study. No indication was given of whether internal voids would be present or not.

Three further samples were later obtained from the manufacturer as control samples and were said to be free of internal voids. These three control samples consisted of:

1×22kV 4kN (620mm creepage) insulator labelled CX,

1×33kV 4kN (900mm creepage) insulator labelled CX1, and

1×33kV 4kN (1120mm creepage) insulator labelled CX2.

The three types of sample porcelain line post insulators are shown in figure 5.1.

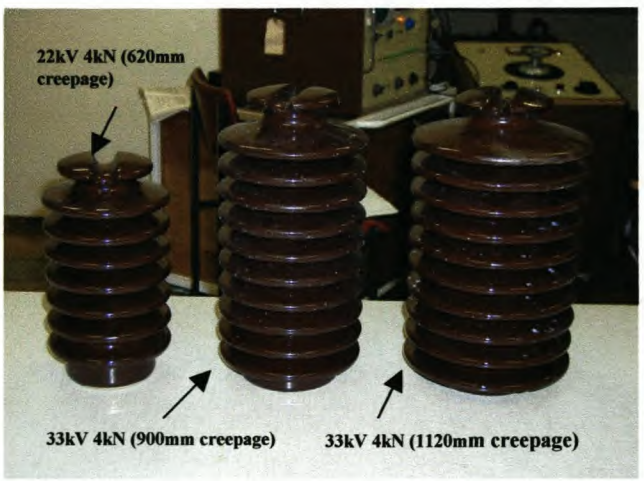

Figure 5.1: Three types of capless porcelain line post insulator samples donated by the manufacturer.

5.1 X-ray Detection

Industrial radiography has evolved mainly around the inspection of metals and therefore no information is available on the X-raying of porcelain insulators. Although theoretical calculations are useful in the initial setting up of equipment it is ultimately the radiographer's practical experience that will ensure a high quality X-ray image.

In chapter 2 the need for a high energy X-ray source was explained. Figure 5.2 shows a typical high energy X-ray source. Denel's Somchem Division has the only high energy X-ray facility in Southern Africa. The Somchem X-ray machine used in this experiment was a 2MeV Linatron model 200A with a maximum focal spot diameter of 2mm.

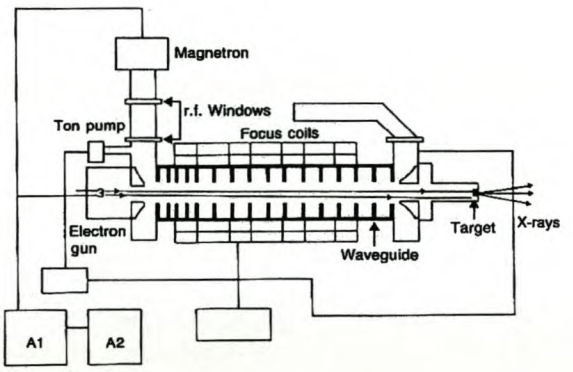

Figure 5.2: Linear electron accelerator [5].

5.1.1 Experimental Set-up

The insulator flaws occur in the main body of the insulator, particularly in the vicinity of the metal insert. For this reason a defect-to-film distance, d, as indicated in figure 5.3 is used. The values of d in table 5.1 were determined by examination of the manufacturer's drawings and were then verified by physical measurement of the sample insulators.

A large source-to-film distance, F, of 4m was chosen to reduce the geometric unsharpness. Using figure 4.5, for a 2MeV source, U_F is approximately 0.3mm.

Equation 4.1 is used to calculate U_G and the total unsharpness is then determined using the equation, $U_T = \sqrt{U_F^{\,2} + U_G^{\,2}}$ [4]. The total unsharpness of the X-ray images for each of the three sample insulator types are tabulated in table 5.1. These values are only an indication, but the visibility of the defects on the actual X-ray images will decide whether the X-rays are acceptable or not. Somchem regards, defect size expressed as a percentage of the specimen thickness, as an acceptable measure of defect visibility. Two percent is considered to be a good defect visibility.

The Agfa-Gevaert Structurix D4 fine grain film (D4P 35×43mm) was used and sandwiched between two lead foil intensifying screens each 0.2mm thick as shown in figure 5.3.

The X-ray beam and insulator sample are lined up using a laser beam. This will prevent image distortion by ensuring a right angle between the X-ray beam and the insulator.

The X-ray source was adjusted to deliver 150rads/min at 1 metre. The 33kV insulators of larger mass were exposed to this radiation for 2 minutes while the smaller 22kV insulators were exposed for 1.6 minutes.

Table 5.1: Expected total unsharpness values for the X-ray images of the three types of insulator samples.

Insulator sample type	Defect-to-film distance, d	Film unsharpness, U_F	Geometric unsharpness, U_G	Total unsharpness, U_T
22kV (620mm creepage)	135mm	0.3mm	0.069mm	0.308mm
33kV (1120mm creepage)	160mm	0.3mm	0.0833mm	0.311mm
33kV (900mm creepage)	147mm	0.3mm	0.0763mm	0.31mm

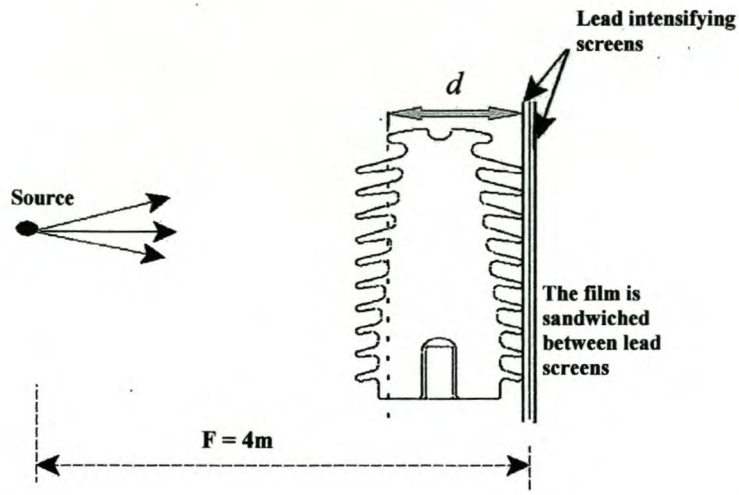

Figure 5.3: Schematic diagram of the X-ray set-up indicating the defect-to-film distance measurement.

5.2 Partial Discharge Detection

Specimens to be PD tested must have at least two electrodes (high voltage and earth) for it to be inserted in a PD test circuit. Figure 5.1 is representative of the donated samples and as can be seen from figure 2.6 they only have one electrode at their base, which is the mechanical attachment (metal insert) to the overhead power line structure. To perform a PD test on these insulators will therefore require a specially designed experiment to provide a second electrode.

It was decided to use a conducting liquid as the second electrode as this would conform to the complex shape of the insulator and also provide a means of adjusting the spacing between the high voltage and earthed electrodes. The ability to adjust the electrode spacing allows the electric field strength to be varied in the base portion of the insulator. Increasing the electric field stress in this region of the insulator will promote discharges inside the voids in the sulphur cement and increase the PD magnitude making detection easier.

Tap water was considered as a possible liquid electrode, but in order to prevent any additional capacitance being introduced into the circuit it was decided to use a saturated saltwater solution. Additional capacitance in the circuit would require a

higher test voltage (potential divider) and there also exists the possibility of introducing unwanted PD activity.

The advantages of using the saltwater solution are that it is cheap to produce and easy to work with.

The conductivity, σ, of the saltwater solution was measured and found to be 49.6 mS/cm. The resistance of the saltwater solution is, $R_{solution} = \frac{l}{\sigma A}$, where l is the length and A is the cross-sectional area of the volume occupied by the saltwater solution. The glass tank shown in figure 5.4 is the test vessel and its inner dimensions are: depth = 415mm and length = breadth = 400mm. If the displaced volume of the inverted insulator in the solution is ignored and the full volume of the tank utilised, then:

$$A = l \times b = 400 \times 400 = 160000mm^2 = 0.16m^2$$

$$R_{solution} = \frac{l}{\sigma A} = \frac{0.415}{49.6 \times 10^{-1} \times 0.16} = 0.5229\Omega$$

The saltwater solution is therefore a conductor and is suitable as an electrode as almost the full test voltage will be impressed on the inverted insulator.

5.2.1 Test Specimen Preparation

As can be seen in figure 5.4 (a), the insulator is inverted and supported on a mild steel collar inside the glass tank. The saltwater solution is carefully decanted into the tank making certain not to cause unwanted splashing onto the upper two sheds of the inverted insulator. The tank should be filled with solution so that its level is just beneath the second shed. The reason for this specific level of solution in the tank will be explained in section 5.2.4. A M20 bolt is threaded into the metal insert at the insulator base and a 20mm inner diameter (ID) copper pipe fitted over it (see figures 5.6 and 5.7) for coupling to the PD test circuit.

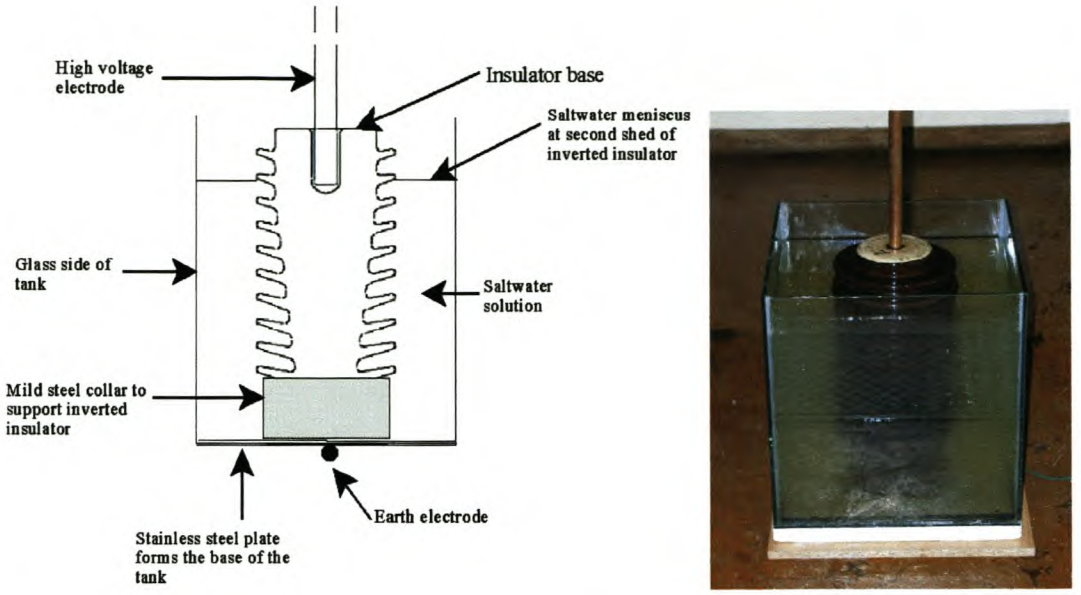

Figure 5.4: Insulator inverted in a glass tank filled with a saturated saltwater solution so that only two sheds are exposed above the surface of the solution. (a) schematic diagram and (b) photograph.

5.2.2 Components of the Detection Circuit

The PD detector used was the E.R.A. Discharge Detector Model 3. In chapter 4 the standard PD detection circuit shown in figure 4.11 was selected.

C_x is the inverted insulator sample placed in the glass tank with two sheds exposed above the saltwater solution as seen in figure 5.4. The saltwater solution is earthed via the tank's stainless steel base plate and the metal insert in the insulator base is attached to the high voltage side of the circuit.

The coupling capacitor, C_b is a 1000pF discharge-free capacitor obtained from the laboratory high voltage construction kit.

There are two considerations to be made in the selection of the Input Unit. The first consideration is that the tuning capacitance of the circuit must match the capacitance of the Input Unit. The tuning capacitance is the total external capacitance of figure 4.11 and is measured between terminals A and B on the detection circuit and is the

series combination of the specimen and the coupling capacitor. The tuning capacitance should fall in the middle of the Input Unit's range for best sensitivity.

Circuit tuning capacitance $= \frac{1}{\frac{1}{C_x} + \frac{1}{C_b}} = 12.83pF$, if $C_x = 13pF$. The E.R.A. Discharge Detector Model 3 operation manual (see appendix A.2) suggests using the Input Unit no. 1 with $C_q = 2pF$.

The second consideration is that the Input Unit must be capable of carrying the maximum current that will flow through its windings when the test is in progress. This current is determined by $I_{\max} = \frac{V_{test}}{X_{C_b}} = \frac{30kV}{\frac{1}{\omega C_b}} = 9.4mA$. V_{test} is the upper limit of the test voltage and is determined in section 5.2.5. Input Unit 1 is capable of carrying a maximum rms current 30mA, which is acceptable. An E.R.A. Input Unit can be seen figure 5.5.

The test voltage was supplied by a 220V/100kV, 7.5kVA single phase Ferranti transformer operating off the 220V, 50Hz mains supply. This test transformer had tapping ranges of 220V/50kV and 220V/100kV, the former being the suitable range for the test requirements.

Figure 5.5: Typical E.R.A. Input Unit used in the detection circuit.

The standard PD detection circuit is constructed using a "Messwandler Bau" high voltage construction kit as shown in figures 5.6 and 5.7. Input Unit 2 was installed in the circuit as determined in section 5.2.3. The equipment is placed in a Faraday cage to prevent picking up interference from outside the test circuit, such as radio transmitters and electronic switching [2]. Single point earthing was employed as it reduces interference by providing a low impedance earth connection and avoids the possibility of earth loops [1]. As can be seen from figure 5.6, all components of the circuit are properly earthed either via the copper clad table or earthing leads to prevent disturbances caused by badly earthed components or small floating objects.

5.2.3 Test Procedure

Once the circuit was constructed, the test insulator, C_x, was disconnected from the detector circuit. The circuit was then energised and the PD detector monitored to ensure that no interference was present. The voltage was then increased to determine whether contact noise or unwanted discharges such as corona from the high voltage rail or equipment discharges were present in the circuit. At approximately 35kV partial discharges associated with the equipment were noticed on the detector display. It was then decided to limit the test voltage to 30kV.

The test insulator was then re-connected into the circuit. The circuit was then re-energised and the voltage slowly increased. When discharges started appearing it soon became evident that the magnitude of the discharges detected were too large to measure with the calibration pulse. This is an indication that the sensitivity was too high. Various combinations of saltwater solution levels and Input Units were experimented with and the combination that gave good sensitivity with measurable discharge magnitude was found to be Input Unit 4 with a solution level adjusted to just below the second shed of the inverted insulator. Input Unit 4 is shown in figure 5.5.

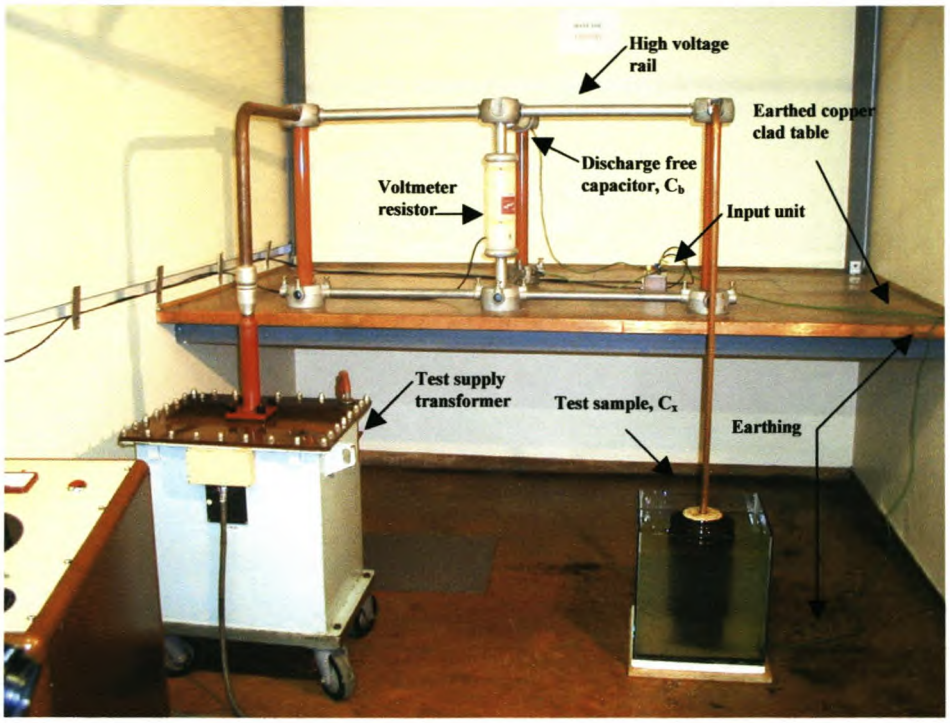

Figure 5.6: Standard PD Detection circuit with high voltage components and earthing visible.

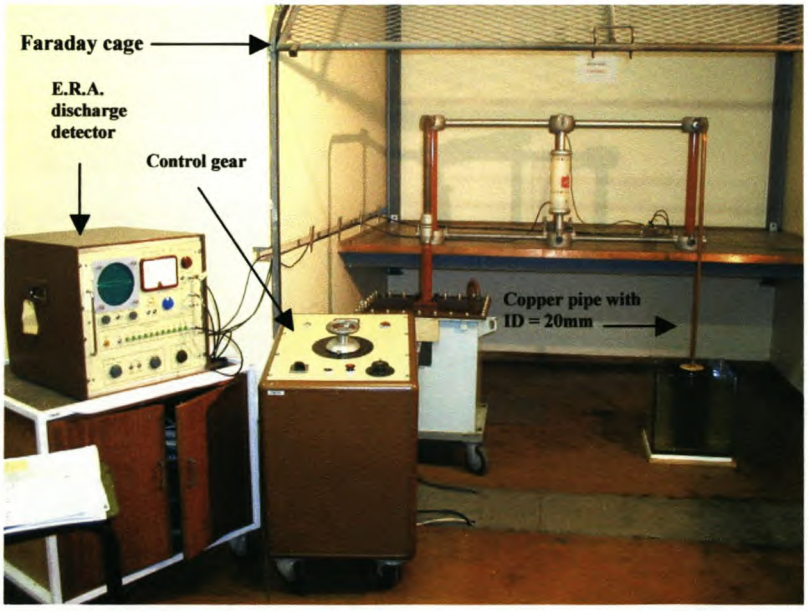

Figure 5.7: Standard PD Detection circuit with E.R.A. Discharge Detector Model 3 and Control Gear clearly visible in the foreground.

The full operating instructions for the E.R.A. Discharge Detector Model 3 can be found in appendix A.3. This section gives the method followed to determine the discharge magnitudes for each sample insulator over the test voltage range for the purpose of plotting X-Y diagrams. The test voltage range chosen was 0 to 30 kV.

Starting at 0V and making increments of 1 kV, the PD detector was monitored and the PD inception voltage and attenuation value recorded. The attenuation values were then recorded for each 1kV increment up to the 30kV upper limit. The test voltage was then lowered in 1 kV decrements, once again recording the attenuation values. Finally, the PD extinction voltage and attenuation value were recorded. This process was repeated for each insulator sample.

During the testing of the insulator samples a Corocam mark 1 manufactured by the CSIR, which is sensitive to ultraviolet light, was used to monitor the test apparatus for external discharges. Surface discharges appeared across the surface of the insulator bases in the vicinity of the high voltage electrode seen in figure 5.4 (a). The voltage at which these surface discharges were visible with the Corocam differed from insulator to insulator, but fell within the range 13 to 17 kV. In figure 5.8 (a) the surface discharges on the base of insulator sample 2 can be seen and these appeared at 13.5kV. In order to discover the exact location of these discharges the voltage was increased to 42kV and the image in figure 5.8 (b) appeared. This image displayed a circular pattern at the interface of the M20 bolt to the sulphur cement and a single discharge at the sulphur cement to porcelain interface. An examination of each insulator base revealed that the sulphur cement portion of the insulator base had a rough surface with depressions. The unwanted surface discharges were eliminated by displacing the air in the depressions in the sulphur cement with sunflower (vegetable) oil. This oil has a permittivity, $\varepsilon_r = 3.2$ and a dielectric strength of 160kV/cm [3].

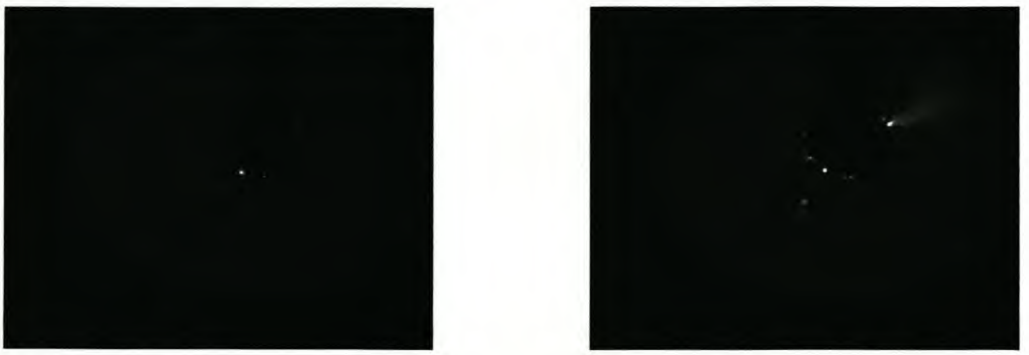

(a) (b)

Figure 5.8: Surface discharges on the base of insulator 2 during PD detection. (a) at 13.5kV and (b) at 42kV.

Equation 4.11 requires the value of C_x in order to compute the value of the discharge magnitude. By examination of equation 4.11 it is evident that C_x plays a negligible role in the outcome of this equation, since C_b is so large. Nevertheless, the capacitance of each insulator sample was measured for the test set-up shown in figure 5.4 (b) using an AVO-Delta 2000 10kV Automated Insulation Test Set and the values tabulated in table 5.2.

Table 5.2: C_x values for each sample insulator inverted in a saltwater solution so that only the upper two sheds are exposed.

Insulator Sample:	A	B	C	CX	2	3	4	CX2	CX1
Capacitance in pF:	13.68	13.49	13.56	13.28	14.68	16.29	12.99	13.03	12.17

5.3 Ultrasonic Testing

Ultrasound can propagate in many materials and is unproblematic to use. For this reason ultrasonic testing is used to verify that the properties materials are claimed to have comply with those that they really do have.

This section will describe the experimental approach to the use of the ultrasonic Pulse-Echo test and Change of Flight methods for the identification of internal flaws in the sample insulators. A first order study is undertaken to determine if this is a viable NDT method for the identification of insulator internal flaws and if there is merit for further research.

5.3.1 Pulse-Echo method

Two commercially available piezoelectric 40kHz ultrasonic burglar alarm transducers were purchased and carefully dismantled (see figure 5.8). The cone on the front of each of the two transducers was removed and the transducers were than super-glued onto a specially machined face at the end of the M20 bolt as shown in figure 5.9 (b). This now provides for separate transducers for signal transmitting and receiving. The new resonant frequency of the transducers for the new arrangement were now determined using an Agilent 33120A 15MHz function/arbitrary waveform generator

and an Agilent 54622A 100MHz oscilloscope. The resonant frequency was found to be 400kHz.

Since the M20 bolt is to be threaded into the mild steel insert in the insulator base a coupling agent was necessary to ensure that the injected pulse will propagate into the insulator. Glycerine was chosen as the coupling agent between the M20 bolt and the metal insert as it was cheap, freely available and had the highest acoustic impedance of all the coupling fluids found in appendix B.1. Other material interfaces to be considered are between the sulphur cement and mild steel insert and the sulphur cement and porcelain. Equations 4.15 and 4.16 must be utilised in conjunction with the acoustic impedances given in appendix B.1 to determine the degrees of reflection and transmission of the incident pulse at each interface within the insulator.

From appendix B.1 the acoustic impedances of the M20 steel bolt and glycerine are $46.6\times10^6\frac{kg}{m^2.s}$ and $2.5\times10^6\frac{kg}{m^2.s}$ respectively. Using equations 4.15 and 4.16:

$r=\frac{Z_2-Z_1}{Z_1+Z_2}=\frac{2.5-46.6}{46.6+2.5}=-0.898$ and $\tau=\frac{2Z_2}{Z_1+Z_2}=\frac{2\times2.5}{46.6+2.5}=0.102$. So, theoretically, approximately 90% of the wave entering the M20 steel bolt will not propagate into the insulator but will be reflected from the end of the bolt. This is detrimental to the success of the Pulse-Echo method. There are further material interfaces inside the insulator and the total reflected and transmitted percentages of the incident wave will vary with the acoustic impedances of the insulator component materials.

A useful preliminary experiment was to performing the Pulse-Echo method on the bolt with transmitter and receiver in air (free of the insulator) as this will help with later comparative analysis.

The M20 bolt with the transducers attached was then threaded into the base of the inverted insulator using glycerine. The wave generator and a channel of the oscilloscope were wired to the transmitting transducer. This provides a trigger for the oscilloscope and a wave for transmission into the insulator. The other channel of the oscilloscope was wired to the receiving transducer. The test set-up can be seen in figure 5.9 (a)

A 10-cycle burst (pulse) of 400kHz; 10Vpeak sine wave was injected into the transmitter transducer. The receiver transducer was then monitored on the oscilloscope.

The longitudinal speed of sound in the mild steel M20 bolt is 5950m/s from appendix B.1 and the bolt length was measured and found to be 257mm. The return pulse from the end of the M20 steel bolt is calculated using equation 4.18 and is $t = \frac{2d}{s} = \frac{2 \times 0.257}{5950} = 86.3\mu s$. Thereafter all other returning pulses are from flaws, the insulator walls, internal components, material interfaces and multiple reflections. These are then analysed to determine the presence and location of flaws.

Figure 5.9: Dismantled 40kHz ultrasonic burglar alarm transducer.

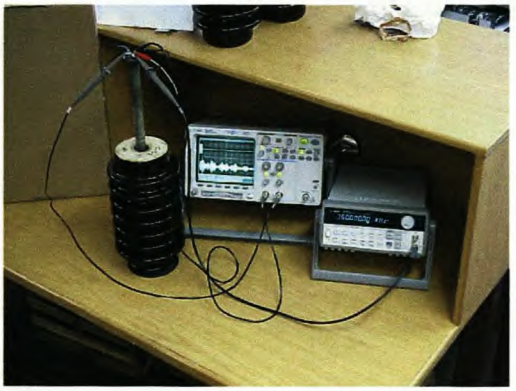

(a)

(b)

Figure 5.10: (a) Pulse-echo experiment with transmitter and receiver mounted on M20 (20mm) bolt which is threaded into the insulator metal insert, and (b) view of the transmitter and receiver on the M20 bolt with oscilloscope and function generator leads attached.

5.3.2 Change of Flight Method

The Change of Flight method was also assessed, which looks at the propagation of the pulse through the insulator. The insulator is made up of a complex shape and combination of mediums including voids, which would effect not only the time of flight (propagation rate) but also the propagation path (voids cause scattering) and frequency response. The pulse received would show changes in amplitude and phase and these characteristics could then be related to the insulator materials.

Two lead electrodes were specially cast to fit the contour of the 22kV 4kN (620mm creepage) sample insulator between the lower two sheds as seen in figure 5.10 (b). The transducers were super-glued to the lead electrodes and two screws fitted to each electrode. The screws were used to clamp the electrodes to the insulator using strong elastic rubber bands with glycerine as the coupling agent. The transducers were mounted 180^0 apart on the circumference of the insulator and the test set-up can be seen in figure 5.10 (a). Once again a 10-cycle burst (pulse) of 400kHz, 10Vpeak sine wave was injected into the transmitter transducer. Initially, from the oscilloscope traces captured this method appeared to hold more promise than the Pulse-Echo method as the received pulses changed as the lead electrodes were rotated around the circumference of the insulator. This indicated better transmission of the incident pulse into the insulator, which is attributed to the acoustic impedances (see appendix B.1) of the glycerine, lead and porcelain being closer together than that of the steel bolt and glycerine in the previous method. It soon became apparent that the pattern of the pulses received could not be repeated for the same position on the insulator circumference. This is due to the inability of the clamping method to achieve a repeatable alignment of the transducers and also to secure good contact between the electrode and insulator. The problem of the contact between the electrode and insulator is due to the non-symmetry of the insulator (initially assumed to be symmetrical) rendering the specially cast lead electrodes ineffective.

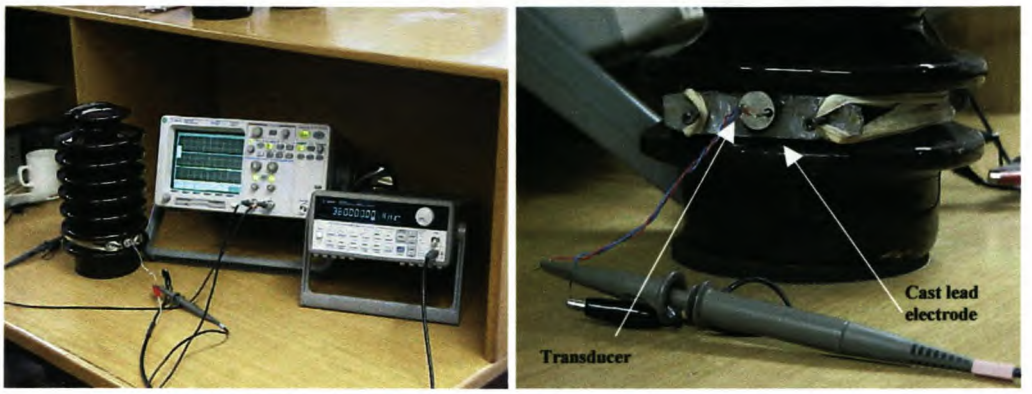

(a) (b)

Figure 5.11: Change of flight experiment with transmitter and receiver mounted on separate lead electrodes each geometrically 180^0 apart on the insulator circumference. (a) experimental set-up and (b) close up of a lead electrode with the transducer mounted on it.

Conclusion

X-ray Detection

- The use of a high energy X-ray source (2MeV machine) made it possible to use a large source-to-film distance ($F = 4m$) and thereby reduce the geometric unsharpness.
- Theoretically the total unsharpness was limited to 0.31mm.
- A value for d was chosen that incorporates the main body of the insulator where the internal flaws are found.
- The 33kV and 22kV insulators were exposed to 150rads/min at 1metre for 2 and 1.6 minutes respectively.

Partial Discharge Detection

- A saturated saltwater solution was found to be a suitable liquid electrode for the inverted insulator housed in a glass tank with an earthed stainless steel base plate.
- A suitable sensitivity with measurable discharge magnitude was achieved with the saltwater solution raised to the second shed of the inverted insulator when using Input Unit 4.
- The test voltage range selected was 0 to 30kV due to the occurrence of unwanted discharges in the test equipment.

- Unwanted surface discharges on the surface of the insulator base in the vicinity of the high voltage electrode were eliminated by filling the depressions in the sulphur cement with sunflower oil.

Ultrasonic Testing

- 40kHz ultrasonic burglar alarm transducers were successfully modified to fit on the M20 bolt and a new resonant frequency was determined.
- The combination of the acoustic impedances of glycerine and the mild steel bolt were theoretically proved to cause 90% of the incident wave being reflected in the Pulse-Echo experiment.
- Examination of appendix B.1 shows that there are no obvious coupling fluids that will match the acoustic impedance of mild steel.
- The inability to obtain repeatable results in the Change of Flight experiment is due to the non-symmetry of the insulators (inconsistent contact area and pressure) and the ineffective clamping method (transducer misalignment) used to secure the lead electrodes to the insulator.

References

1. Robinson Electronic Instruments, "E.R.A. Discharge Detector Model 3 System Manual".
2. Kreuger,F.H., "Partial Discharge Detection in High Voltage Equipment", Butterworths, 1989.
3. Holtzhausen, J.P., "Puncture Testing on Insulators – Project 117/1/D, Report on work done during 1982", Institute for Electronics, University of Stellenbosch, 1982.
4. Heffan,H and Brunty,B.J, "Linatron – High Energy X-ray Applications for Non-Destructive Testing" Diablo Test Associates for Varian Associates, Inc., 1982.
5. Halmslaw,R, "Industrial Radiography- Agfa NDT" ,Agfa-Gevaert N.V. , 1991.

Analysis of Experimental Results

This chapter will present the results obtained from the NDT experiments described in chapter 5 and provide a discussion of the results and the validity of the NDT methods used as tools for identifying internal flaws within the sample insulators.

6.1 X-ray Results

6.1.1 Presentation of X-ray Images

Each insulator is represented by two X-ray images taken 90^0 apart to ensure that the insulator volume is adequately inspected to expose defects. The results of the X-raying of all nine of the insulators are presented using digital photographs of the X-ray images as seen on the radiograph viewing light box. These photographs are shown in figures 6.3 to 6.11. The red arrows on the X-ray images (figures 6.3 to 6.11) give an indication of the proximity of the defects. Detail of some defects visible on a X-ray image were unfortunately lost in the photography process. In order to recapture this detail an artistic impression of the embedded electrode area is included with each X-ray image.

When studying the defect detail on the X-ray images it is necessary to have an indication of the location of these defects with respect to the sulphur cement and the porcelain. Figure 6.1 clearly shows that the insert hole of the 22kV insulator terminates inside the second shed of the insulator while the insert hole of the 33kV terminates between the second and third sheds of the insulator.

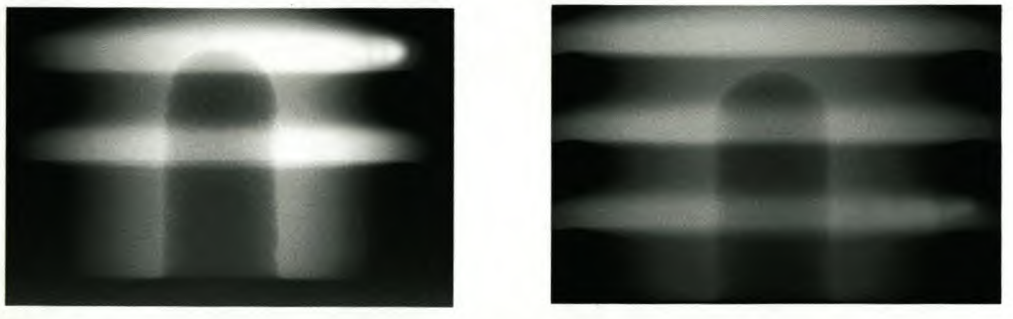

(a) (b)

Figure 6.1: X-ray images of (a) 22kV 620mm creepage and (b) 33kV 1120mm creepage insulators showing the position of their insert holes relative to the insulator sheds with no metal inserts fitted.

The artistic impression in figure 6.2 (b) shows the embedded electrode portion of the porcelain post insulator. It assumes that the top of the insert hole is semicircular in cross-section, but as stated in chapter 1 this is not always the case. As can be seen in figures 6.3 to 6.11 the X-ray images do not help to confirm the insert hole shape. The focus areas (see figure 6.2 (a)) within the sulphur cement are labelled area 1 and area 2 and will be used to categorise the location of voids. Figure 6.2 (b) highlights the points of small radius of curvature on the mild steel insert where higher field strength can be expected. In the artistic impressions of figures 6.3 to 6.11, the blue section represents the sulphur cement while the yellow section represents the defects.

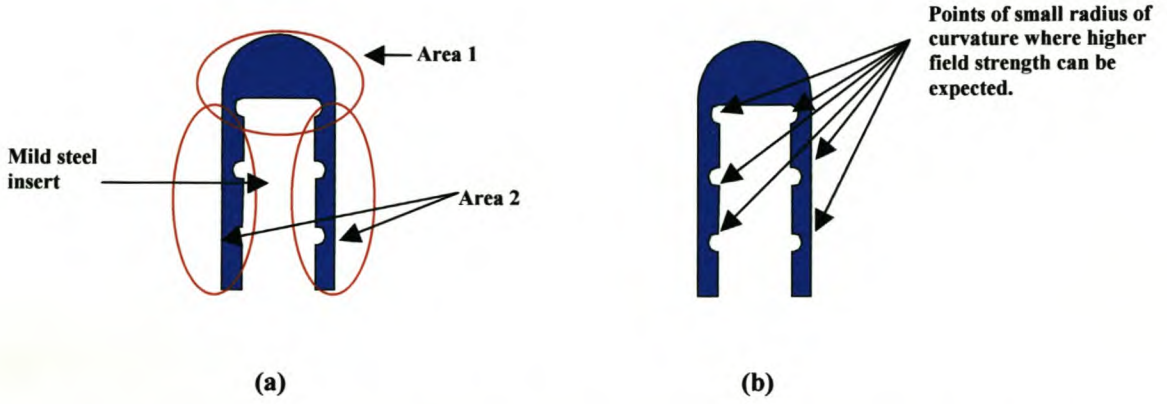

Figure 6.2: Artistic impression of the embedded electrode portion showing, (a) focus areas within the sulphur cement used to give the location of voids and (b) points of small radius curvature on mild steel insert.

6.1.2 X-ray Image Analysis

The X-ray images of the control samples CX, CX1 and CX2 reveal internal defects and these insulators could therefore not be accepted as control samples and were treated as additional sample insulators.

Table 6.1 summarises the flaw types found in each of the nine sample insulators using the X-ray images shown in figures 6.3 to 6.11. Voids caused by de-bonding or stress fractures will not be identified as voids but rather by their cause so that any design or manufacture problems can be highlighted. De-bonding in area 2 should not be confused with sulphur cement voids in this area.

Analysis of the table 6.1 shows that:

- the most commonly found flaw types are voids in the sulphur cement and de-bonding between the sulphur cement and porcelain.
- sulphur cement voids appeared in all nine of the insulator samples while de-bonding occurred in eight of the samples.
- the largest voids in the sulphur cement occurred in area 1 (see figure 6.2) while low volume voids occurred in area 2.
- porcelain stress fractures and voids in the porcelain were less common with only two of the 33kV insulators showing stress fractures and three of the 22kV insulators showing voids in the porcelain.
- the porcelain voids found in samples A, B and C have a symmetrical pattern. This only appears in these three insulators which were among the six insulators that were purposely made for this study to include sulphur cement voids. The porcelain voids could have been caused by the manufacturing technique used to produce these three faulty samples.

Table 6.1: Summary of the flaws identified from the X-ray images shown in figures 6.3 to 6.11.

Insulator sample	Void/s in sulphur cement		De-bonding		Porcelain stress fractures (area 1 only)	Void/s in porcelain
	area 1	area 2	area 1	area 2		
2	Yes	No	Yes	No	Yes	No
3	Yes	No	Yes	No	Yes	No
4	Yes	Yes	No	No	No	No
CX2	Yes	No	Yes	No	No	No
CX1	Yes	Yes	Yes	No	No	No
A	Yes	Yes	No	Yes	No	Yes
B	Yes	Yes	No	Yes	No	Yes
C	Yes	No	No	Yes	No	Yes
CX	Yes	No	Yes	Yes	No	No

6.1.3 Validity of X-ray as a NDT Technique

Although only some defects are visible on the digital photographs of the X-ray images in figures 6.3 to 6.11, there is good defect discernability when using good film viewing conditions. Defect detail as small as a crack, stress fracture or de-bonding can be seen. X-ray as a NDT technique is therefore an effective technique for finding internal flaws in porcelain post insulators.

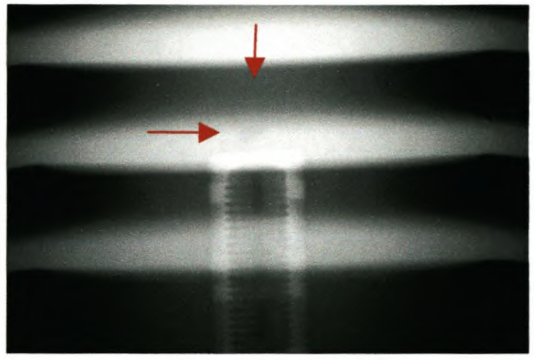

(a)

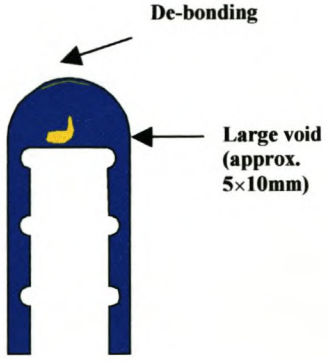

(b)

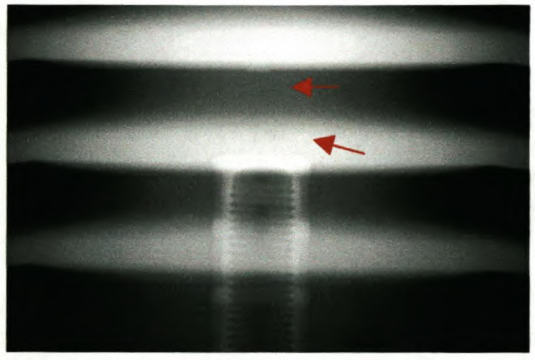

(c)

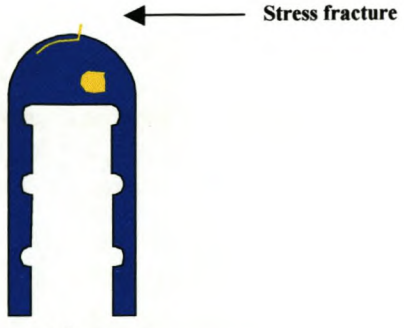

(d)

Figure 6.3: X-ray image of sample insulator 2. (a) digital image at 0^0, (b) artistic impression of embedded electrode area at 0^0, (c) digital image at 90^0, (b) artitistic impression of embedded electrode area at 90^0.

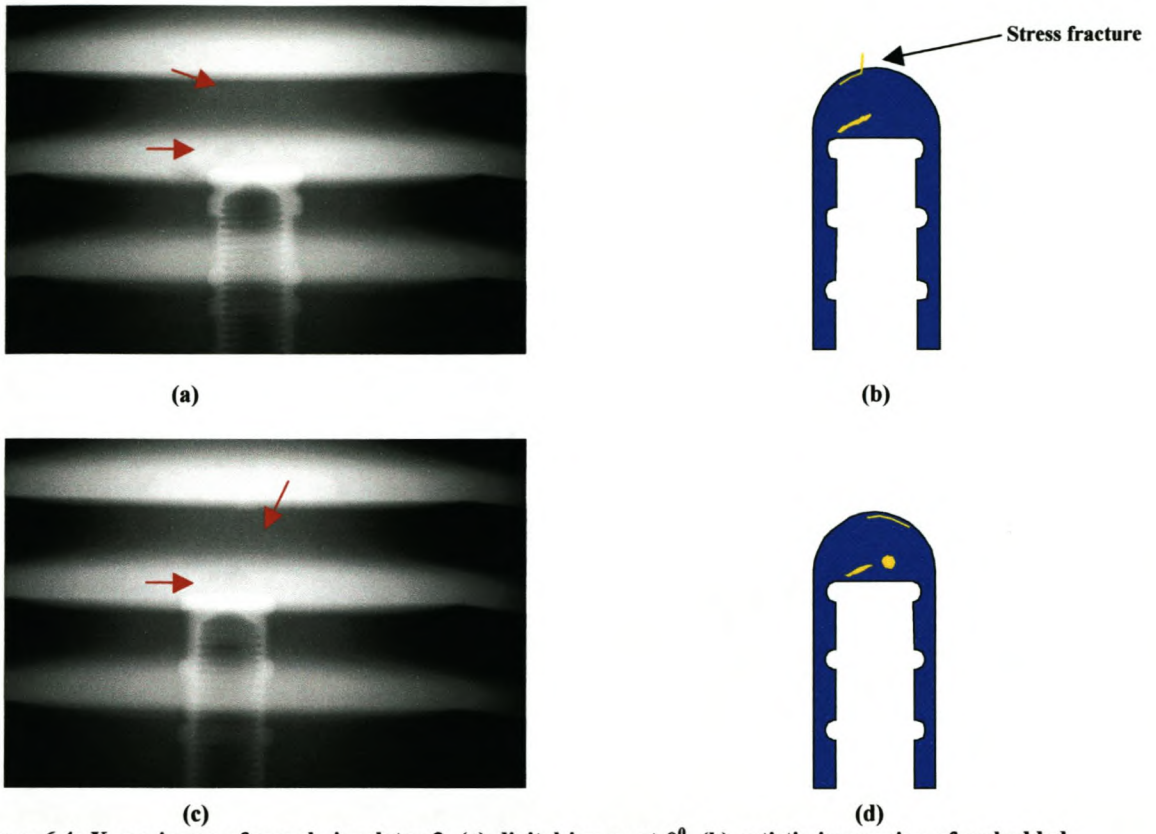

Figure 6.4: X-ray image of sample insulator 3. (a) digital image at 0^0, (b) artistic impression of embedded electrode area at 0^0, (c) digital image at 90^0, (d) artitistic impression of embedded electrode area at 90^0.

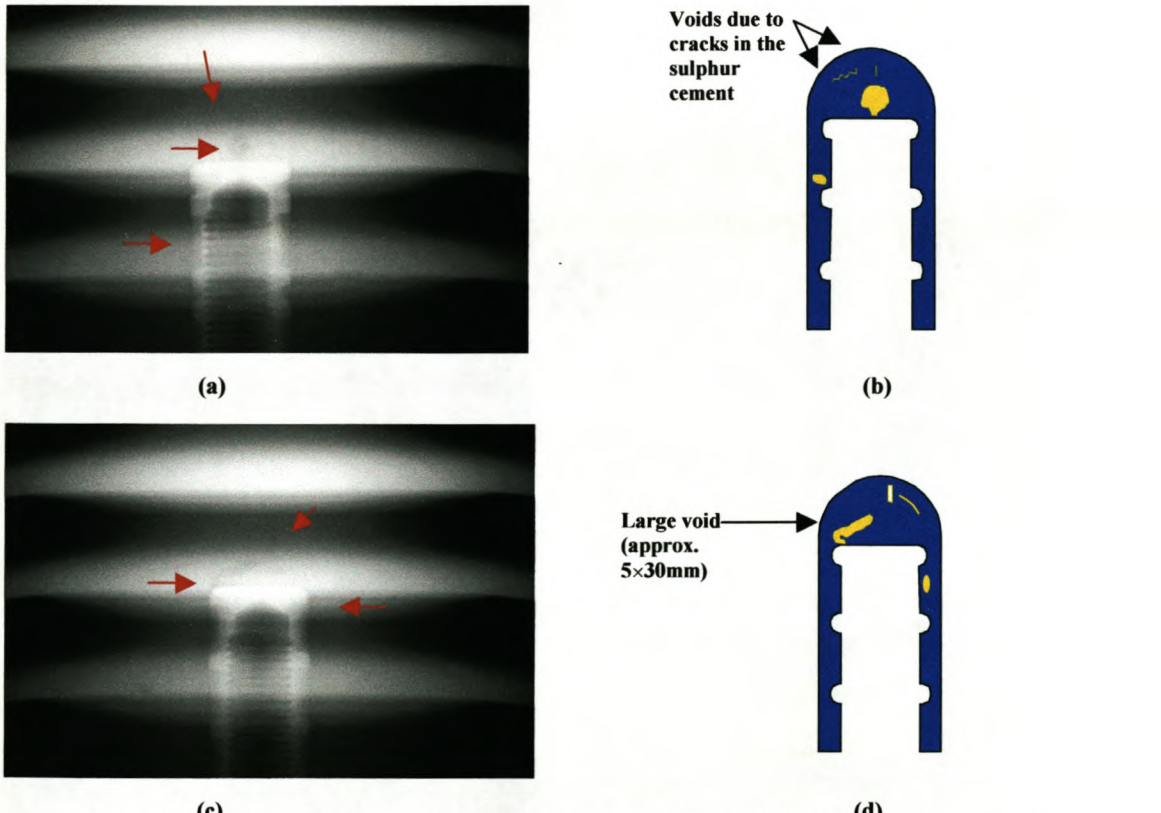

Figure 6.5: X-ray image of sample insulator 4. (a) digital image at 0^0, (b) artistic impression of embedded electrode area at 0^0, (c) digital image at 90^0, (d) artitistic impression of embedded electrode area at 90^0.

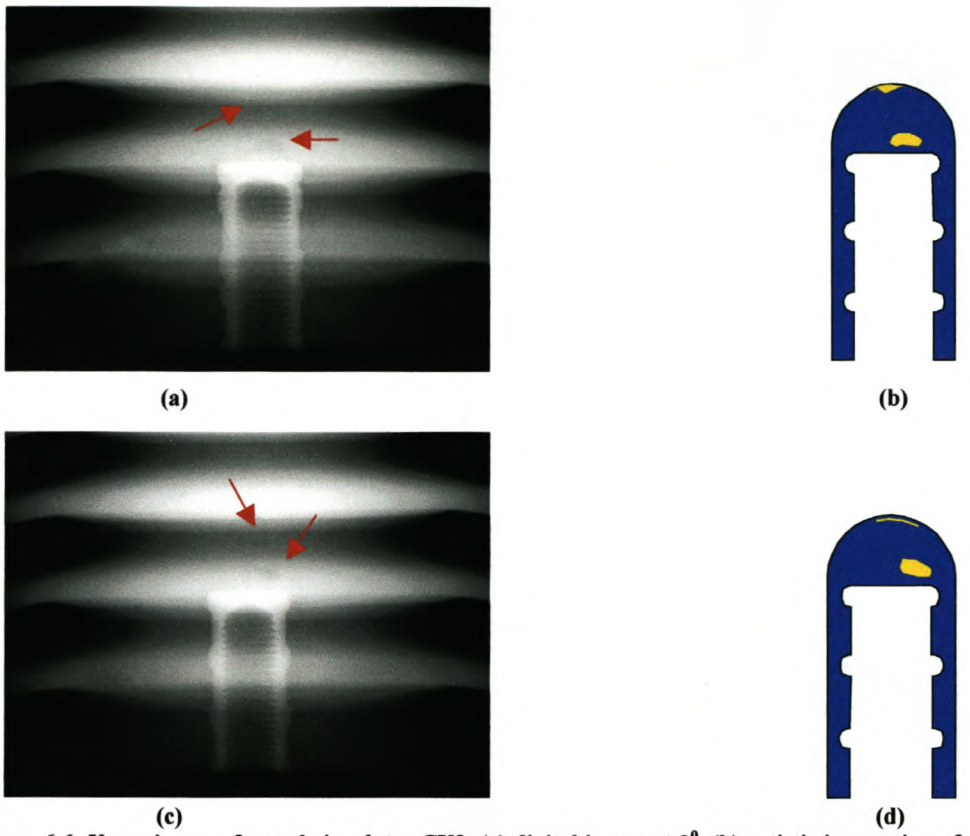

Figure 6.6: X-ray image of sample insulator CX2. (a) digital image at 0^0, (b) artistic impression of embedded electrode area at 0^0, (c) digital image at 90^0, (d) artitistic impression of embedded electrode area at 90^0.

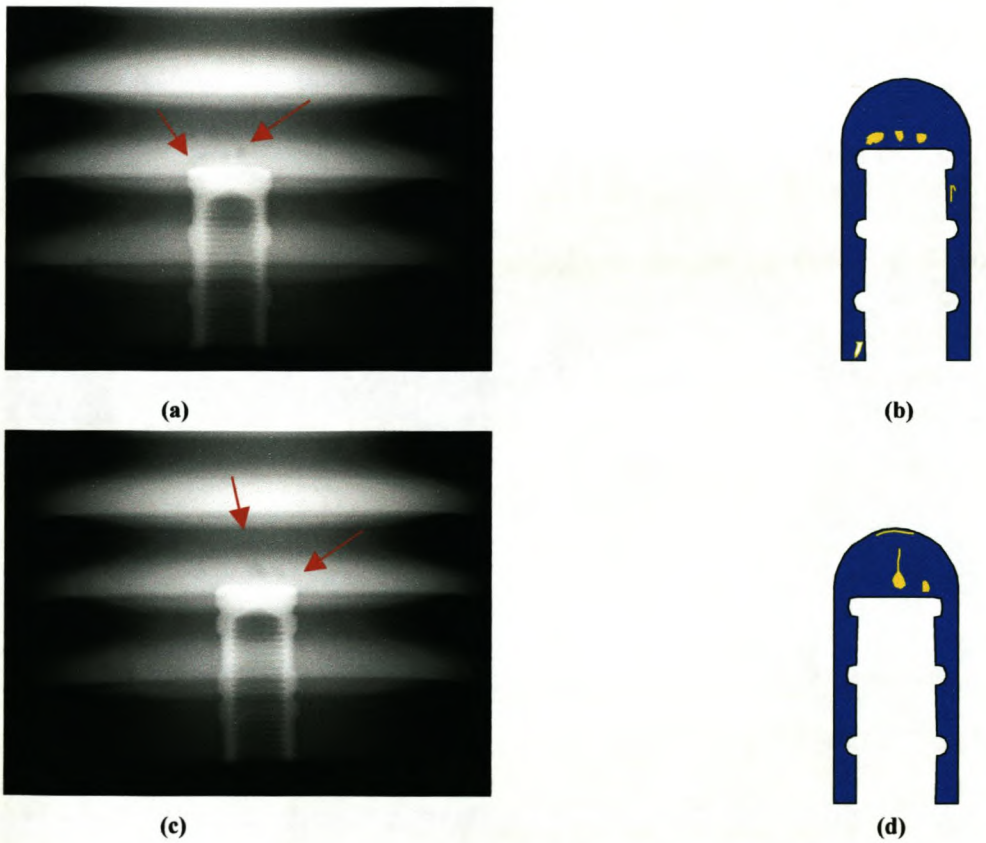

Figure 6.7: X-ray image of sample insulator CX1. (a) digital image at 0^0, (b) artistic impression of embedded electrode area at 0^0, (c) digital image at 90^0, (d) artitistic impression of embedded electrode area at 90^0.

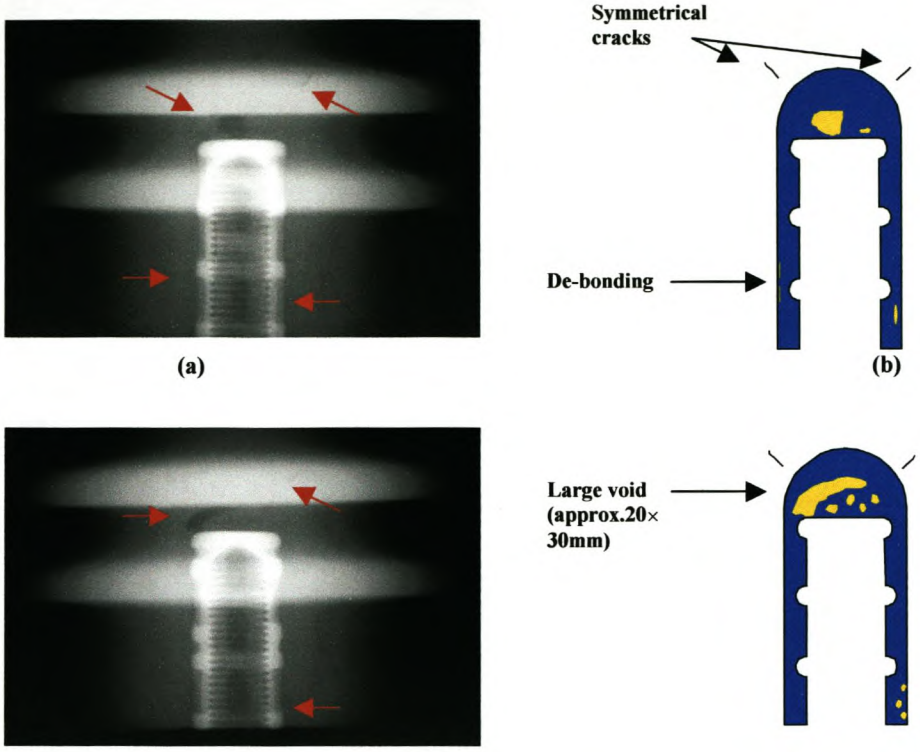

Figure 6.8: X-ray image of sample insulator A. (a) digital image at 0^0, (b) artistic impression of embedded electrode area at 0^0, (c) digital image at 90^0, (d) artitistic impression of embedded electrode area at 90^0.

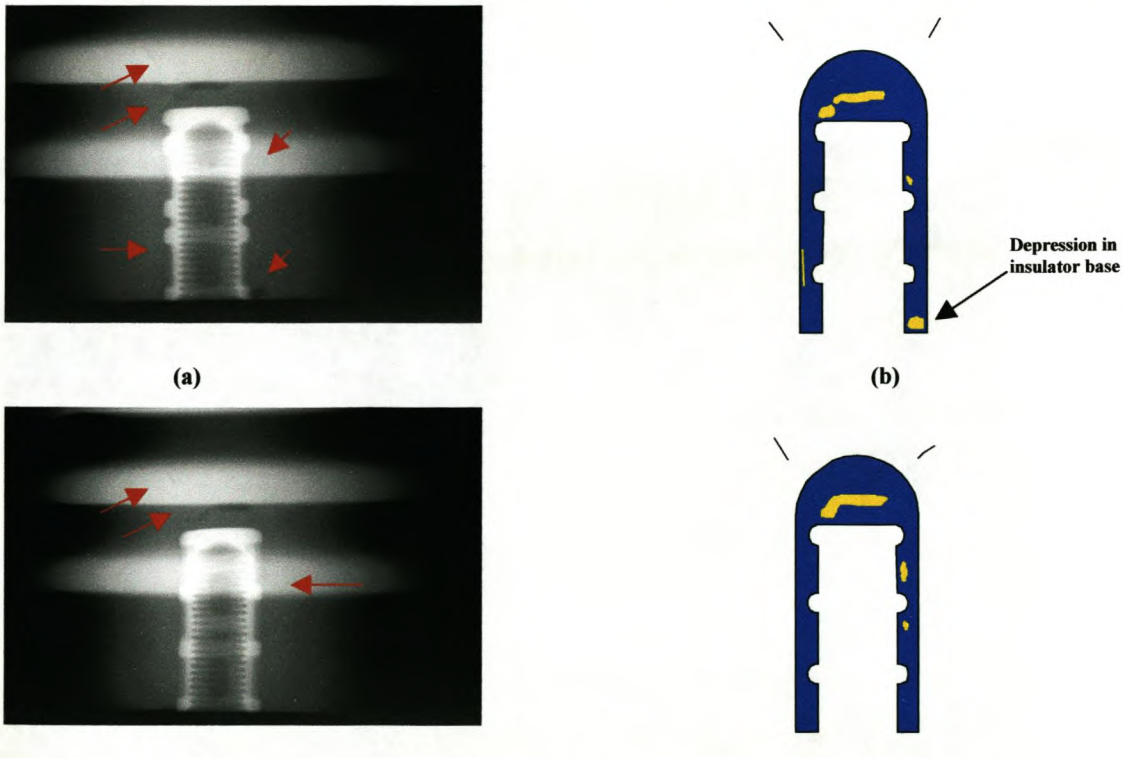

Figure 6.9: X-ray image of sample insulator B. (a) digital image at 0^0, (b) artistic impression of embedded electrode area at 0^0, (c) digital image at 90^0, (d) artitistic impression of embedded electrode area at 90^0.

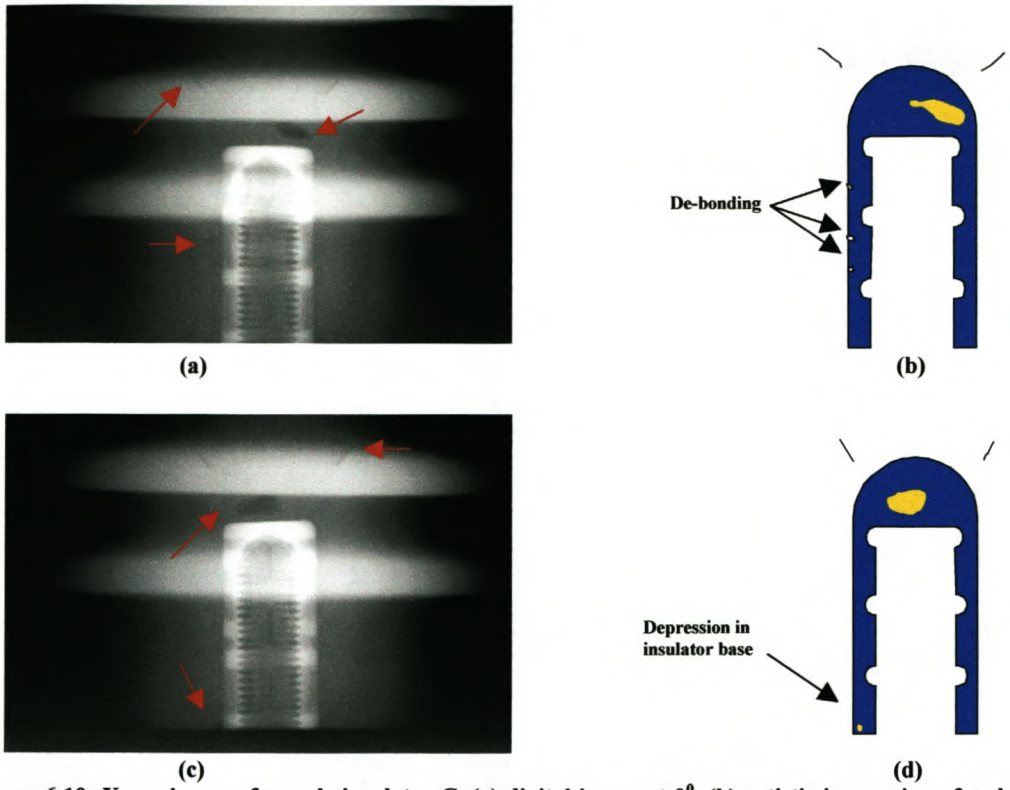

Figure 6.10: X-ray image of sample insulator C. (a) digital image at 0^0, (b) artistic impression of embedded electrode area at 0^0, (c) digital image at 90^0, (d) artitistic impression of embedded electrode area at 90^0.

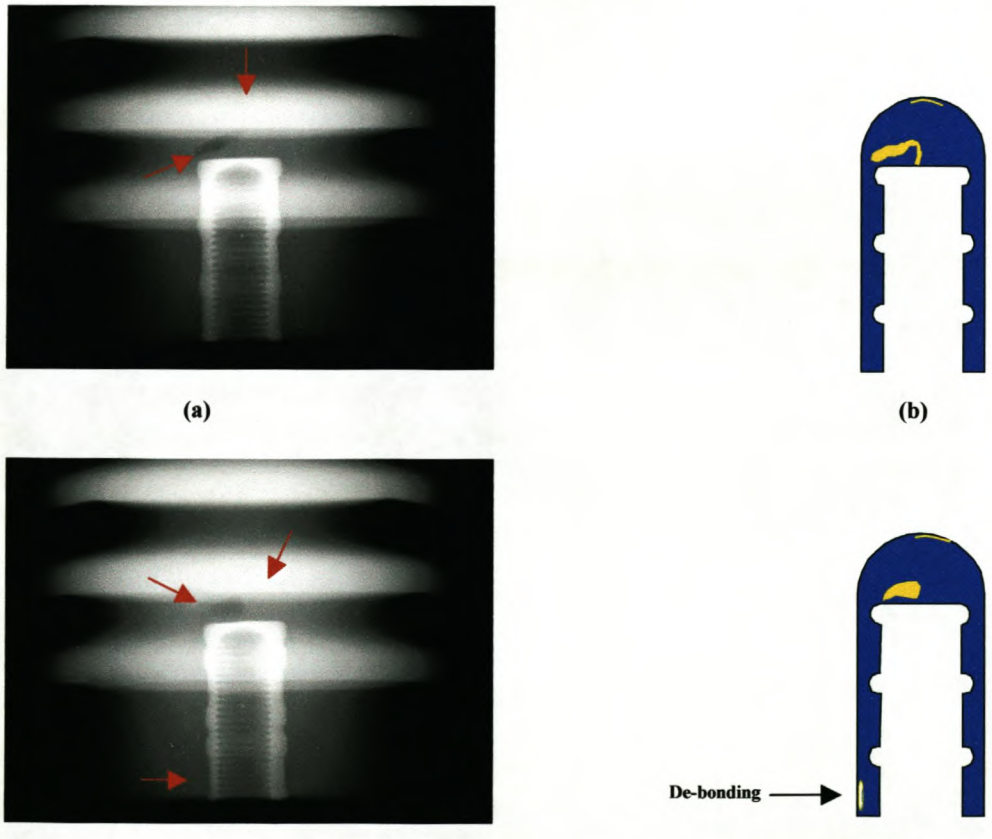

Figure 6.11: X-ray image of sample insulator CX. (a) digital image at 0^0, (b) artistic impression of embedded electrode area at 0^0, (c) digital image at 90^0, (d) artitistic impression of embedded electrode area at 90^0.

6.2 Partial discharge results

The results of the PD experiments for each of the nine sample insulators are separately tabulated in appendices C.1 to C.9. Each table details the attenuation value (dB), the step-wave output voltage (mV), and the discharge magnitude (pC) for each 1kV adjustment of the test voltage from PD inception to extinction. The attenuation values were obtained by matching the calibration pulse to the steady PD pulses by following the E.R.A. discharge detector operating instructions given in appendix A.3. Step-wave output voltages were obtained from appendix A.1 and the discharge magnitudes were then calculated using equation 4.11. The X-Y diagrams for each of the sample insulators were produced by making use of Microsoft Excel and plotting test voltage (linear scale) against discharge magnitude (logarithmic scale). These X-Y diagrams are shown in figures 6.12 to 6.20.

Examination of the artistic impressions of each X-ray image reveals that most of the sample insulators have multiple voids, some limited and others of a more extended nature (see figure 4.18). Voids in the vicinity of small radius of curvature on the mild steel insert (see figure 6.2 (b)) experience higher electric field strength than voids elsewhere, therefore it is to be expected that these will be more stressed and more likely to produce PD activity. Large volume voids may not produce any PD activity as a result a large void depth in the direction of the applied electric field and the limited test voltage (30kV).

As stated in section 4.2.3 the discharge magnitude increases with the volume of the discharge site. Therefore the maximum discharge magnitude and void location inside the electric field gives an indication of which void could possibly be discharging in an insulator with multiple internal voids. It should be noted that only a portion may be discharging and not necessarily the entire void, which can make the prediction of discharging extremely difficult and sometimes speculative.

As figures 4.15, 4.16 and 4.17 refer to samples with a single void discharging, matching these figures to the X-Y diagrams of the nine sample insulators was only possible for sample insulators 2 and CX which have few voids of vastly varying

volume. The great variation in volume and relatively small maximum discharge magnitude of these samples makes the prediction of the discharging void much easier and verifies the X-Y diagram match.

Table 6.2 summarises the inception and extinction voltages, and maximum discharge magnitude of each of the nine sample insulators.

Table 6.2: Summary of the inception and extinction voltages, and maximum discharge magnitude of each of the nine sample insulators.

Insulator sample	Inception voltage ($kV_{r.m.s.}$)	Extinction voltage ($kV_{r.m.s.}$)	Maximum discharge magnitude (pC)
2	13	12	18.16
3	11	6	101.9
4	13	12	570.43
CX2	4	16	101.5
CX1	10	9	57.04
A	22	20	1015
B	16	10	9043.65
C	22	15	12.79
CX	21	19	18.07

Sample 2

The PD inception and extinction voltages were 13kV and 12kV respectively. The maximum discharge magnitude of 18.16pC occurred while increasing the test voltage in the range 19 to 25kV.

The squarely shaped X-Y diagram (figure 6.12) approximately matches figure 4.15, which indicates a discharge in a void of limited dimensions (see figure 4.18). This can be attributed to the de-bonding or a portion of it in area 1 as shown figures 6.3 (b) and (d). The large volume void and the stress fracture in area 1 as seen in figures 6.3 (b) and (d) would not be sufficiently stressed by the test voltage as they have a large depth in the direction of the applied electric field. The sample's maximum discharge magnitude is not indicative of the discharge magnitude associated with the large volume void.

Sample 3

The PD inception and extinction voltages were 11kV and 6kV respectively. The maximum discharge magnitude of 101.9pC occurred while increasing the test voltage in the range 27 to 28kV. During the PD experiment large magnitude self-extinguishing discharges were observed on the ellipse of the E.R.A. PD detection monitor with increasing test voltage. These intermittent discharges are due to asymmetrically shaped voids [1].

The X-Y diagram 6.13 could not be matched to either of figures 4.15, 4.16 or 4.17. Figures 6.4 (b) and (d) indicate that the insulator has de-bonding, a stress fracture and two low volume voids in the vicinity of the top of the embedded electrode. This makes the prediction of the discharging void/s unlikely, without proven discharge magnitudes for specific void types, shapes, volumes and locations under the same experimental conditions.

Sample 4

The PD inception and extinction voltages were 13kV and 12kV respectively. The maximum discharge magnitude of 570.43pC occurred at 27kV with increasing test voltage.

The X-Y diagram 6.14 could not be matched to either of figures 4.15, 4.16 or 4.17. Figures 6.5 (b) and (d) indicate that sample 4 has multiple voids of small and large volume in both areas 1 and 2 with differing orientation with respect to the applied electric field. The number and variety of internal flaws in the insulator make the prediction of the discharging void unlikely, without proven discharge magnitudes for specific void types, shapes, volumes and locations under the same experimental conditions.

Sample CX2

The PD inception and extinction voltages were 4kV and 16kV respectively. The maximum discharge magnitude of 101.5pC occurred at 29kV while decreasing the

test voltage. The low inception voltage is an indication of a shallow void in the direction of the applied electric field. Large magnitude self-extinguishing discharges were observed on the ellipse of the E.R.A. PD detection monitor with increasing test voltage. These intermittent discharges are due to asymmetrically shaped voids [1].

The X-Y diagram 6.15 could not be matched to either of figures 4.15, 4.16 or 4.17. Figures 6.6 (b) and (d) indicate that sample CX2 has de-bonding and a large volume void in area 1. The insulator maximum discharge magnitude is an indication that the de-bonding could be discharging. A higher maximum discharge magnitude would be expected for discharging in the large volume void.

Sample CX1

The PD inception and extinction voltages were 10kV and 9kV respectively. The maximum discharge magnitude of 57.04pC occurred at 20kV while increasing the test voltage. Large magnitude self-extinguishing discharges were observed on the ellipse of the E.R.A. PD detection monitor with increasing and decreasing test voltage. These intermittent discharges are due to asymmetrically shaped voids [1].

The X-Y diagram 6.16 could not be matched to either of figures 4.15, 4.16 or 4.17. Figures 6.7 (b) and (d) indicate that sample CX1 has multiple voids of small and large volume in both areas 1 and 2 with differing orientation with respect to the applied electric field. The maximum discharge magnitude of this insulator is an indication of discharging in a void of small volume or a portion thereof. The prediction of the discharging void in this insulator is unlikely without proven discharge magnitudes for specific void types, shapes, volumes and locations under the same experimental conditions.

Sample A

The PD inception and extinction voltages were 22kV and 20kV respectively. The maximum discharge magnitude of 1015pC occurred while increasing the test voltage in the range 29 to 30kV. Large magnitude self-extinguishing discharges were observed on the ellipse of the E.R.A. PD detection monitor in the voltage range 29kV

– 30kV – 27kV. These intermittent discharges are due to asymmetrically shaped voids [1].

The X-Y diagram 6.17 could not be matched to either of figures 4.15, 4.16 or 4.17. Figures 6.8 (b) and (d) indicate that sample A has multiple voids of small and large volume in both areas 1 and 2 with differing orientation with respect to the applied electric field. The prediction of the discharging void in this insulator is unlikely. The large volume void seen in Figure 6.8 (d) is the largest of all found in the any of the sample insulators. The maximum discharge magnitude of this insulator gives an indication of a void of larger volume discharging than in the previous samples, but this discharge magnitude is not indicative of the discharge activity associated with the largest void. The maximum test voltage of 30kV is not large enough to cause a discharge in this void.

Sample B

The PD inception and extinction voltages were 16kV and 10kV respectively. The maximum discharge magnitude of 9043.65pC occurred while decreasing the test voltage in the range 30 to 26kV. This sample's maximum discharge magnitude was the largest of all the insulators measured.

The X-Y diagram 6.18 could not be matched to either of figures 4.15, 4.16 or 4.17. Figures 6.9 (b) and (d) indicate that sample B has multiple voids of small and large volume in both areas 1 and 2 with differing orientation with respect to the applied electric field. The void caused by the depression in the insulator base (figure 6.9 (b)) can be ignored as it is filled with vegetable oil to prevent surface discharges. The high maximum discharge magnitude of this insulator is an indication that a void of large volume or a portion thereof is discharging.

Sample C

The PD inception and extinction voltages were 22kV and 15kV respectively. The maximum discharge magnitude of 12.79pC occurred at 30kV.

The X-Y diagram 6.19 could not be matched to either of figures 4.15, 4.16 or 4.17. The low maximum discharge magnitude of this sample is indicative of a low volume void discharging and could possibly be one of the de-bonding voids in area 2 of figure 6.10 (b). The void caused by the depression in the insulator base (figure 6.10 (d)) can be ignored as it is filled with vegetable oil to prevent surface discharges. The large volume void seen in figures 6.10 (b) and (d) was not stressed sufficiently by the test voltage as the sample's maximum discharge magnitude is not indicative of this level of discharge activity.

Sample CX

The PD inception and extinction voltages were 21kV and 19kV respectively. The maximum discharge magnitude of 18.07pC occurred while increasing the test voltage in the ranges 23 to 25kV and 27kV to 29kV.

The squarely shaped X-Y diagram (figure 6.20) approximately matches figure 4.15, which indicates a discharge in a void of limited dimensions (see figure 4.18) and this can be attributed to the de-bonding void or a portion thereof, as shown in figures 6.11 (b) and (d). The sample's maximum discharge magnitude is not indicative of a large volume void discharging.

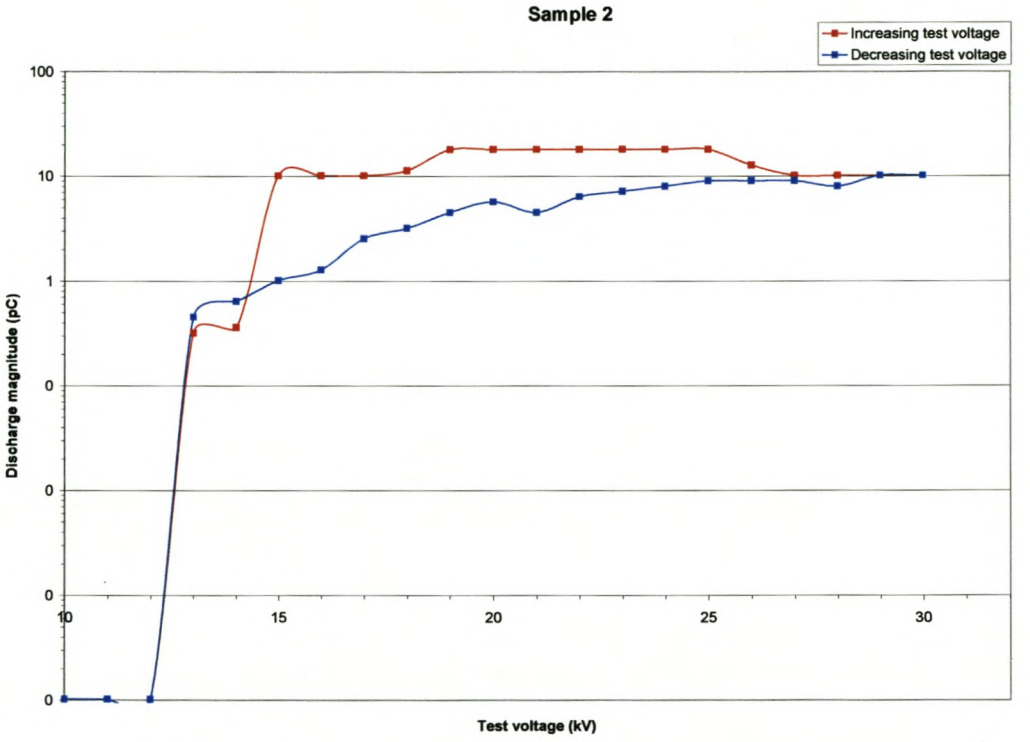

Figure 6.12: X-Y diagram of PD in insulator sample 2.

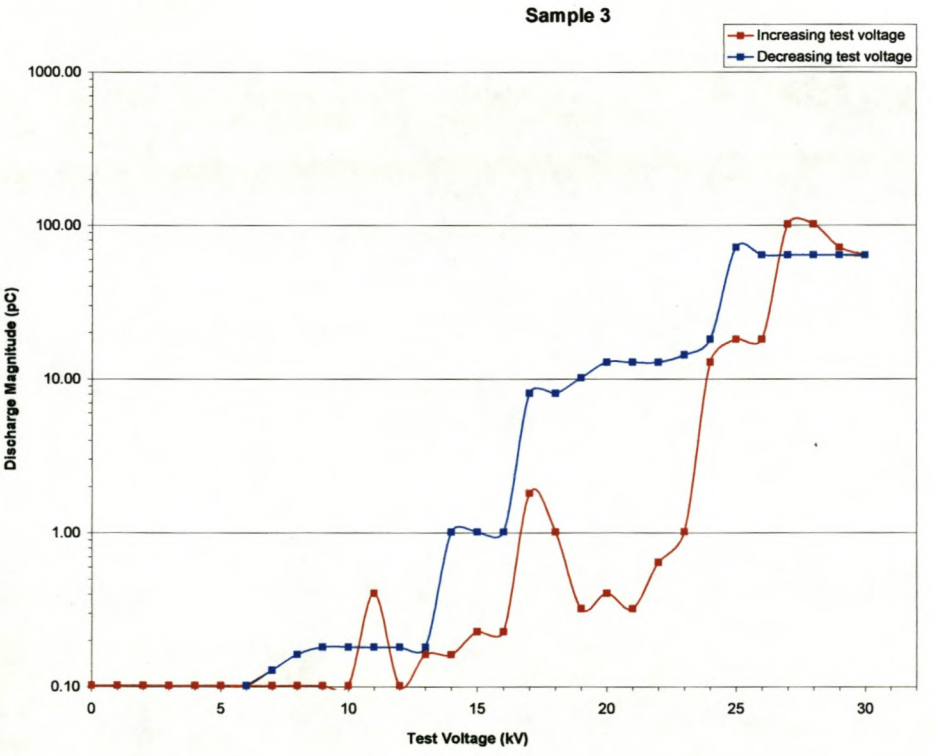

Figure 6.13: X-Y diagram of PD in insulator sample 3.

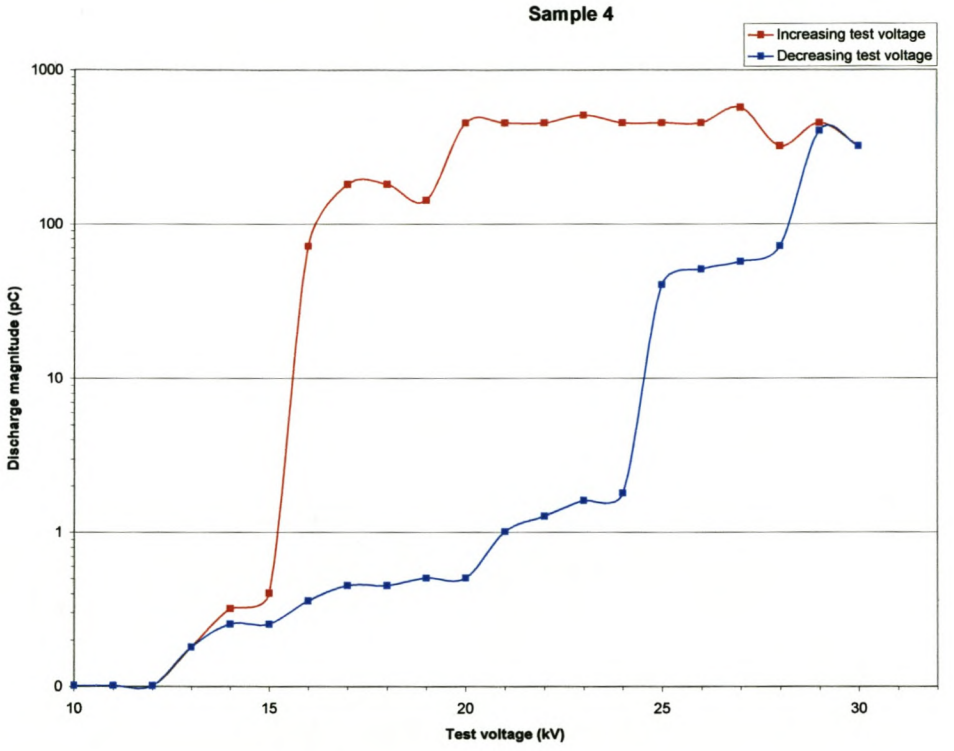

Figure 6.14: X-Y diagram of PD in insulator sample 4.

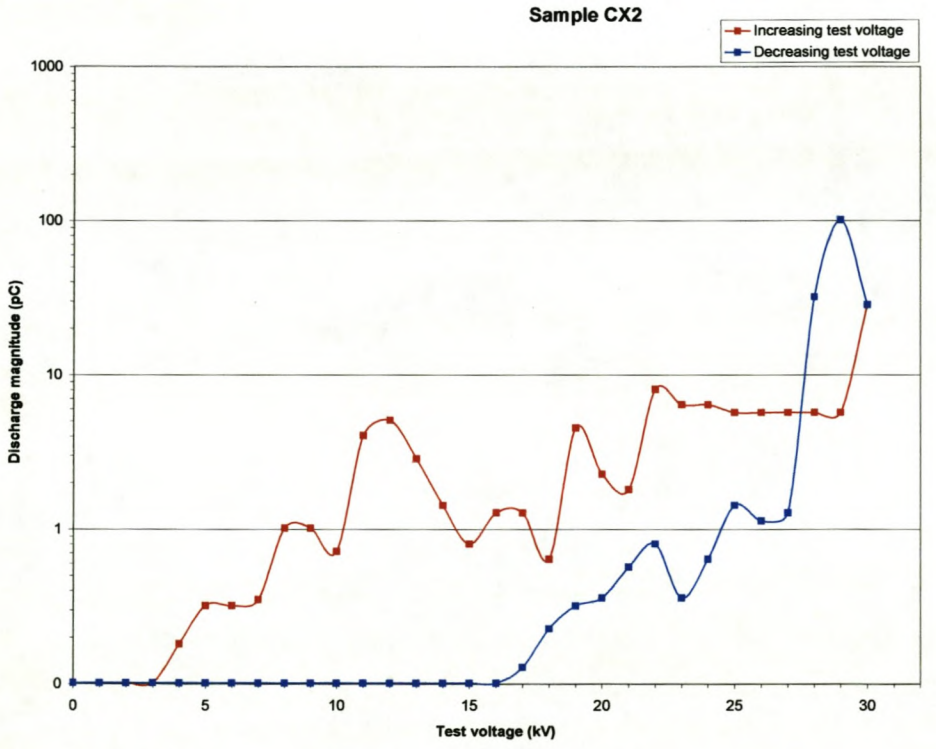

Figure 6.15: X-Y diagram of PD in insulator sample CX2.

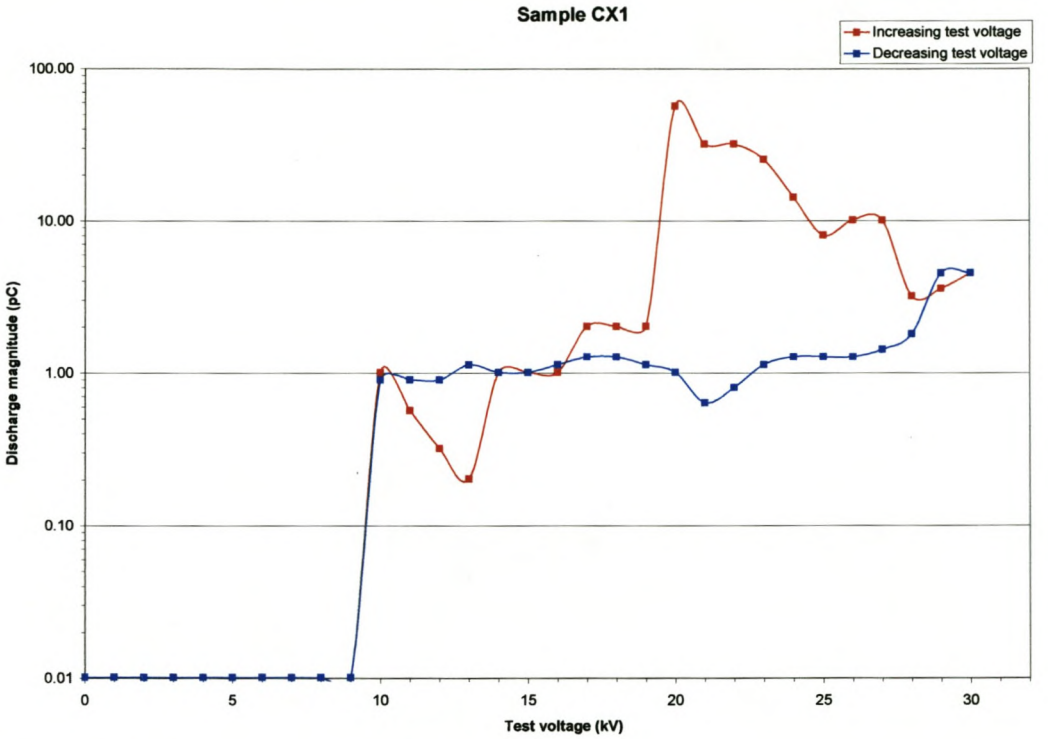

Figure 6.16: X-Y diagram of PD in insulator sample CX1.

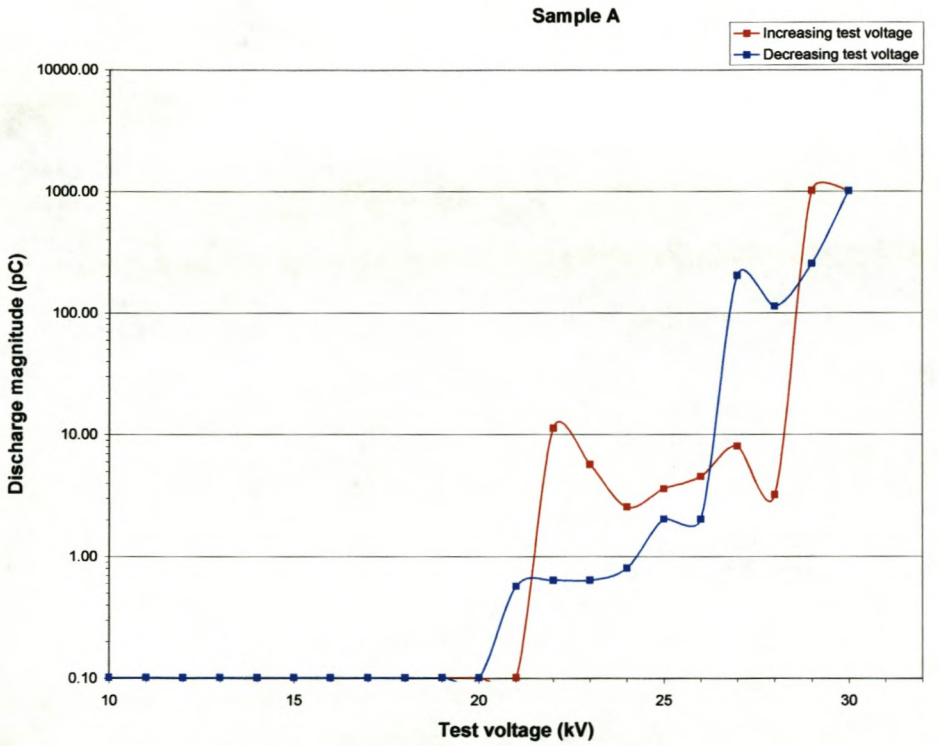

Figure 6.17: X-Y diagram of PD in insulator sample A.

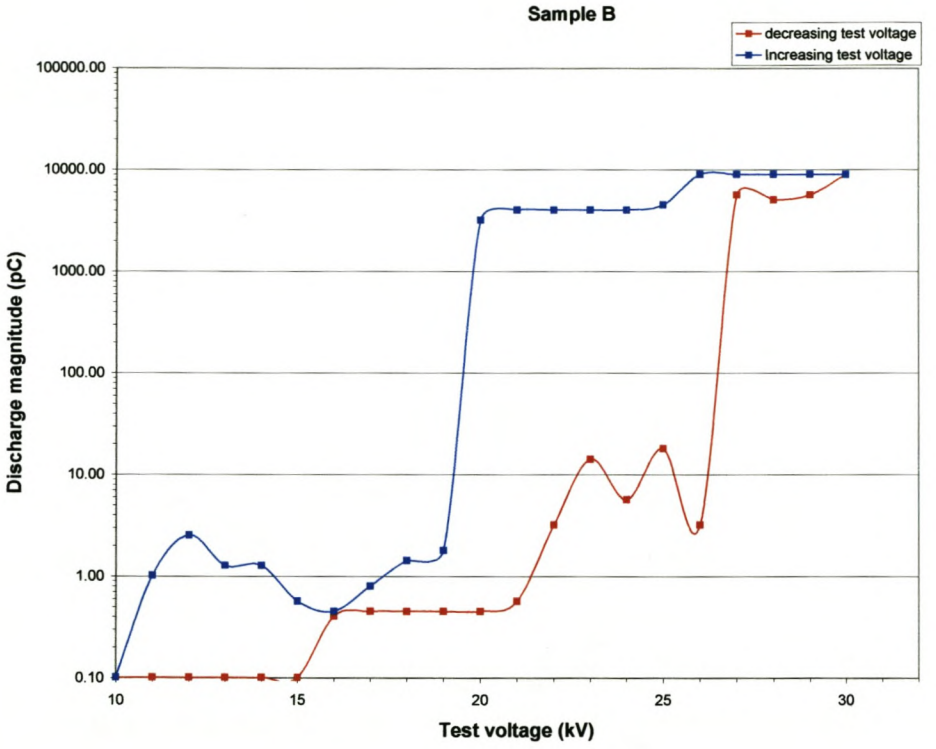

Figure 6.18: X-Y diagram of PD in insulator sample B.

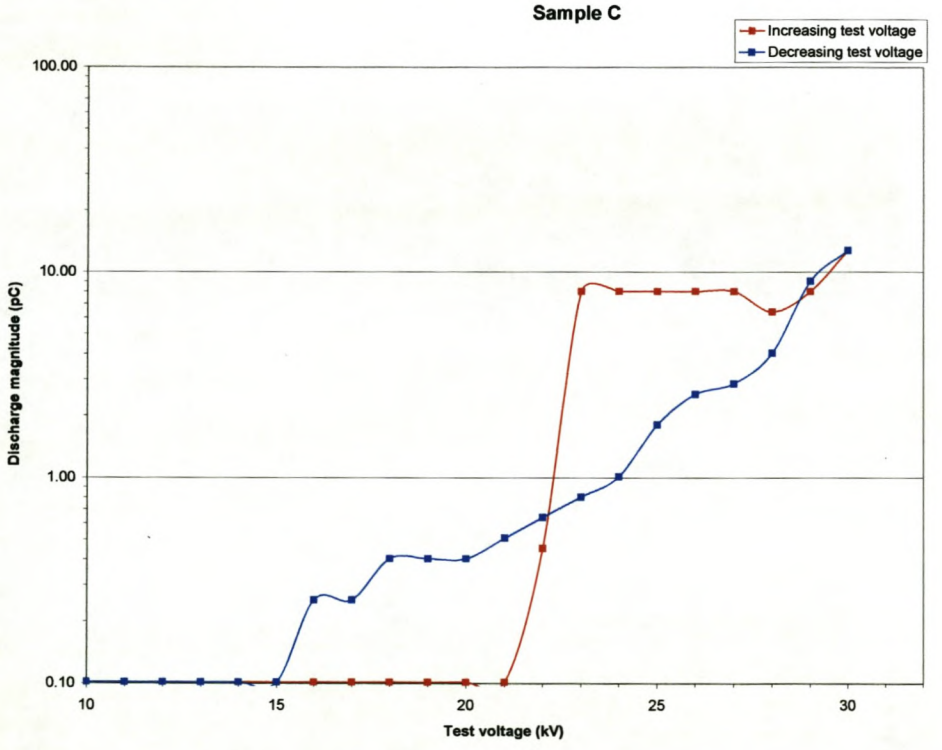

Figure 6.19: X-Y diagram of PD in insulator sample C.

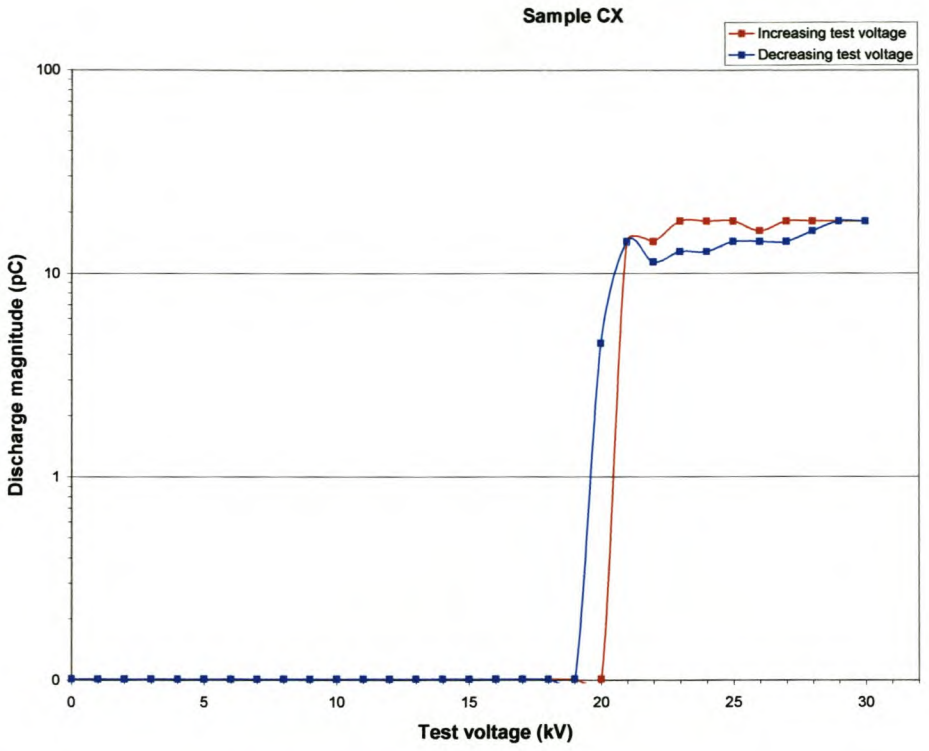

Figure 6.20: X-Y diagram of PD in insulator sample CX.

6.2.1 Medium Wave Radio Receiver

Medium wave (MW) radio reception interference from PD activity was the forerunner of the E.R.A. Discharge Detector. A radio receiver selected to the medium wave band was used during the PD testing of sample B to investigate its possible usefulness as a quality control measure in the insulator factory. With the MW band tuned to approximately 1350kHz, checks for corona and then internal discharges were performed. Both the corona and internal discharges were audible over the loudspeaker. Only large PD magnitudes (approximately 5000pC) were audible with the available radio receiver, requiring much refinement of this technique for use as a PD detector. It does not allow for distinguishing between the different types of discharges found in high voltage equipment. With the E.R.A. Discharge Detector already well established as a PD detector there does not appear to be any added value or need to pursue the MW radio receiver method.

6.3 Ultrasonic experimental results

Both the ultrasonic experimental methods described in section 5.3 were employed to detect internal flaws in the sample insulators. Problems of non-symmetry of the insulator, acoustic impedance mismatching, non-availibility of suitable coupling fluids, and transducer alignment were the major drawbacks experienced with this NDT technique.

6.3.1 Pulse-Echo Method

The calculation of the percentage reflection of the incident wave in section 5.3.1.2 is confirmed by figure 6.21. Other than amplitude changes there is no difference between the reflected waves received from the end of the M20 steel bolt-in air, -in sample A or –in sample CX.

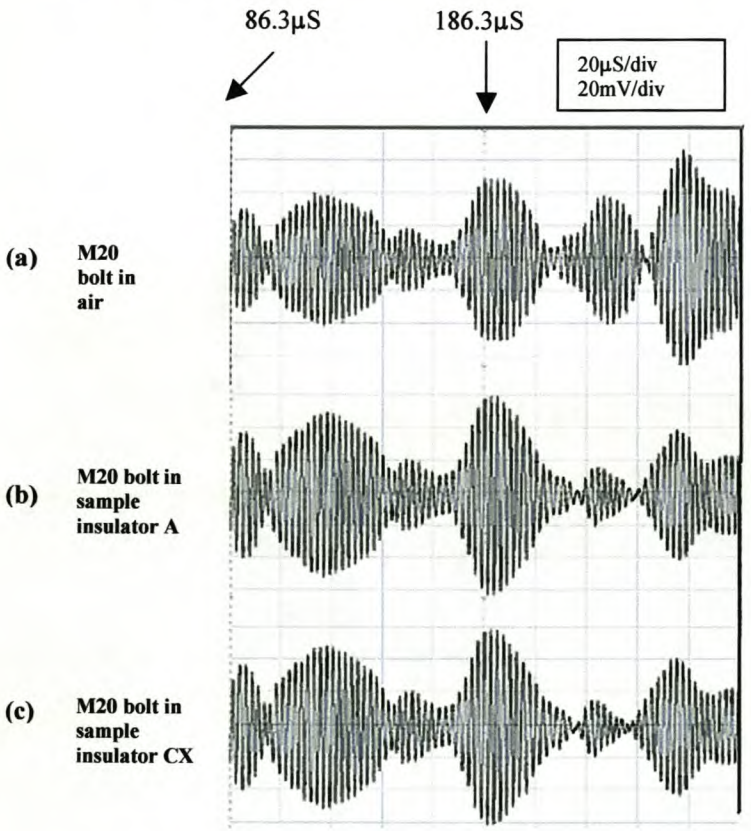

Figure 6.21: Oscilloscope traces of the reflected waves received by the receiver transducer for (a) M20 bolt in air, (b) M20 bolt in sample insulator A and (c) M20 bolt in sample insulator CX.

Figure 6.22 is a zoom of the first 2.5 time divisions of figure 6.21. This is the portion of the trace that should contain the reflections from the voids seen in figures 6.8 (b) and (d), and 6.11 (b) and (d). This confirms that the transmission of the incident wave

into the insulator is negligible and the experiment was not successful in detecting internal flaws in the insulator samples A and CX. The Pulse-Echo experimentation was then ceased.

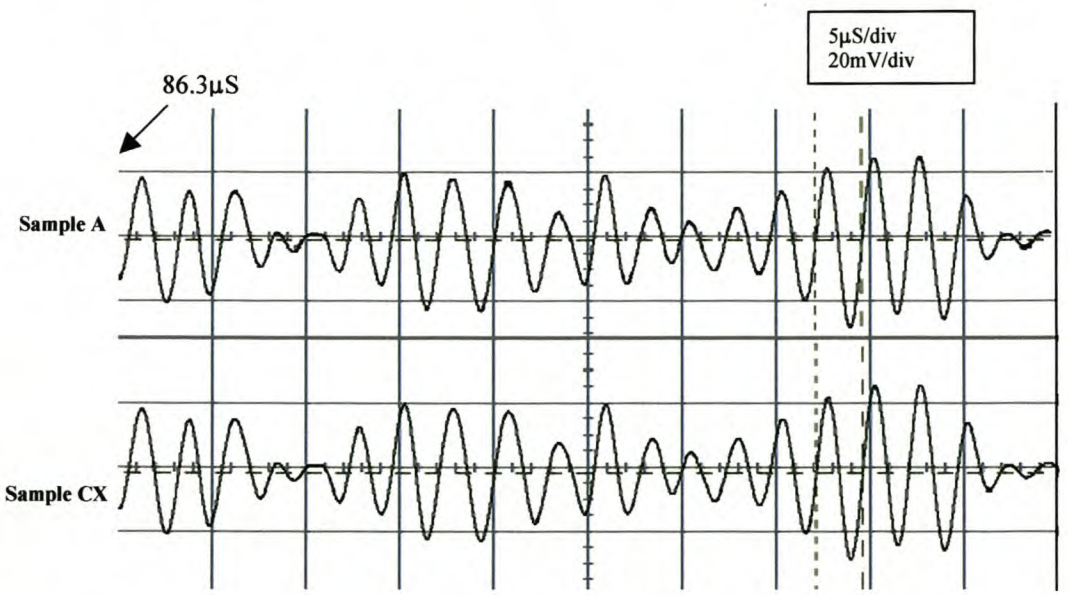

Figure 6.22: Zoom of the first 2.5 time divisions of figure 6.21.

6.3.2 Change of Flight Method

The oscilloscope traces displayed from the received pulses were initially encouraging as there was a variation for each adjustment of the transducer positions on the circumference of the test insulator. When the transducers were shifted back to a previous position the original oscilloscope trace could not be repeated. This inability to achieve repeatable results was due to the use of the lead electrodes that could not secure good physical contact between the insulator and itself. The poor contact experienced is due to the non-symmetry of the insulator, which was initially assumed to be symmetrical. Also, the clamping method used to attach the lead electrodes to the insulator was not effective in aligning the transducers. This led to the inability to secure a repeatable pattern of received pulses for the same position on the insulator's circumference. The Change of Flight experimentation was then ceased.

Conclusions

The analysis of the experimental results of the three NDT methods led to the following concluding remarks:

X-ray Detection

- The X-raying method of NDT revealed internal flaws in all of nine the sample insulators.
- The shape of the top of the insert hole cannot be discerned on the X-ray image, as there is a lack of contrast between the sulphur cement and porcelain.
- Voids appeared to be assymmetrical in shape.
- Void location and size can be determined.
- Two X-ray images per sample insulator were taken 90^0 apart and proved an effective method of ensuring that the insulator volume was adequately inspected for internal flaws.
- The insulator control samples were rejected based on the X-ray evidence.
- The most common flaw types found were voids in the sulphur cement which occurred in all nine of the sample insulators, followed by de-bonding between the sulphur cement and porcelain in eight of the sample insulators.
- The largest voids occurred in area 1 of the sulphur cement while low volume voids occurred in area 2.
- Porcelain stress fractures and voids in the porcelain were less common with only two of the 33kV insulators showing stress fractures and three of the 22kV insulators showing voids in the porcelain.
- The artistic impressions proved helpful in recapturing the detail lost in the photographing of the X-ray images.

PD Detection

- The ability to measure discharge activity is an indication that PD detection was successful as a NDT method for detecting the presence of internal flaws in the sample insulators. The number, location, shape and orientation of voids cannot be determined using this method.
- The X-ray images greatly improved the ability to make predictions about PD activity inside the sample insulators.

- The prediction of discharging void/s in an insulator is unlikely without proven discharge magnitudes for each specific void type, shape, volume and location within the insulator under the same experimental conditions.
- Only large discharge magnitudes of corona or internal discharges were audible when using the available MW radio receiver, but this method is unable to distinguish between the different discharge types found in high voltage equipment. The E.R.A. Discharge Detector is well established as a PD detector and there does not appear to be any added value or need to pursue the MW radio receiver method.
- The PD inception voltages were often less than the operating voltage of the SWER lines. The tests thus show that large discharges can occur if the upper part of the insulator is covered with a conducting pollution layer.

Ultrasonic Testing

- The Pulse-Echo method was unsuccessful due to the acoustic impedance mismatching between the steel M20 bolt and glycerine that lead to negligible transmission of the incident wave into the insulators.
- The Change of Flight method was unsuccessful due to the design of the experiment, which could not secure proper transducer alignment and consistently good transducer physical contact with the insulator.

References

1. Kreuger,F.H., "Partial Discharge Detection in High Voltage Equipment", Butterworths, 1989.

Conclusions and Recommendations

This chapter reviews the study conducted on the capless porcelain line post insulator and makes final concluding remarks and recommendations. The insulator manufacture, insulator electric field simulation and the three NDT techniques for detecting internal flaws are discussed.

7.1 Conclusions

The conclusions will be grouped under appropriate headings for ease of reference. The following conclusions are made regarding the capless porcelain line post insulator.

7.1.1 Manufacture

The following conclusions are based on evidence gathered during a visit to the insulator factory.

1. The design of the embedded electrode region of the porcelain line post insulator led to the internal flaws experienced with this insulator.

2. Voids form inside the sulphur cement during the manufacturing process due to this fast setting cement and the lack of provision made in the production process to prevent air entrapment. As this is a manufacturing problem that existing quality control is unable to detect these voids could be present in all of the insulators manufactured. The X-ray evidence in chapter 6 confirms this. Sulphur cement is a dielectric and these voids can therefore lead to discharge activity.

3. Stress fractures occur in the porcelain at the top of the metal insert hole due to the geometry of the hole and the drying out of the porcelain. Sulphur cement will fill these stress fractures or air will become entrapped in them, which can lead to discharge activity. Stress fractures are a result of the insulator design and although it was expected that they would be present in most of the insulators manufactured, the X-ray evidence in chapter 6 did not confirm this. Instead, it showed that only two of the nine insulators each had a single stress

fracture that was quite deep in the direction of the applied electric field. Stress fractures can be detected by a visual inspection prior to the fitting and cementing of the metal insert.

4. De-bonding occurs in places at the sulphur cement to porcelain interface and voids are formed. De-bonding is a result of the insulator design and could be present in most of the insulators manufactured. The X-ray evidence in chapter 6 confirms this. Existing quality control during the manufacturing process is unable to detect de-bonding.

5. Voids can form in the porcelain body of the insulator. Void formation in the porcelain cannot be attributed to the insulator design and as such should not be present in most of the insulators manufactured. The X-ray evidence in chapter 6 confirms this. Porcelain is a very stable material and this insulator has a large solid porcelain body, therefore the presence of a limited void is harmless [1].

7.1.2 Electric Field Simulation

The conclusions listed under this heading are based on a computer-based electric field simulation study. The analysis of the simulation results using the SLIM 2D electrostatic software module led to the following conclusions:

- attempts to simulate the presence of a 3 mm spherical void as indicated in figure 3.4 were unsuccessful as sufficient accuracy could not be obtained due to the small size of the void.
- the value of the maximum field strength in a spherical void, should it exist in the regions of high electric field strength can be estimated, using field theory principles.
- the areas of highest electrical field stress inside the insulator were successfully identified.
- in the absence of a void the electric field strength is highest in the sulphur cement at the curved edges of the embedded electrode.
- when a void is inserted inside the sulphur cement, the electric field strength is highest inside the void. This is due to field enhancement.

- when 19kV r.m.s. (26.87kV peak) is applied to the insulator no discharge occurs inside the void.
- the electric field strength inside the void when 1MV is applied to the insulator will cause a discharge inside the void. The electric field strengths inside the 3mm void for paths AB and CD are 17.022 kV/mm and 10.788kV/mm respectively. Both of these electric field strengths are well above the 3kV/mm breakdown strength of air.
- a void near a curved edge of the embedded electrode where the electric field strength is high would create discharges of a greater magnitude than a void situated on the axis of symmetry of the insulator.
- the existence of a conductive pollution layer on the upper part of the insulator would initiate partial discharges in the voids in the sulphur cement under power frequency conditions.

7.1.3 Non-Destructive Testing

The conclusions listed under this heading are sub-divided into the three NDT techniques, namely, X-ray, Partial Discharge Detection and Ultrasonic Testing.

7.1.3.1 X-ray

1. Good defect discernibility is governed by the quality of radiation, the properties of the film, dimensions of the source, the source-to-object distance and the defect-to-film distance. In this regard the following conclusions are made:
   - a high energy X-ray source is necessary for X-raying porcelain post insulators in order to overcome the high contrast between the thin edges and thicker body sections of the insulator body. The 33kV and 22kV insulators were exposed to 150rads/min at 1metre for 2 and 1.6 minutes respectively.
   - the loss of contrast that results from using hard radiation can be partially compensated for by using Agfa-Gevaert Structurix D4 fine grain film.
   - the use of a high energy X-ray source (2MeV machine) made it possible to use a large source-to-film distance ($F = 4m$) and thereby

reduce the geometric unsharpness.

- good viewing conditions are necessary if all the information on the radiograph is to be seen.

2. The use of two X-ray images per insulator sample, 90^0 apart, adequately inspected the insulator volume for internal flaws. The internal flaws in all of nine the sample insulators were visible on the X-ray images. The following conclusions are made:
   - the shape of the top of the metal insert hole cannot be discerned on the X-ray image as there is a lack of contrast between the sulphur cement and porcelain.
   - the voids appeared to be assymmetrical in shape.
   - void location and size can be determined from the X-ray image.
   - the insulator control samples were rejected based on the X-ray evidence.
   - the most common flaw types found were voids in the sulphur cement and de-bonding between the sulphur cement and porcelain. Sulphur cement voids occurred in all nine of the sample insulators while de-bonding occurred in eight of the sample insulators.
   - porcelain stress fractures and voids in the porcelain were less common with only two of the 33kV insulators showing stress fractures and three of the 22kV insulators showing symmetrical voids in the porcelain.
   - the artistic impressions proved helpful in recapturing the detail lost in the photographing of the X-ray images.

3. X-ray is an effective NDT method of finding internal flaws in capless porcelain line post insulators, but the cost of X-raying and the burden placed on the only 2MeV high energy X-ray facility in the RSA, which is already heavily utilised make it an impractical solution.

7.1.3.2 Partial Discharge Detection

1. A workable experimental setup for PD detection of internal flaws in capless porcelain line post insulators was achieved by:
   - using the standard PD detector circuit for the E.R.A. Discharge Detector Model 3.

- immersing the inverted insulator in a glass tank with an earthed stainless steel base plate and a saturated saltwater solution as the second electrode.
- adjusting the saltwater solution level to the second shed of the inverted insulator and using Input Unit 4 to obtain a suitable sensitivity with measurable discharge magnitude.
- filling the depressions in the insulator base in the vicinity of the high voltage electrode with sunflower oil to eliminate unwanted surface discharges.

2. The prediction of the discharging void/s in an insulator is unlikely without the X-ray images and proven discharge magnitudes for void types, shapes, volumes and locations within the insulator under the same experimental conditions.

3. The number, location, shape and orientation of voids cannot be determined using this method.

4. The electrical field strength in the sulphur cement is higher than in the porcelain and this will result in the PD activity in a sulphur cement void/s masking the existence of a void/s in the porcelain dielectric. The voids in the sulphur cement are also more likely to occur and are larger than in the porcelain.

5. The ability to measure discharge activity is an indication that PD detection was successful as a NDT method for detecting the presence of internal flaws in the sample insulators.

6. A concern for future PD experimentation is that the occurrence of a single void with a large depth in the direction of the applied electric field will not be detectable using the test voltage range that this PD experiment was limited to. Nevertheless, the X-ray evidence indicates clearly that all nine of the sample insulators had multiple voids.

7. A further advantage of the liquid electrode technique (saturated saltwater solution) is that it simulates the condition where a wet conducting pollution layer exists on the upper part of the insulator. As test voltages up to 30kV were used, the real PD values measured may well occur on polluted insulators in service.

8. Only large discharge magnitudes of corona or internal discharges were audible when using the available MW radio receiver. This method is unable to distinguish between the different discharge types found in high voltage equipment. The E.R.A. Discharge Detector is well established as a PD detector and there does not appear to be any added value or need to pursue the MW radio receiver method.

7.1.3.3 Ultrasonic Testing

1. The following principles are important to the success of ultrasonic experiments:
   - acoustic impedances must be matched as best possible to ensure good transmission of the generated wave.
   - ensure that the transmitter and receiver are aligned and perpendicular to the surface of the specimen in order to avoid refraction of the incident wave.

2. 40kHz ultrasonic burglar alarm transducers were successfully modified for use in the Pulse-Echo and Change of Flight experiments and a new resonant frequency was determined.

3. No obvious coupling fluid could be found to match the acoustic impedance of the mild steel bolt in the Pulse-Echo experiment.

4. The Pulse-Echo method was unsuccessful due to the acoustic impedance mismatch between the M20 mild steel bolt and glycerine coupling gel that led to negligible transmission of the incident wave into the insulator. Theoretically 90% of the incident wave will be reflected.

5. The Change of Flight experiment was unsuccessful due to the unrepeatability of experimental results. There are two reasons for this, firstly, the non-symmetry of the insulators causing inconsistent contact area and pressure. Secondly, the ineffective clamping method used to secure the lead electrodes to the insulator, which led to transducer misalignment.

7.1.3.4 Impulse Testing

In chapter 1 the assumption was made that lightning could be the cause of the failure of the porcelain post insulator with embedded electrode. Sample B a 22kV 4kN (620mm creepage) insulator with a BIL of 150kV was impulse tested using a 1.2/50μs wave shape. The 50 percent impulse flashover voltage of the insulator was determined to be 170kV. Despite the internal flaws in this insulator it did not puncture during the impulse testing.

The upper three sheds of the insulator were then polluted using a slurry, consisting of kaolin and salt water. The purpose of this test was to induce puncturing of the insulator by transferring the impulse closer to the insulator base where the flaws exist. This measure still did not cause the insulator to puncture. The flashovers were consistently to the insulator base resulting a strong sulphur smell and some deterioration to the sulphur cement in the vicinity of the metal insert at the insulator base.

7.2 Recommendations

The recommendations will be grouped under appropriate headings for ease of reference. The following recommendations are made regarding the capless porcelain line post insulator.

7.2.1 Manufacture

1. Provision should be made in the manufacturing process to exclude voids forming in the sulphur cement particularly since quality control is unable to detect these voids. Perhaps vibrating of the assembly during the pouring of the sulphur cement could be effective in excluding voids from the cement. An

alternative cement could also be considered for fixing the metal insert into the insulator.

2. Stress fractures in the porcelain at the top of the metal insert hole can be detected by a visual inspection prior to the fitting and cementing of the metal insert. Since sulphur cement will fill these stress fractures or air will become entrapped in them, insulators with stress fractures should be rejected. Alternatively, re-engineer the insulator design and manufacturing process to eliminate stress fractures.

3. De-bonding is a result of the insulator design and this should be investigated to determine its cause.

4. If it is proved conclusively that the exclusion of internal flaws will improve the performance of the insulator and the corrective action is not effective in excluding these flaws, then an alternative insulator design should be sought.

7.2.2 Electric Field Simulation

Further electric field simulations should be undertaken using a 3D software simulation package. The effect on the electric field by asymmetrically shaped voids and voids with differing locations and orientation within the sulphur cement (including de-bonding and stress fractures) should be studied to gain further understanding of PD activity inside the insulator.

7.2.3 X-ray

X-ray should not be used as a routine NDT method, but rather as a type test to confirm future insulator designs or to confirm the success of corrective measures.

7.2.4 Partial Discharge Detection

The PD detection method described in section 5.2 is effective in determining the existence of internal flaws in capless porcelain line post insulators. A larger test voltage range will be an advantage if a single void of large depth in the direction of the applied electric field is to be detected. The inclusion of this PD experiment into

the quality control of these insulators is not suggested as it is a time consuming procedure that will lead to a bottleneck in the manufacturing procedure.

This PD test could be used to determine the effect of a conducting pollution layer on the upper part of the insulator, on PD activity under power frequency conditions.

7.2.5 Ultrasonic Testing

The ultrasonic experiments described in section 5.3 should be improved upon to ascertain the validity of this test technique by finding a suitable coupling gel and developing an improved arrangement for transducer mounting and alignment.

Ultrasonic phased-array technology that is versatile and adaptable should be considered for insulator flaw detection [2]. 3D-imaging and software processing can be produced.

7.2.6 The Effect of PD on the Insulator Materials

Porcelain is a stable material and it can be assumed that discharges of the order of 10 000pC can do no harm [1].

In chapter 2 it was shown that sulphur cement is a dielectric. The effect of PD on the life of sulphur cement is not known and this should be researched. This will assist in determining whether the voids in the cement are detrimental to the life of the insulator and help understand if they are the cause of the insulator failures experienced.

7.2.7 Impulse Testing

Further impulse testing should be carried on the capless porcelain line post insulators to investigate the assumption of failure due to lightning in chapter 1. When testing high-voltage equipment with impulse voltages the test levels are sufficiently high to expect discharges in cavities, along surfaces or corona discharges at sharp edges. However, these tests have little relation to deterioration and life expectation at nominal voltage (where discharge detection plays such an important role) [1].

References

1. Kreuger,F.H., "Partial Discharge Detection in High Voltage Equipment",

Butterworths, 1989.

2. Pérez,C., "Advanced Array Technologies for Optimised Maintenance", Amica, http://projects.tecnatom.es/amica/abstract.html

Appendix A.1

Step-Wave Output Voltage for each Attenuator Setting

db	Voltage	db	Voltage	db	Voltage	db	Voltage
0	100V	40	1.00V	80	10.0mV	120	100µV
1	89.1V	41	891mV	81	8.92mV	121	89.1µV
2	79.4V	42	794mV	82	7.94mV	122	79.4µV
3	70.8V	43	708mV	83	7.08mV	123	70.8µV
4	63.1V	44	631mV	84	6.31mV	124	63.1µV
5	56.2V	45	562mV	85	5.62mV	125	56.2µV
6	50.1V	46	501mV	86	5.01mV	126	50.1µV
7	44.7V	47	447mV	87	4.47mV	127	44.7µV
8	39.8V	48	398mV	88	3.98mV	128	39.8µV
9	35.5V	49	355mV	89	3.55mV	129	35.5µV
10	31.6V	50	316mV	90	3.16mV	130	31.6µV
11	28.2V	51	282mV	91	2.82mV	131	28.2µV
12	25.1V	52	251mV	92	2.51mV	132	25.1µV
13	22.4V	53	224mV	93	2.24mV	133	22.4µV
14	20.0V	54	200mV	94	2.00mV	134	20.0µV
15	17.8V	55	178mV	95	1.78mV	135	17.8µV
16	15.9V	56	159mV	96	1.59mV	136	15.9µV
17	14.1V	57	141mV	97	1.41mV	137	14.1µV
18	12.6V	58	126mV	98	1.26mV	138	12.6µV
19	11.2V	59	112mV	99	1.12mV	139	11.2µV
20	10.0V	60	100mV	100	1.00mV	140	10.0µV
21	8.91V	61	89.1mV	101	891µV		
22	7.94V	62	79.4mV	102	794µV		
23	7.08V	63	70.8mV	103	708µV		
24	6.31V	64	63.1mV	104	631µV		
25	5.62V	65	56.2mV	105	562µV		
26	5.01V	66	50.1mV	106	501µV		
27	4.47V	67	44.7mV	107	447µV		
28	3.98V	68	39.8mV	108	398µV		
29	3.55V	69	35.5mV	109	355µV		
30	3.16V	70	31.6mV	110	316µV		
31	2.82V	71	28.2mV	111	282µV		
32	2.51V	72	25.1mV	112	251µV		
33	2.24V	73	22.4mV	113	224µV		
34	2.00V	74	20.0mV	114	200µV		
35	1.78V	75	17.8mV	115	178µV		
36	1.59V	76	15.9mV	116	159µV		
37	1.41V	77	14.1mV	117	141µV		
38	1.26V	78	12.6mV	118	126µV		
39	1.12V	79	11.2mV	119	112µV		

Appendix A.2

Input Unit No.	Tuning Capacitance or resistance	Ultimate Sensitivity		Maximum rms current		Calibration Capacitance Cq (pF)
		Unbalanced Circuit (pC)	Balanced Circuit (pC)	Unbalanced Circuit	Balanced Circuit	
1	6pF 25pF 100pF	0.005 0.005 0.01	0.01 0.01 0.02	30mA	0.25A	2
2	25pF 100pF 400pF	0.01 0.01 0.02	0.02 0.02 0.04	60mA	0.5A	10
3	100pF 400pF 1500pF	0.02 0.02 0.04	0.04 0.04 0.08	120mA	1A	50
4	400pF 1500pF 6000pF	0.04 0.04 0.08	0.08 0.08 0.15	250mA	2A	100
5	1500pF 6000pF 0.025uF	0.08 0.08 0.15	0.15 0.15 0.3	500mA	4A	500
6	6000pF 0.025uF 0.1uF	0.15 0.15 0.3	0.3 0.3 0.6	1A	8A	1000
7	0.025uF 0.1uF 0.4uF	0.3 0.3 0.6	0.6 0.6 1.2	2A	15A	2000
8	0.1uF 0.4uF 1.5uF	0.6 0.6 1.2	1.2 1.2 2.5	4A	30A	2000
9	0.4uF 1.5uF 6uF	1.2 1.2 2.5	2.5 2.5 5	8A	60A	2000
10 10	1.5uF 6uF 25uF	2.5 2.5 5	5 5 10	15A	120A	2000
11	4uF 15uF 60uF	4 4 8	8 8 15	25A	200A	2000
12	15uF 60uF 250uF	8 8 15	15 15 30	50A	300A	2000
7R	33ohm	0.3	0.6	2A	15A	2000

Appendix A.3

Operating instructions for a complete installation are given in the system operating manual.

(a) Switch on the EARTH/GROUND toggle switch unless the equipment is earthed in some other way.

(b) Switch on the LINE/SUPPLY toggle switch and note that the SUPPLY ON lamp is now illuminated. Allow 1 minute for the instrument to warm up.

(c) Adjust the BRILLIANCE of the trace to a suitable level and adjust the FOCUS control for best focus.

(d) Increase the AMPLIFIER GAIN to maximum by turning control fully clockwise. Check that circuit noise is visible.

(e) Switch on the STEPWAVE GENERATOR and note that the STEPWAVE ON lamp is now illuminated.

(f) Connect the detector to an Input Unit using the coaxial cables with green and blue plugs.

(g) Adjust the ATTENUATION to zero and note that a very large pulse appears on the screen. Increase the ATTENUATION until this pulse is reduced to about 2cm in overall height.

(h) Connect the Voltmeter Resistor to the VOLTMETER INPUT socket and select the required VOLTMETER RANGE.

(j) Switch on the test supply and increase it until discharges are visible.

(k) Switch on the MARKERS to enable the position of the discharges to be determined.

(l) Reduce the AMPLIFIER GAIN so that the pulses displayed do not exceed 2cm in overall height. This is to prevent distortion due to overloading of the amplifier. Use the LOW GAIN INPUT socket if insufficient adjustment is available with the gain control.

(m) Adjust the ROTATE ELLIPSE switch so that the discharges occur in a suitable position for viewing.

(n) Adjust the ROTATE STEP WAVE switch so that the calibration step wave is alongside the discharge to be measured.

(o) Adjust the ATTENUATION until the calibration step wave is the same size as the discharge. Read off the attenuation and compute the discharge magnitude, as described in the System Manual.

(p) If required the discharge and calibration step wave may be compared along a straight line by operating the ELLIPSE HEIGHT switch to the COLLAPSED position.

Appendix B.1

Characteristics of Some Nonpiezoelectric Materials[a]

Material	Mass Density, kg/m³	Longitudinal Velocity, m/s	Acoustic Impedance, $\times 10^6$ kg/m² · s
Air (20°C)	1.21	340	411×10^{-6}
Water (20°C)	1,000	1,480	1.5
Glycerine	1,260	1,920	2.5
Castor oil	950	1,540	1.46
Motor car oil (SAE 20)	870	1,740	1.5
Polyalkyleneglycol (PAG), 20°C	973	1,330	1.29
Choloroform	1,480	1,010	1.5
Carbon tetrachloride, 20°C	1,590	940	1.5
Paraffin	860	1,420	1.22
Ice	900	3,980	3.6
Lithium	5,330	3,000	16
Teflon	2,160	1,340	3
Acrylic resin (Lucite, Perspex, Plexiglass)	1,182	2,680	3.17
Polyethylene	900	1,940	1.75
Polystyrene	1,056	2,340	2.47
Epoxy resin	1,100–1,250	2,400–2,900	2.7–3.6
Nylon, Perlon	1,100–1,200	2,200–2,600	2.4–3.1
Silicon rubber (GE, RTV 615)	1,010	1,030	1.04
Aluminum	2,695	6,350	17.1
Indium	7,310	2,500	18.3
Beryllium	1,850	12,500	23.1
Brass	8,100	4,430	35.9
Lead	11,400	1,960	22.3
Copper	8,900	4,700	42
Gold	19,300	3,210	62
Iron (steel)	7,830	5,950	46.6
Mercury	13,600	1,450	20
Mylar	1,180	2,540	3
Platinum	21,400	4,152	89
Silver	10,490	3,440	36.1
Tungsten	19,100	5,500	105.1
Zinc	7,100	4,200	30
Titanium	4,500	6.071	27.3
Nickel	8,905	6,030	53.7
Glass T-40	3,390	4,310	14.6
Sapphire (z axis)	3,990	11,100	44.3
Glass, Pyrex	2,320	5,610	13
Glass, crown	2,243	5,090	11.4
Glass, flint	3,879	4,030	15.6
Fused quartz (silica)	2,200	5,970	13.1
Rutile (z axis)	4,260	7,900	33.7
Methanol, 30°C	796	1,088	0.866
Acetone, 30°C	791	1,158	0.916
Ethanol, 30°C	789	1,127	0.890
Zircaloy (Zr–2.5Nb)	6,500	4,686	30.5
Magnesium	1,720	5,800	10
Graphite	2,170	4,210	9.14
Magnesia (MgO)	3,842	8,850	34
Silicon, along [100]	2,337	8,430	19.7
Flutec PP3 (C_7F_{14} + C_8F_{16})	1,900	612	1.12
Stainless steel	8,090	5,610	45.4
Porcelain	2,400	5,600	13.4

[a]The parameters listed for some materials should be considered as an average. The parameters of these vary depending on the production method used. Ice and metals are assumed to be polycrystalline.

Appendix C.1

Experimental results from PD detection monitoring of insulator sample 2.

Test voltage (kV)	13	14	15	16	17	18	19	20	21	22	23	24	25
Attenuation value (dB)	90	89	60	60	60	59	55	55	55	55	55	55	55
Step-wave output voltage (mV)	3.16	3.55	100	100	100	112	178	178	178	178	178	178	178
Discharge magnitude (pC)	0.32	0.36	10.20	10.20	10.20	11.42	18.16	18.16	18.16	18.16	18.16	18.16	18.16

Test voltage (kV)	26	27	28	29	30	29	28	27	26	25	24	23	22	21
Attenuation value (dB)	58	60	60	60	60	60	62	61	61	61	62	63	64	67
Step-wave output voltage (mV)	126	100	100	100	100	100	79.4	89.1	89.1	89.1	79.4	70.8	63.1	44.7
Discharge magnitude (pC)	12.85	10.20	10.20	10.20	10.20	10.20	8.10	9.09	9.09	9.09	8.10	7.22	6.44	4.56

Test voltage (kV)	20	19	18	17	16	15	14	13	12
Attenuation value (dB)	65	67	70	72	78	80	84	87	Extinction
Step-wave output voltage (mV)	56.2	44.7	31.6	25.1	12.6	10	6.31	4.47	Extinction
Discharge magnitude (pC)	5.73	4.56	3.22	2.56	1.29	1.02	0.64	0.46	Extinction

Appendix C.2

Experimental results from PD detection monitoring of insulator sample 3.

Test voltage (kV)	11	12	13	14	15	16	17	18	19	20	21	22	23	24
Attenuation value (dB)	88	100	96	96	93	93	75	80	90	88	90	84	80	58
Step-wave output voltage (mV)	3.98	1	1.59	1.59	2.24	2.24	17.8	10	3.16	3.98	3.16	6.31	10	126
Discharge magnitude (pC)	0.41	1.10	0.16	0.16	0.23	0.23	1.81	1.02	0.32	0.41	0.32	0.64	1.02	12.84

Test voltage (kV)	25	26	27	28	29	30	29	28	27	26	25	24
Attenuation value (dB)	55	55	40	40	43	44	44	44	44	44	43	55
Step-wave output voltage (mV)	178	178	1000	1000	708	631	631	631	631	631	708	178
Discharge magnitude (pC)	18.14	18.14	101.90	101.90	72.15	64.30	64.30	64.30	64.30	64.30	72.15	18.14

Test voltage (kV)	23	22	21	20	19	18	17	16	15	14	13	12	11	10
Attenuation value (dB)	57	58	58	58	60	63	63	80	80	80	95	95	95	95
Step-wave output voltage (mV)	141	126	126	126	100	79.4	79.4	10	10	10	1.78	1.78	1.78	1.78
Discharge magnitude (pC)	14.37	12.84	12.84	12.84	10.19	8.09	8.09	1.02	1.02	1.02	0.18	0.18	0.18	0.18

Test voltage (kV)	9	8	7	6	5
Attenuation value (dB)	95	96	98	100	Extinction
Step-wave output voltage (mV)	1.78	1.59	1.26	1	Extinction
Discharge magnitude (pC)	0.18	0.16	0.13	0.10	Extinction

Appendix C.3

Experimental results from PD detection monitoring of insulator sample 4.

Test voltage (kV)	13	14	15	16	17	18	19	20	21	22	23	24
Attenuation value (dB)	95	90	88	43	35	35	37	27	27	27	26	27
Step-wave output voltage (mV)	1.78	3.16	3.98	708	1780	1780	1410	4470	4470	4470	5010	4470
Discharge magnitude (pC)	0.18	0.32	0.40	71.86	180.67	180.67	143.12	453.71	453.71	453.71	508.52	453.71

Test voltage (kV)	25	26	27	28	29	30	29	28	27	26	25	24
Attenuation value (dB)	27	27	25	30	27	30	28	43	45	46	48	75
Step-wave output voltage (mV)	4470	4470	5620	3160	4470	3160	3980	708	562	501	398	17.8
Discharge magnitude (pC)	453.71	453.71	570.43	320.74	453.71	320.74	403.97	71.86	57.04	50.85	40.40	1.81

Test voltage (kV)	23	22	21	20	19	18	17	16	15	14	13	12
Attenuation value (dB)	76	78	80	86	86	87	87	89	92	92	95	Extinction
Step-wave output voltage (mV)	15.9	12.6	10	5.01	5.10	4.47	4.47	3.55	2.51	2.51	1.78	Extinction
Discharge magnitude (pC)	1.61	1.28	1.02	0.51	0.51	0.45	0.45	0.36	0.25	0.25	0.18	Extinction

Appendix C.4

Experimental results from PD detection monitoring of insulator sample CX2.

Test voltage (kV)	4	5	6	7	8	9	10	11	12	13	14	15	16	17
Attenuation value (dB)	95	90	90	89	80	80	83	68	66	71	77	82	78	78
Step-wave output voltage (mV)	1.78	3.16	3.16	3.44	10	10	7.08	39.8	50.1	28.2	14.1	7.94	12.6	12.6
Discharge magnitude (pC)	0.18	0.32	0.32	0.35	1.02	1.02	0.72	4.04	5.09	2.86	1.43	0.81	1.28	1.28

Test voltage (kV)	18	19	20	21	22	23	24	25	26	27	28	29	30	29
Attenuation value (dB)	84	67	73	75	62	64	64	65	65	65	65	65	51	40
Step-wave output voltage (mV)	6.31	44.7	22.4	17.8	79.4	63.1	63.1	56.2	56.2	56.2	56.2	56.2	2.82	1000
Discharge magnitude (pC)	0.64	4.54	2.27	1.81	8.06	6.40	6.40	5.70	5.70	5.70	5.70	5.70	28.62	101.50

Test voltage (kV)	28	27	26	25	24	23	22	21	20	19	18	17	16
Attenuation value (dB)	50	78	79	77	84	89	82	85	89	90	93	98	Extinction
Step-wave output voltage (mV)	316	12.6	11.2	14.1	6.31	3.55	7.94	5.62	3.55	3.16	2.24	1.26	Extinction
Discharge magnitude (pC)	32.07	1.28	1.14	1.43	0.64	0.36	0.81	0.57	0.36	0.32	0.23	0.13	Extinction

Appendix C.5

Experimental results from PD detection monitoring of insulator sample CX1.

Test voltage (kV)	10	11	12	13	14	15	16	17	18	19	20	21	22	23
Attenuation value (dB)	80	85	90	94	80	80	80	74	74	74	45	50	50	52
Step-wave output voltage (mV)	10	5.62	3.16	2	10	10	10	20	20	20	562	316	316	251
Discharge magnitude (pC)	1.02	0.57	0.32	0.20	1.02	1.02	1.02	2.03	2.03	2.03	57.04	32.07	32.07	25.48

Test voltage (kV)	24	25	26	27	28	29	30	29	28	27	26	25	24	23
Attenuation value (dB)	57	62	60	60	70	69	67	67	75	77	78	78	78	79
Step-wave output voltage (mV)	141	79.4	100	100	31.6	35.5	44.7	44.7	17.8	14.1	12.6	12.6	12.6	11.2
Discharge magnitude (pC)	14.31	8.06	10.15	10.15	3.21	3.59	4.54	4.54	1.81	1.43	1.28	1.28	1.28	1.14

Test voltage (kV)	22	21	20	19	18	17	16	15	14	13	12	11	10	9
Attenuation value (dB)	82	84	80	79	78	78	78	80	80	79	81	81	81	Extinction
Step-wave output voltage (mV)	7.94	6.31	10	11.2	12.6	12.6	11.2	10	10	11.2	8.92	8.92	8.92	Extinction
Discharge magnitude (pC)	0.81	0.64	1.02	1.14	1.28	1.28	1.14	1.02	1.02	1.14	0.91	0.91	0.91	Extinction

Appendix C.6

Experimental results from PD detection monitoring of insulator sample A.

Test voltage (kV)	22	23	24	25	26	27	28	29	30	29	28	27	26
Attenuation value (dB)	59	65	72	69	67	62	70	20	20	32	39	34	74
Step-wave output voltage (mV)	112	56.2	25.1	35.5	44.7	79.4	31.6	10000	10000	2510	1120	2000	20
Discharge magnitude (pC)	11.37	5.70	2.55	3.60	4.54	8.06	3.21	1015.00	1015.00	254.77	113.68	203.00	2.03

Test voltage (kV)	25	24	23	22	21	20
Attenuation value (dB)	74	82	84	84	85	Extinction
Step-wave output voltage (mV)	20	7.94	6.31	6.31	5.62	Extinction
Discharge magnitude (pC)	2.03	0.81	0.64	0.64	0.57	Extinction

Appendix C.7

Experimental results from PD detection monitoring of insulator sample B.

Test voltage (kV)	16	17	18	19	20	21	22	23	24	25	26	27	28
Attenuation value (dB)	88	87	87	87	87	85	70	57	65	55	70	5	6
Step-wave output voltage (mV)	3.98	4.47	4.47	4.47	4.47	5.62	31.6	141	56.2	178	31.6	56200	50100
Discharge magnitude (pC)	0.40	0.45	0.45	0.45	0.45	0.57	3.21	14.31	5.70	18.07	3.21	5704.30	5085.15

Test voltage (kV)	29	30	29	28	27	26	25	24	23	22
Attenuation value (dB)	5	1	1	1	1	1	7	8	8	8
Step-wave output voltage (mV)	56200	89100	89100	89100	89100	89100	44700	39800	39800	39800
Discharge magnitude (pC)	5704.30	9043.65	9043.65	9043.65	9043.65	9043.65	4537.05	4039.70	4039.70	4039.70

Test voltage (kV)	21	20	19	18	17	16	15	14	13	12
Attenuation value (dB)	8	10	75	77	82	87	85	78	78	72
Step-wave output voltage (mV)	39800	31600	17.8	14.1	7.94	4.47	5.62	12.6	12.6	25.1
Discharge magnitude (pC)	4039.70	3207.40	1.81	1.43	0.81	0.45	0.57	1.28	1.28	2.55

Test voltage (kV)	11	10
Attenuation value (dB)	80	Extinction
Step-wave output voltage (mV)	10	Extinction
Discharge magnitude (pC)	1.02	Extinction

Appendix C.8

Experimental results from PD detection monitoring of insulator sample C.

Test voltage (kV)	22	23	24	25	26	27	28	29	30	29	28	27
Attenuation value (dB)	87	62	62	62	62	62	64	62	58	61	68	71
Step-wave output voltage (mV)	4.47	79.4	79.4	79.4	79.4	79.4	63.1	79.4	126	89.1	39.8	28.2
Discharge magnitude (pC)	0.45	8.06	8.06	8.06	8.06	8.06	6.41	8.06	12.79	9.04	4.04	2.86

Test voltage (kV)	26	25	24	23	22	21	20	19	18	17	16	15
Attenuation value (dB)	72	75	80	82	84	86	88	88	88	92	92	Extinction
Step-wave output voltage (mV)	25.1	17.8	10	7.94	6.31	5.01	3.98	3.98	3.98	2.51	2.51	Extinction
Discharge magnitude (pC)	2.55	1.81	1.02	0.81	0.64	0.51	0.40	0.40	0.40	0.26	0.26	Extinction

Appendix C.9

Experimental results from PD detection monitoring of insulator sample CX.

Test voltage (kV)	21	22	23	24	25	26	27	28	29	30	29
Attenuation value (dB)	57	57	55	55	55	56	55	55	55	56	57
Step-wave output voltage (mV)	141	141	178	178	178	159	178	178	178	178	178
Discharge magnitude (pC)	14.31	14.31	18.07	18.07	18.07	16.14	18.07	18.07	18.07	18.07	18.07

Test voltage (kV)	28	27	26	25	24	23	22	21	20	19
Attenuation value (dB)	57	57	57	57	58	58	59	57	67	Extinction
Step-wave output voltage (mV)	159	141	141	141	126	126	112	141	44.7	Extinction
Discharge magnitude (pC)	16.14	14.31	14.31	14.31	12.79	12.79	11.37	14.31	4.54	Extinction